Pluto's Sputnik Planitia: Composition of geological units from infrared spectroscopy

F. Scipioni, O. White, J.C. C Cook, T. Bertrand, D.P. P Cruikshank, W.M. M Grundy, C. Beddingfield-Cartwright, R.P. P Binzel, C.M. M Dalle Ore, D. Jennings, et al.

PLUTO'S SPUTNIK PLANITIA: COMPOSITION OF GEOLOGICAL UNITS FROM INFRARED SPECTROSCOPY

F. Scipioni[1], O. White[1,2], J.C. Cook[3], T. Bertrand[2], D.P. Cruikshank[2], W.M. Grundy[4], C. Beddingfield-Cartwright[1], R. P. Binzel[5], C.M. Dalle Ore[1,2], D. Jennings[6], J.M. Moore[2], C.B. Olkin[7], S. Protopapa[7], D. C. Reuter[6], B. Schmitt[8], K.N. Singer[7], J.R. Spencer[7], S.A. Stern[7], H.A. Weaver[9], A.J. Verbiscer[10], L.A. Young[7].

[1]SETI Institute, Mountain View, CA, 94040, USA
[2]NASA Ames Research Center; Moffett Field, CA, 94035, USA
[3]Pinhead Institute, Telluride, CO, USA
[4]Lowell Observatory, Flagstaff, AZ, 8600, USA
[5]Massachusetts Institute of Technology, Cambridge, MA 02139, USA
[6]NASA Goddard Space Flight Center, Greenbelt, MD 20771, USA
[7]Southwest Research Institute, Boulder, CO, 80302, USA
[8]Université Grenoble Alpes, CNRS, Grenoble, France
[9]Johns Hopkins University Applied Physics Laboratory, Laurel, MD, 20723, USA
[10]University of Virginia, Charlottesville, VA, 22904, USA

* Some feature names mentioned in this paper are now formalized while others are informal

Abstract

We have compared spectroscopic data of Sputnik Planitia on Pluto, as acquired by New Horizons' Linear Etalon Imaging Spectral Array (LEISA) instrument, to the geomorphology as mapped by White et al. (2017) using visible and panchromatic imaging acquired by the LOng-Range Reconnaissance Imager (LORRI) and the Multi-spectral Visible Imaging Camera (MVIC). We have focused on 13 of the geologic units identified by White et al. (2017), which include the plains and mountain units contained within the Sputnik basin. We divided the map of Sputnik Planitia into 15 provinces, each containing one or more geologic units, and we use LEISA to calculate the average spectra of the units inside the 15 provinces. Hapke-based modeling was then applied to the average spectra of the units to infer their surface composition, and to determine if the composition resulting from the modeling of LEISA spectra reflects the geomorphologic analyses of LORRI data, and if areas classified as being the same geologically, but which are geographically separated, share a similar composition. We investigated the spatial distribution of the most abundant ices on Pluto's surface - CH_4, N_2, CO, H_2O, and a non-ice component presumed to be a macromolecular carbon-rich material, termed a tholin, that imparts a positive spectral slope in the visible spectral region and a negative spectral slope longward of ~1.1 μm. Because the exact nature of the non-ice component is still debated and because the negative spectral slope of the available tholins in the near infrared does not perfectly match the Pluto data, for spectral modeling purposes we reference it generically as the negative spectral slope endmember (NSS endmember). We created maps of variations in the integrated band depth (from LEISA data) and areal mass fraction (from the modeling) of the components. The analysis of correlations between the occurrences of the endmembers in the geologic units led to the observation of an anomalous suppression of the strong CH_4 absorption bands in units with compositions that are dominated by H_2O ice and the NSS endmember. Exploring the mutual variation of the CH_4 and N_2 integrated band depths with the abundance of crystalline H_2O and NSS

* Some feature names mentioned in this paper are now formalized while others are informal

endmember revealed that the NSS endmember is primarily responsible for the suppression of CH_4 absorptions in mountainous units located along the western edge of Sputnik Planitia. Our spectroscopic analyses have provided additional insight into the geological processes that have shaped Sputnik Planitia. A general increase in volatile abundance from the north to the south of Sputnik Planitia is observed. Such an increase first observed and interpreted by Protopapa et al. 2017 and later confirmed by climate modeling (Bertrand et al., 2018) is expressed geomorphologically in the form of preferential deposition of N_2 ice in the upland and mountainous regions bordering the plains of southern Sputnik Planitia. Relatively high amounts of pure CH_4 are seen at the southern Tenzing Montes, which are a natural site for CH_4 deposition owing to their great elevation and the lower insolation they are presently receiving. The NSS endmember correlates the existence of tholins within certain units, mostly those coating the low-latitude mountain ranges that are co-latitudinal with the tholin-covered Cthulhu Macula. The spectral analysis has also revealed compositional differences between the handful of occurrences of northern non-cellular plains and the surrounding cellular plains, all of which are located within the portion of Sputnik Planitia that is presently experiencing net sublimation of volatiles, and which do not therefore exhibit a surface layer of bright, freshly-deposited N_2 ice. The compositional differences between the cellular and non-cellular plains here hint at the effectiveness of convection in entraining and trapping tholins within the body of the cellular plains, while preventing the spread of such tholins to abutting non-cellular plains.

1. Introduction

In 2015 the New Horizons spacecraft encountered dwarf planet Pluto, unveiling a complex and diverse icy world (Stern et al., 2015). Prior to New Horizons' flyby, Pluto had been extensively studied from ground-based and space telescopes. Observations in the visible (VIS; e.g., Lorenzi et al., 2016) and infrared range (IR; e.g. Cruikshank et al., 1976; Grundy et al., 2013; 2014; Merlin, 2015, Olkin et al., 2007; Protopapa et al., 2008), determined that Pluto's

* Some feature names mentioned in this paper are now formalized while others are informal

uppermost surface layer is mostly composed of frozen N_2, CH_4, CO, C_2H_6, along with additional non-ice, organic components (Cruikshank et al., 2015). This surficial coating overlies bedrock made of H_2O ice.

The surface of Pluto exhibits distinct terrain types, the most conspicuous being Sputnik Planitia*, a 1000 km by 1300 km wide impact basin that is interpreted to have formed $\gtrsim$4 Gya (Moore et al., 2016; McKinnon et al., 2016; Johnson et al., 2016; Keane et al., 2016; Nimmo et al., 2016; Schenk et al., 2018). The deep basin represents a powerful cold trap and a natural setting for the accumulation of volatile ices spread across Pluto's surface, principally N_2 and CO ice (Bertrand & Forget, 2016; Hamilton et al., 2016; Earle et al., 2017). Modeling of volatile behavior in response to topography has shown that infilling of the basin with the majority of surface N_2-CO ice would be complete by tens of millions of years after its formation (Bertrand et al., 2018). Most of the surface of Sputnik Planitia today is depressed by 2.5-3.5 km relative to the basin rim, and by 2 km relative to Pluto's mean radius (Schenk et al., 2018). No impact craters are seen within Sputnik Planitia in contiguous 315 m/pixel mapping coverage (Robbins et al., 2017; White et al., 2017; Singer et al., 2019), indicating very recent resurfacing of its plains. The central and northern portions of Sputnik Planitia are marked by a reticulate pattern of troughs a few km wide that divide the plains into ovoid cells (Stern et al., 2015; Moore et al., 2016). The cells likely originated due to solid-state convection of the N_2-CO ice, with a surface renewal timescale of <1 Myr (McKinnon et al., 2016; Trowbridge et al., 2016; Buhler & Ingersoll, 2018). Cells are absent within the southern and eastern parts of Sputnik Planitia, which instead display featureless plains or dense concentrations of sublimation pits reaching a few km across (Stern et al., 2015; Moore et al., 2016; White et al., 2017). A discontinuous chain of mountain ranges, consisting of discrete angular blocks with apparently random orientations, extends for hundreds

* Some feature names mentioned in this paper are now formalized while others are informal

of kilometers along the western margin of Sputnik Planitia (Moore et al., 2016; Skjetne et al., 2020). These are interpreted to be fragments of Pluto's tectonized and brecciated H_2O ice crust that were intruded by glacial N_2-CO ice covering the uplands and flowing into the Sputnik basin in the aftermath of the impact, and subsequently dislodged, transported and rotated by the glacial ice to form the ranges (Moore et al., 2016; Stern et al., 2015; Howard et al., 2017; O'Hara & Dombard, 2020).

We report here a compelling analysis of the Sputnik Planitia region, performed by comparing the data acquired by the LOng-Range Reconnaissance Imager (LORRI) (Cheng et al., 2008) with the spectroscopic observations returned by the Linear Etalon Imaging Spectral Array (LEISA) (Reuter et al., 2009). Our investigation has the goal to understand if the terrain units identified by White et al. (2017) on the basis of geologic analysis, display distinct spectral characteristics in addition to their geomorphology and albedo.

2. Geologic and spectral mapping

A geological map of Sputnik Planitia was produced by White et al. (2017), using a mosaic of 12 LORRI images as the base map. The base map covers the plains themselves and the surrounding uplands. The mapping defined 15 geologic units, based primarily on the surface texture and albedo that they present at the 386 m/pixel scale of the base map; topographic relief as expressed in the global stereo digital elevation model (Schenk et al., 2018) was generally not useful for unit definition due to the extreme flatness of the plains. In this work we focus on 13 of the 15 units presented in White et al. (2017), excluding the Impact Crater (ic) and Bright, Pitted Uplands (bpu) units because they are exterior to Sputnik Planitia. Figure 1 - which corresponds to Figure 5 in White et al. (2017) - shows the Sputnik Planitia geological map, and Table 1

* Some feature names mentioned in this paper are now formalized while others are informal

describes the diagnostic characteristics and interpretations of these units as presented in White et al. (2017).

Cellular plains occupy the core of Sputnik Planitia, with cell boundaries consisting of trough and ridge morphology. The cellular plains are brighter in the central-south area (bcp), and darker in the central-northern part (dcp). The northern margin of Sputnik Planitia shows very low-albedo plains (tbp), but within which cell boundaries can still be discerned. The western rim of Sputnik Planitia is occupied by chains of randomly oriented blocky mountains (abm) - embayed by inter-block material (ibm) - and by dark-pitted, marginal plains (dmp), and dark, ridged terrain (drt). A few isolated mountain blocks of unit abm are seen within the plains of unit dcp, separated from the main ranges. The spatially largest abm area inside the cellular plains of Sputnik Planitia is Coleda de Dados Colles. To the east and south, Sputnik Planitia shows four types of pitted plains. The lightly pitted plains (lpp) bound the cellular plains along their eastern margin, the sparsely (spp) and deeply pitted plains (dpp) dominate the southernmost region of Sputnik Planitia, and the patchy, pitted, marginal plains (pmp) separate the interior plains from the surrounding highlands along the eastern and southwestern boundaries of Sputnik Planitia. These pitted plains units are concentrated within the eastern and southern regions of Sputnik Planitia, but small expanses of the units are identified on the northern and western edges as well, where they are embayed by the cellular plains and mountain units. Conglomerations of blocks reaching a few km across are seen within the cellular and pitted plains in the eastern portion of Sputnik Planitia, forming the scattered hills unit (sh).

The 13 units that form Sputnik Planitia and its mountain ranges do not commonly concentrate in a single, spatially coherent region, and often occur in several localities across the mapping area that are isolated from each other. To gauge geographical variation in the spectral properties

* Some feature names mentioned in this paper are now formalized while others are informal

of these units, we have divided the Sputnik Planitia map into 15 provinces* (Figure 2). These provinces typically display contiguous geomorphological characteristics across their expanse, specifically cellular plains for the “Cellular plains” province, non-cellular plains for the “south pitted plains” and "east pitted plains", “southwest buffer”, “west pitted plains” and “north pitted plains” provinces, and mountainous and hilly terrain for the ten “Montes” and “Colles” provinces. This strategy allows us to define the bulk spectral characteristics of each of the 13 units across the entire mapping area, and also the spectral characteristics for isolated occurrences of each unit within these separate provinces. This in turn will allow us to assess the degree to which spatially distant occurrences of a particular unit are spectrally similar, and if their spectra do vary with location, then what factors contribute to such variation.

The scientific payload onboard NH designed to investigate the spectral characteristics of Pluto’s surface is Ralph, a multispectral imager composed by two different instrument sub-systems covering the visible (VIS) and near infrared (NIR) regions of the spectrum with two independent spectrometers. The first component is MVIC, the Multi-spectral Visible Imaging Camera, with its three VIS and NIR channels, blue (400–550 nm), red (540–700 nm), and NIR (780–975 nm), and a narrow CH_4 band filter (860–910 nm). The second instrument sub-system is the Linear Etalon Imaging Spectral Array (LEISA). LEISA has two filter segments, the first covering the 1.25–2.5 μm short wave infrared (SWIR) spectral region (spectral power $\lambda/\Delta\lambda$ = 240) to produce spectral maps, the second covering the 2.1-2.25 μm range ($\lambda/\Delta\lambda$ = 560) to investigate the solid-N_2 absorption feature centered at 2.15 μm. LEISA scans the 0.9°x0.9° FOV in a push broom fashion (Reuter et al., 2009). In this work we used the data from the LEISA SWIR segment only.

* Some feature names mentioned in this paper are now formalized while others are informal

We considered three high spatial resolution (ranging between ~ 6 and ~ 9 km/pixel) LEISA spectral image cubes to produce a mosaic of Sputnik Planitia with the Integrated Software for Imagers and Spectrometers (ISIS) routines. The image cubes were first projected on a common simple cylindrical map, centered at 180°E and 0°N, with a pixel resolution to 2 km/px (smaller than the original resolution of the three LEISA scans). We then converted the I/F radiance (as defined in Hapke, 2012) into a reflectance factor (*REFF*) to minimize the effect of solar incidence on the reflected radiance and maximize the absorbing and scattering properties of the surface materials (Schmitt et al., 2017). The *REFF* is calculated, for each pixel, by dividing the I/F radiance by the cosine of the incidence angle (Hapke, 2012), assuming isotropic scattering of the surface (Lambertian photometry). The I/F values have been corrected by the scaling factor in the LEISA radiometric calibration of 0.74±0.05 reported by Protopapa et al. 2020. The three projected cubes were then averaged together to create the final spectral mosaic. LORRI basemap used by White et al. (2017) for the geologic classification, was projected and sampled at the same scale of the LEISA mosaic, so to precisely compare them. We selected regions of interest on the LEISA mosaic corresponding to the Sputnik Planitia geologic units identified in White et al. (2017) by using the ENVI image analysis software.

Figure 1: *Geologic units identified in Sputnik Planitia by White et al. (2017) through analysis of New Horizons LORRI images. The original 15 units initially identified were reduced to 13 here, to include only the geologic units within and around Sputnik Planitia. The basemap mosaic is a combination of 12 LORRI images, with a spatial resolution of 386 m/px.*

Table 1. Descriptions and interpretations of 13 geologic units within Sputnik Planitia mapped by White et al. (2017).

Unit	Description	Interpretation
Bright, Cellular plains (bcp)	High albedo plains divided into ovoid cells by a network of troughs. Cell interiors typically display a pitted	Plains of N_2-CO ice undergoing continuous resurfacing by solid-state convection. High albedo is caused by

* Some feature names mentioned in this paper are now formalized while others are informal

	texture at a scale of a few hundred meters towards their edges. Concentrates in central Sputnik Planitia.	condensation of atmospheric N_2-CO onto the Dark, Cellular plains to form a thin mantle of pure N_2-CO ice.
Dark, Cellular plains (dcp)	Similar to the Bright, Cellular plains, but with a lower albedo. Concentrates in northern and western Sputnik Planitia, but also appears as enclaves within the Bright, Cellular plains near the main contact between the two units.	Unit is deficient in N_2-CO relative to the Bright, Cellular plains and represents the exposed portion of the convecting N_2-CO ice mass, which displays a high content of entrained tholin accumulated.
Dark, Trough-Bounding Plains (tbp)	Low albedo plains at the northern edge of Sputnik Planitia that surround cell margins, which appear as narrow, dark lines. Exhibit flow patterns around obstacles at the margin with the surrounding uplands.	N_2-CO ice with an especially high concentration of entrained tholins at the edges of the cells and in the bounding troughs. Flow patterns indicate recent mobility of the N_2-CO ice.
Lightly Pitted Plains (lpp)	High albedo plains displaying a shallow, densely pitted texture at a scale of a few hundred meters.	Sublimation of N_2-CO ice across the surface of the plains.
Deeply Pitted Plains (dpp)	High albedo plains featuring dense concentrations of dark-floored pits reaching a few km across. Pits can be single or merge to form doublets and chains of elongate, aligned pits. Pit swarms sometimes form wavelike patterns.	Sublimation pits that may be widening existing fractures formed by ice shearing in the N_2-CO ice plains. Floors are covered by dark tholins. Wavelike patterns may reveal stress fields associated with flow paths.
Sparsely Pitted Plains (spp)	Smooth, high albedo plains featuring scattered pits with subdued and softened relief.	Plains that have been resurfaced by flow of N_2-CO ice, and/or blanketing by atmospheric N_2-CO condensation, which acts to relax/infill pit topography.
Patchy, Pitted, Marginal Plains (pmp)	High albedo, often-hummocky plains on the margins of Sputnik Planitia. Generally, it displays a patchy texture of close-spaced shallow pits interspersed with smooth, featureless zones. Dark flow lines are often seen where the unit occurs along the border with the Bright, Pitted Uplands.	Shallow N_2-CO ice draped over underlying topography, which may contribute to the heterogeneous texture of the unit. Glacial flow of the unit is occurring from valleys in the Bright, Pitted Uplands to the open plains of Sputnik Planitia.
Dark-Pitted, Marginal Plains (dmp)	High albedo plains displaying chains of elongate, dark-floored pits interspersed with smooth, lightly pitted zones. Unit occurs on the western edge of Sputnik Planitia.	Shallow N_2-CO ice draped over underlying topography. The ice may be residual and relatively immobile compared to that of the Patchy, Pitted, Marginal Plains. Dark pit floors represent Cthulhu Macula, which this unit overlies.
Chaotic, Angular, Blocky Mountains (abm)	Discontinuous chain of mountain ranges, consisting of angular blocks with random orientations. Ranges	Fragments of the H_2O ice crust that have been detached by tectonism and intruded, transported, and rotated by glacial N_2-CO

* Some feature names mentioned in this paper are now formalized while others are informal

	extend along the western margin of Sputnik Planitia, with a few isolated blocks occurring within its interior.	ice. The mountain blocks are now grounded within shallow N_2-CO ice of Sputnik Planitia.
Chaotic, Inter-Block Material (ibm)	Chaotically oriented, close-packed blocks, reaching several km across, that are interstitial to and embay the Chaotic, Angular, Blocky Mountains.	Like the Chaotic, Angular, Blocky Mountains, but finer texture may indicate breaking up of mountain blocks into smaller fragments and/or size filtering thereafter.
Scattered Hills (sh)	Hills scattered across east Sputnik Planitia that reach a few km across and tend to collect into densely packed clusters. Chains of aligned hills occur proximal to the Bright, Pitted Uplands. In the Bright, Cellular plains, the hills are always coincident with the cell boundaries.	CH_4 ice fragments eroded from the Bright, Pitted Uplands that have rafted into Sputnik Planitia on valley glaciers of denser N_2-CO ice. In the Bright, Cellular plains, convective motions corral them into clusters at cell boundaries.
Dark, Ridged Terrain (drt)	Situated between the Chaotic, Angular, Blocky Mountains of western Sputnik Planitia and uplands to the west. Aligned ridges are oriented parallel to the edge of Sputnik Planitia, and display wavelengths from several hundred meters to a few km.	Possibly Chaotic, Inter-Block Material covered by dark mantling material. Compression of this unit by pressure exerted from westward motion of the Chaotic, Angular, Blocky Mountains may produce the ridges.
Bright, Chaotic Terrain (bct)	High albedo plains interspersed with darker blocks reaching several km across, on the northwest margin of Sputnik Planitia. E-W oriented troughs and scarps cross the unit. Parts of the unit are depressed by several hundred meters below the bordering Chaotic Inter-Block Material.	Unit represents uplands material that is experiencing extensional tectonism and subsidence, and possible intrusion by N_2-CO ice of Sputnik Planitia. High albedo of the plains indicates a surface covering of N_2-CO ice, possibly 'overflowed' from Sputnik Planitia. Unit may represent an incipient stage of formation of the Chaotic, Angular, Blocky Mountains.

Figure 2: The 15 provinces that we have divided the Sputnik Planitia geologic map into, with each province containing one or more geologic unit. Indeed, some geologic unit covers areas that are spatially distant and surrounded by very divers terrain types. For example, spp unit can be found in 5 different provinces: in the northernmost part of Sputnik Planitia (North Pitted Plains), embedded in the cellular plains; in the West Pitted Plains, again close to the cellular plains, but also to the blocky mountains; in the Hillary Montes region, surrounded by inter-blocky material; in the Southwest Buffer and the South-East Pitted Plains, where the other types of pitted plains dominate.

3. Methodology

The LEISA mosaic allows us to calculate the average spectrum of each geologic unit inside each province, giving a total of 48 spectra. The average spectra of the 13 geologic units are shown in Figure 3. In the spectral region covered by LEISA's low-spectral-resolution segment

* Some feature names mentioned in this paper are now formalized while others are informal

(1.25-2.5 μm), the spectrum of Sputnik Planitia is dominated, on average, by CH_4, N_2, and CO ice absorptions (e.g. Grundy et al., 2016). Some regions also show the presence of H_2O ice. CH_4 has four series of broad absorptions in the region between 1.30–1.43 μm (Range 1), 1.59–1.83 μm (Range 2), 1.90–2.00 μm (Range 3), and 2.09–2.48 μm (Range 4), and a single band centered at 1.48 μm (Schmitt et al., 2017). CO and N_2 absorption bands are centered at 1.58 μm and 2.15 μm, respectively.

Figure 3: Average spectra of the 13 geologic units identified by White et al. (2017). The boxes indicate the location of the main absorption bands of CH_4, CO and N_2.

3.1 Absorption bands analysis

We calculated the integrated band depth of the main CH_4, N_2, CO, and H_2O ice absorptions in LEISA spectra by following the method of Schmitt et al. (2017):

$$BD_{\lambda_1\lambda_2} = 1 - \frac{\int_{\lambda_1}^{\lambda_2} REFF(\lambda)d\lambda}{\int_{\lambda_1}^{\lambda_2} Cont(\lambda)d\lambda} \quad (1)$$

λ_1 and λ_2 are the positions of the right and left shoulders of the absorption bands, listed in Table 2. To limit the effect of random noise, we calculated the shoulder's continuum value by averaging the reflectance of five points around λ_1 and λ_2. *REFF(λ)* is the reflectance at the bottom of the band, integrated over the wavelength range between λ_1 and λ_2, and *Cont(λ)* is the continuum, calculated as a best fit line between the two shoulders.

Table 2: List of absorption bands, with the range of wavelengths used to evaluate the positions of the right and left shoulders for each of them.

Ice	Nominal minimum position	Right shoulder	Left shoulder
CH_4	Range 1 1.30–1.43 μm	1.2929 - 1.3116 μm	1.4205 - 1.4417 μm

* Some feature names mentioned in this paper are now formalized while others are informal

	Range 2 1.59–1.83 μm	1.5777 - 1.6004 μm	1.8202 - 1.8466 μm
	Range 3 1.90–2.00 μm	1.8871 - 1.9147 μm	1.9857 - 2.0149 μm
	Range 4 2.09–2.48 μm	2.0747 - 2.1053 μm	2.4723 - 2.4892 μm
	1.48 μm	1.4681 - 1.4734 μm	1.4895 - 1.5003 μm
CO	1.58 μm	1.5552 - 1.5777 μm	1.5777 - 1.6004 μm
N_2	2.15 μm	2.1207 - 2.1519 μm	2.1441 - 2.1756 μm
H_2O	2.02 μm	1.8371 - 1.8638 μm	2.1647 - 2.1965 μm

223

224

225 **3.2 CH_4 band shifts**

226 Solid nitrogen (N_2) can appear in two different, temperature-dependent states: cubic, or α-,
227 and hexagonal, or β- (e.g., Grundy et al., 1993). N_2 absorption on Pluto is consistent with the β-
228 phase, stable at T > 35.6 K (Quirico & Schmitt, 1997; Grundy et al., 2013).

229 CH_4 and N_2 form complex mixtures on the surface of Pluto since these two ices attract each
230 other at the molecular level. Prokhvatilov and Yantsevich (1983) demonstrated that at Pluto's
231 average surface temperature (40 K), CH_4 and N_2 ice are partly soluble and can form two mixing
232 phases: a CH_4-rich component that is CH_4 saturated with N_2 (CH_4:N_2), and a N_2-rich component
233 that is N_2 saturated with CH_4 (N_2:CH_4). When a small concentration of CH_4 is dissolved within
234 N_2, CH_4 absorption bands show a shift towards shorter wavelengths (Schmitt & Quirico, 1992;
235 Quirico & Schmitt, 1997), with the shift decreasing with increasing amount of CH_4 dissolved in
236 the N_2 (Protopapa et al., 2015). This means that smaller values of the observed CH_4 band shift
237 correspond to higher fraction of pure CH_4 ice.

238 To quantify the amount of CH_4 dissolved in the N_2 matrix for each geologic unit across
239 Sputnik Planitia, we used the following method to estimate the average shift of the CH_4
240 absorptions. We take a pure CH_4 ice spectrum model, with a grain size of 0.5 mm, as reference.

* Some feature names mentioned in this paper are now formalized while others are informal

241 The following procedure is applied to both LEISA and the reference pure CH_4 spectrum. We
242 consider the left and right shoulders of each CH_4 absorption band listed in Table 3 (for the
243 triplets, we considered each local minimum), and we calculated a straight-line continuum
244 between the two shoulders. For each absorption feature (and local minimum), we divided the
245 spectrum by the straight-line continuum. The continuum-removed bands are fit with a cubic
246 spline with an increment of 100 steps, and we assumed the absolute minimum of the spline curve
247 as the band's minimum position. The shift for each minimum is defined as the difference
248 between the pure CH_4 ice and the LEISA spline estimated minima. We have, at the end of this
249 process, eight different band shifts values. From our calculations, and from Schmitt et al. (2017),
250 each individual CH_4 absorption shows a different band's minimum shift. We calculated the
251 average CH_4 band shift parameter by averaging the eight shift values together. The shift towards
252 shorter wavelengths (increasing N_2-rich ice) is indicated by an increasing positive value of the
253 shift index.
254

Table 3: List of **CH_4 absorption bands in the wavelength range covered by LEISA**, with the range of wavelengths used to evaluate the positions of the right and left shoulders for each of them.

CH_4 range	Nominal minimum position	Right shoulder	Left shoulder
Range 1 - triplet 1.30–1.43 μm	1.33 μm	1.3093 μm	1.3453 μm
	1.36 μm	1.3453 μm	1.3827 μm
	1.40 μm	1.3827 μm	1.4200 μm
Single band	1.48 μm	1.4681 μm	1.4949 μm
Range 2 - triplet 1.59–1.83 μm	1.66 μm	1.6271 μm	1.6948 μm
	1.72 μm	1.6948 μm	1.7419 μm
	1.79 μm	1.7419 μm	1.8128 μm
Range 3 - broad band 1.90–2.00 μm	2.20 μm	2.1762 μm	2.2365 μm

255
256

* Some feature names mentioned in this paper are now formalized while others are informal

3.3 Radiative transfer model

The spectra of the geologic units inside each province have been modeled by using a modified version of the Hapke theory (i.e. Hapke et al., 1993; 2012). The Hapke parameters used here are from Verbiscer et al. (2019): the Henyey-Greenstein single particle phase function asymmetry parameter g = -0.36, and the amplitude and width of the opposition surge due to shadow hiding, B_0=0.307 and h=0.206 respectively. Coherent backscatter was not considered in the model. For a full and complete description of the Hapke methodology we employed here, we refer to Cook et al., (2019).

The models consider several endmember components, combined into two spatially separate units by considering an areal mixture. In Tables 4 and 5, the two units are labeled with the letters A and B. Each unit can have one or more endmembers. When more than one endmember is considered, they are intimately mixed together.

As proven by previous work (e.g. Protopapa et al., 2017; Schmitt et al., 2017), CH_4 is ubiquitous within Sputnik Planitia. It can either be diluted within N_2-rich ice, or it can be a pure endmember (Douté et al., 1999; Young et al., 2018). We considered optical constants of CH_4 ice diluted in N_2 ice from Protopapa et al. (2015), and pure CH_4 ice optical constants from Grundy et al. (2002). Pure CH_4 is used here as a substitute for the CH_4-rich component (CH_4:N_2), since previous studies have shown that the wavelength shifts are very small in that phase (Protopapa et al., 2017). N_2 can also appear on the surface as pure ice. We used optical constants from Grundy et al. (1993).

The spectra of several geologic units have a marked negative spectral slope in the wavelength range covered by LEISA. After several attempts to model the negative spectral slope with a wide range of components, we concluded that the optical constants of the clay mineral kaolinite fit this

* Some feature names mentioned in this paper are now formalized while others are informal

spectral feature the best. Figure 4 shows the spectrum of unit drt in Baret montes - the region with the strongest negative spectral slope - compared with seven Hapke models, calculated by considering the optical constants of seven different materials selected to account for the observed negative spectral slope: amorphous carbon, kaolinite, montmorillonite, Pluto tholin, serpentine, Titan tholin, and Triton tholin. Kaolinite returned the best result.

Figure 4: LEISA spectra of unit drt in Baret overlapped by seven Hapke theory-based best fit models, calculated by considering the optical constants of seven different materials to account for the observed negative spectral slope. The spectra are offset for clarity.

This does not mean that kaolinite is present on Pluto's surface, because small structures will scatter greater at shorter wavelengths. For this paper, however, we assume that the negative spectral slope is due to a separate endmember and adopt kaolinite as representative of the negative spectral slope endmember (NSS endmember).

A negative spectral slope can be explained also by physical properties of the surface material, such as a surface coating of ultra-fine grains (Stephan et al., 2017, Protopapa et al. 2020). We do not consider ultra-fine grains in this work, as it is outside the scope of this work.

The NSS endmember is presumed to be a relatively refractory non-ice macromolecular carbon-rich organic material formed by energetic processing of Pluto's atmosphere of CH_4, N_2, CO, and other minor gaseous components, as well as the solid forms of these molecules in the surface ices. Both ultraviolet radiation and charged particles readily transform these simple molecules into disordered macromolecular complexes generally termed tholins. Tholins exhibit a range of yellow-to-red color in the visible spectral region and are thought to account for the red colors of numerous Solar System bodies (e.g., Cruikshank et al. 2005). Materese et al. (2014, 2015) determined the compositions and structures of tholins produced by UV photolysis and low-voltage electron radiolysis of an ice mixture of N_2, CH_4, and CO (100:1:1) relevant to

* Some feature names mentioned in this paper are now formalized while others are informal

Pluto's surface. The radiolytic produced tholin was further analyzed by Cruikshank et al. (2016), demonstrating its negative spectral slope at λ>1.1 μm.

Tholins synthesized in gas phase experiments appropriate for modeling the spectra of the atmospheres of Titan or Triton have positive rather than a negative spectral slope (Khare et al., 1984; 1993; 1994), and do not introduce a sufficiently negative spectral slope in models of LEISA spectra of Pluto's surface units (Figure 4) unless accounting for fine grains. Indeed, Protopapa et al. 2020 reproduces successfully Pluto's MVIC+LEISA observations using Titan tholin like material with ultra-fine grains. As we explained before, we will not explore the contribution of fine grain in this paper. At the same time, there is very little published information on the optical constants for tholins synthesized in ices. Cruikshank et al. (2016) published a reflectance spectrum of the tholin produced by electron radiolysis of the CH_4:N_2:CO ice mixture in the experiments of Materese et al. (2015) considered to be relevant to Pluto's surface. Optical constants were derived from that reflectance spectrum by assuming a grain size of 10 μm (Protopapa et al. 2021). While the derived optical constants for that Plutonian tholin show a subtle negative spectral slope trend, it is insufficient to account for the negative spectral slope found in LEISA spectra (Cook et al., 2019). To test the optical constants of Plutonian tholins, and to compare them to the results obtained with the NSS endmember, we selected four spectra to be modeled with the inclusion of the Plutonian tholin. The results are discussed in detail in Section 4.4. Three of these spectra were taken from unit drt within the Baret, Hillary, and Al-Idrisi Montes provinces, located on the western rim of Sputnik Planitia, as they show particularly negative spectral slope spectra. The last spectrum was taken from unit sh in the Columbia Colles province. This was selected because, even though this unit is located on the eastern perimeter of Sputnik Planitia and was classified as the "scattered hills" unit by White et

* Some feature names mentioned in this paper are now formalized while others are informal

al. (2017), it does show spectral and geomorphological characteristics that are more similar to those of unit drt than to those of other occurrences of unit sh (see Section 5 for further details).

The mountain ranges that line the western perimeter of Sputnik Planitia are **composed** of H_2O ice (Grundy et al., 2016; Protopapa et al., 2017; Schmitt et al., 2017; Cook et al., 2019). We consider both crystalline and amorphous H_2O ice, with optical constants from Grundy & Schmitt (1998) and Mastrapa et al. (2008) respectively.

The optical constants for CH_4:N_2 mixtures, pure β-N_2 and H_2O-ices are known at specific temperature values. The optical constants at intermediate values of temperature are calculated in our models by linearly interpolating the optical constants at measured temperatures, and by searching for the temperature which minimizes the χ^2. However, the changes in χ^2 due to temperature variation are typically small and can confidently constrain the temperature **only** between 40 and 60 K. The temperatures reported in this paper are the best-fit values only.

The endmembers used for each geologic unit in the 15 provinces are listed in Table 4. The first areal mixture (unit 0 in Table 4) includes higher-volatility materials, namely CH_4 (pure or diluted in N_2-rich ice) and pure β-N_2. The second unit (unit 1) includes lower-volatility materials, namely crystalline or amorphous H_2O ice, and NSS endmember.

Figure 5 shows the average LEISA spectra of the geologic units for each province, superimposed on the corresponding model. It must be noted that the model never considers the CO 1.58 μm spectral region because of lack of reliable optical constants (Protopapa et al., 2017). This band corresponds to the (3-0) overtone, which is weaker than the (2-0) band centered at 2.35 μm (seen in ground-based, disk-integrated observations). Even though reliable optical constants are available for the CO spectral region around 2.35 μm, it lies in a gap in our knowledge of the optical constants for CH_4:N_2. Furthermore, the CH_4 bands appear saturated in

* Some feature names mentioned in this paper are now formalized while others are informal

the data, and any attempt to accommodate for the diluted CH_4 optical constants without proper understanding of the bands would likely yield large uncertainties in our fit for the CO band at 2.35 μm.

To understand the areal abundance of the endmembers in each unit, we calculated the areal mass fraction as the product of the endmember's mass fraction with its corresponding fractional area. This parameter represents the surface percentage of each geologic unit covered by each endmember, and it will be used in the compositional maps to indicate the abundance of each endmember in the geologic units (see section 4 for further details).

Table 4: Parameters used to model the LEISA spectra with a modified version of the Hapke theory (i.e. Hapke 1993, 2012).

Province*	T (K)	CH_4 fraction (%)	Component	Unit	Mass fraction	Grain diameter (mm)	Fractional Area	Areal mass fraction (%)
ABM								
Baret Montes	44	1.20	N_2:CH_4	A	1.000	297.9	0.214	**21.4**
			NSS endmember	B	0.467	0.004	0.786	**36.7**
			Crystalline H_2O		0.533	0.20		**41.9**
Cellular plains	45	1.80	Pure CH_4	A	0.003	0.18	0.664	**0.2**
			N_2:CH_4		0.997	70.0		**66.2**
			Crystalline H_2O	B	0.871	5.66	0.336	**29.3**
			Amorphous H_2O		0.129	0.03		**4.3**
Hillary Montes	43	0.25	N_2:CH_4	A	0.007	86.0	0.348	**0.2**
			β-N_2		0.993	120,453.0		**34.5**
			NSS endmember	B	0.426	0.01	0.652	**27.8**
			Crystalline H_2O		0.574	0.331		**37.5**
Southwest buffer	48	1.00	Pure CH_4	A	0.005	0.62	0.817	**0.4**
			N_2:CH_4		0.995	595.7		**81.3**
			Crystalline H_2O	B	1.0	0.01	0.183	**18.3**
Tenzing Montes	50	0.05	Pure CH_4	A	0.015	1.68	0.907	**1.4**
			N_2:CH_4		0.985	58.4		**89.3**
			Crystalline H_2O	B	1.0	0.30	0.093	**9.3**
Zheng He Montes	55	2.90	N_2:CH_4	A	1.0	29.63	0.333	**33.3**
			Crystalline H_2O	B	0.376	4.8E-03	0.667	**25.1**
			NSS endmember		0.624	0.43		**41.6**
Al-Idrisi Montes	44	0.70	N_2:CH_4	A	1.0	120.3	0.646	**64.6**
			Crystalline H_2O	B	1.0	0.01	0.354	**35.4**
BCP								

* Some feature names mentioned in this paper are now formalized while others are informal

Cellular plains	46	0.60	Pure CH_4 N_2:CH_4	A	$2.44 \cdot 10^{-5}$ 1.00	0.004 155.1	1.0	**0.002** **99.998**
				BCT				
Al-Idrisi Montes	44	0.80	N_2:CH_4 β-N_2	A	0.095 0.905	19.719 336.1	0.605	**5.7** **54.8**
			NSS endmember Crystalline H_2O	B	0.353 0.647	0.004 0.153	0.395	**14.0** **25.5**
				DCP				
Cellular plains	44	1.70	Pure CH_4 N_2:CH_4 β-N_2	A	$9.38 \cdot 10^{-5}$ 0.07 0.93	0.33 26.0	0.731	**$6.86 \cdot 10^{-3}$** **4.9** **68.2**
			NSS endmember	B	1.0	0.01	0.269	**26.9**
Al-Idrisi Montes	44	2.30	N2:CH4 β-N_2	A	0.033 0.967	9.208 512.3	0.557	**1.9** **53.9**
			NSS endmember Crystalline H_2O	B	0.467 0.533	0.006 0.071	0.443	**20.7** **23.6**
				DMP				
Baret Montes	47	2.20	Pure CH_4 N_2:CH_4 β-N_2	A	0.001 0.114 0.885	0.332 44.9 1597.9	0.611	**0.1** **7.0** **54.1**
			NSS endmember	B	1.000	0.007	0.389	**38.9**
Hillary Montes	48	1.2	N_2:CH_4	A	1.000	88.000	0.614	**61.4**
			NSS endmember	B	1.000	0.006	0.386	**38.6**
				DPP				
Hillary Montes	48	0.60	Pure CH_4 N_2:CH_4	A	0.001 0.999	0.109 662.8	1.0	**0.1** **99.9**
North pitted plains	45	0.45	Pure CH_4 N_2:CH_4	A	0.0002 0.999	0.021 224.6	1.0	**0.02** **99.98**
Cellular plains	47	0.66	Pure CH_4 N_2:CH_4	A	0.001 0.999	0.087 288.3	1.0	**0.1** **99.9**
East pitted plains	48	4.50	N_2:CH_4 β-N_2	A	0.020 0.980	12.7 1868.6	0.712	**1.4** **69.8**
			NSS endmember	B	1.000	0.022	0.288	**28.8**
South pitted plains	54	7.50	Pure CH_4 N_2:CH_4 β-N_2	A	$3.4 \cdot 10^{-4}$ 0.018 0.982	0.492 12.2 1572.7	0.793	**0.03** **1.4** **77.9**
			NSS endmember	B	1.000	0.025	0.207	**20.7**
West pitted plains	45	0.30	Pure CH_4 N_2:CH_4	A	0.009 0.991	1.949 37.8	1.0	**0.9** **99.1**
				DRT				
Baret Montes	42	0.80	N_2:CH_4	A	1.0	1040.0	0.285	**28.5**
			NSS endmember Crystalline H_2O	B	0.747 0.252	0.003 0.019	0.715	**53.4** **18.1**
Hillary Montes	45	0.60	Pure CH_4 N_2:CH_4	A	0.003 0.997	1.52 296.6	0.389	**0.1** **38.7**
			NSS endmember Crystalline H_2O	B	0.630 0.370	0.005 0.072	0.611	**38.5** **22.6**
Al-Idrisi Montes	42	0.50	Pure CH_4 N_2:CH_4	A	0.001 0.999	0.87 1277.3	0.215 0.215	**$2.3 \cdot 10^{-2}$** **21.5**
			NSS endmember	B	0.637	0.003	0.785	**50.0**

* Some feature names mentioned in this paper are now formalized while others are informal

			Crystalline H_2O		0.363	0.123	0.785	**28.5**
IBM								
Baret Montes	52	2.80	Pure CH_4	A	0.017	0.226	0.317	**0.6**
			N_2:CH_4		0.983	33.9		**31.1**
			NSS endmember	B	0.478	0.007	0.683	**32.6**
			Crystalline H_2O		0.522	0.17		**35.7**
Hillary Montes	52	6.00	Pure CH_4	A	$8.5 \cdot 10^{-6}$	0.271	0.455	$\mathbf{3.9 \cdot 10^{-4}}$
			N_2:CH_4		$4.2 \cdot 10^{-4}$	24.2		**0.02**
			β-N_2		1.000	375,246.0		**45.5**
			NSS endmember	B	0.339	0.007	0.545	**18.5**
			Crystalline H_2O		0.661	0.380		**36.0**
Tenzing Montes	58	5.00	Pure CH_4	A	0.001	0.521	0.606	**0.03**
			N_2:CH_4		0.029	20.2		**1.8**
			β-N_2		0.970	1,513.5		**58.8**
			NSS endmember	B	0.502	0.016	0.394	**19.8**
			Crystalline H_2O		0.498	0.247		**19.7**
Al-Idrisi Montes	47	1.90	N_2:CH_4	A	0.057	11.97	0.437	**2.5**
			β-N_2		0.943	739.4		**41.2**
			NSS endmember	B	0.379	0.005	0.563	**21.3**
			Crystalline H_2O		0.621	0.23		**34.9**
LPP								
Hillary Montes	53	9.10	Pure CH_4	A	$2.1 \cdot 10^{-4}$	0.109	0.592	**0.01**
			N_2:CH_4		0.036	7.312		**2.1**
			β-N_2		0.964	251.4		**57.1**
			NSS endmember	B	0.945	0.047	0.408	**38.5**
			Crystalline H_2O		0.055	0.045		**2.2**
East pitted plains	52	6.10	N_2:CH_4	A	0.014	4.95	1.0	**1.4**
			β-N_2		0.986	761.6		**98.6**
South pitted plains	44	0.4	N_2:CH_4	A	0.624	512.3	1.0	**62.4**
			β-N_2		0.376	159.2		**37.6**
Cellular plains	46	3.00	N_2:CH_4	A	0.029	14.357	0.790	**2.3**
			β-N_2		0.971	1727.4		**76.7**
			NSS endmember	B	1.0	0.007	0.210	**21.0**
Al-Idrisi Montes	49	4.90	Pure CH_4	A	$3.0 \cdot 10^{-4}$	0.254	0.516	**0.02**
			N_2:CH_4		0.031	6.33		**1.6**
			β-N_2		0.969	1217.2		**50.0**
			NSS endmember	B	0.669	0.009	0.484	**32.3**
			Crystalline H_2O		0.331	0.088		**16.0**
PMP								
East pitted plains	49	4.50	Pure CH_4	A	$2. \cdot 10^{-4}$	0.738	0.730	**0.02**
			N_2:CH_4		0.023	13.6		**1.7**
			β-N_2		0.977	2415.3		**71.3**
			NSS endmember	B	1.000	0.018	0.270	**27.0**
Southwest buffer	57	5.20	Pure CH_4	A	0.001	0.346	0.627	**0.1**
			N_2:CH_4		0.079	34.36		**4.9**
			β-N_2		0.920	834.1		**57.7**
			NSS endmember	B	0.560	0.020	0.373	**20.9**
			Crystalline H_2O		0.440	0.461		**16.4**
South pitted plains	48	2.10	N_2:CH_4	A	0.001	61.3	0.668	**0.1**
			β-N_2		0.999	323,181.0		**66.7**
			NSS endmember	B	1.000	0.028	0.332	**33.2**

* Some feature names mentioned in this paper are now formalized while others are informal

Tenzing Montes	58	5.00	Pure CH_4		0.001	0.416		**0.04**
			N2:CH4	A	0.014	14.83	0.792	**1.1**
			β-N_2		0.985	2326.5		**78.1**
			NSS endmember	B	1.0	0.017	0.208	**20.8**
SH								
Astrid Colles	48	4.80	Pure CH_4		$2.4 \cdot 10^{-5}$	23.65		**0.002**
			N_2:CH_4	A	0.020	10.26	0.676	**1.3**
			β-N_2		0.980	1258.8		**66.3**
			NSS endmember	B	1.0	0.022	0.324	**32.4**
Challenger Colles	48	1.40	Pure CH_4		$1.87 \cdot 10^{-4}$	0.644		**0.01**
			N_2:CH_4	A	0.053	39.9	0.680	**3.6**
			β-N_2		0.947	3397.6		**64.4**
			NSS endmember	B	1.0	0.006	0.320	**32.0**
Columbia Colles	52	4.60	Pure CH_4		$2.94 \cdot 10^{-5}$	0.337		**0.001**
			N_2:CH_4	A	0.001	11.849	0.456	**0.05**
			β-N_2		0.999	124,708.0		**45.5**
			NSS endmember	B	0.398	0.005	0.544	**21.7**
			Crystalline H_2O		0.602	0.200		**32.8**
Soyuz Colles	47	4.30	Pure CH_4		$4.92 \cdot 10^{-5}$	1.044		**0.004**
			N_2:CH_4	A	0.016	13.221	0.803	**1.3**
			β-N_2		0.984	2518.6		**79.0**
			NSS endmember	B	1.0	0.007	0.197	**19.7**
East pitted plains	48	3.50	Pure CH_4		$1.20 \cdot 10^{-4}$	0.448		**0.01**
			N_2:CH_4	A	0.026	16.927	0.796	**2.0**
			β-N_2		0.974	2041.8		**77.5**
			NSS endmember	B	1.0	0.013	0.204	**20.4**
SPP								
Hillary Montes	52	3.60	Pure CH_4		$4.87 \cdot 10^{-4}$	0.319		**0.03**
			N_2:CH_4	A	0.070	23.20	0.700	**4.9**
			β-N_2		0.929	652.4		**65.1**
			NSS endmember	B	1.0	0.018	0.300	**30.0**
East pitted plains	50	1.4	N_2:CH_4	A	0.127	70.4	1.000	**12.7**
			β-N_2		0.873	198.6		**87.3**
South pitted plains	44	0.50	Pure CH_4	A	$2.9 \cdot 10^{-4}$	0.09	1.000	**0.03**
			N_2:CH_4		0.990	322.1		**99.0**
North pitted plains	48	0.80	Pure CH_4	A	$2.5 \cdot 10^{-5}$	0.002	1.000	$\mathbf{2.5 \cdot 10^{-3}}$
			N_2:CH_4		1.000	136.6		**99.998**
Cellular plains	48	3.20	Pure CH_4		$2.67 \cdot 10^{-10}$	1.227		$\mathbf{1.9 \cdot 10^{-8}}$
			N_2:CH_4	A	0.038	11.86	0.731	**2.8**
			β-N_2		0.962	1124.0		**70.3**
			NSS endmember	B	1.0	0.011	0.269	**26.9**
Southwest buffer	54	5.00	Pure CH_4		$3.86 \cdot 10^{-4}$	0.409		**0.03**
			N2:CH4	A	0.031	16.473	0.815	**2.5**
			β-N_2		0.968	1010.4		**78.9**
			NSS endmember	B	1.0	0.026	0.185	**18.5**
West pitted plains	44	0.25	Pure CH_4	A	$4.0 \cdot 10^{-3}$	1.6	1.000	**0.4**
			N_2:CH_4		0.996	57.9		**99.6**
TBP								
Cellular	45	1.30	Pure CH_4	A	$7.48 \cdot 10^{-10}$	0.252	0.616	$\mathbf{4.6 \cdot 10^{-8}}$

* Some feature names mentioned in this paper are now formalized while others are informal

plains	N_2:CH_4		0.124	18.62		**7.6**
	β-N_2		0.876	2399.3		**53.9**
	NSS endmember	B	1.0	0.010	0.384	**38.4**

Figure 5: Comparison between LEISA spectra, averaged for each geologic unit in the 15 provinces, and the models calculated by applying the Hapke theory. Each panel also reports the components used in the models, with their fractional area.

4. Spectroscopic Analysis

The spectral indicators obtained from the methodology in Section 3, and the areal mass fraction and grain size of the models' components, are presented as grayscale variation maps. Dark grays are associated with suppressed band depths, or lower areal mass fraction and smaller grain size, and light grays with stronger absorptions and higher areal mass fraction and grain size values.

4.1 CH_4 and N_2

4.1.1 CH_4 band shifts

CH_4 and N_2 are the two most abundant ices on Pluto' surface. Many studies (eg. Prokhvatilov and Yantsevich, 1983; Lunine & Stevenson, 1985; Protopapa et al., 2015) have showed that the phase of the two ices, pure or diluted in each other, depends on the surface temperature. On average, they are most likely to be found in two distinct phases on Pluto's surface (for an average temperature of 44 K): CH_4 saturated in N_2 ice (CH_4:N_2) and N_2 saturated in CH_4 ice (N_2:CH_4). The N_2:CH_4 binary phase diagram, generated from X-ray diffraction experiments by Prokhvatilov & Yantsevich (1983), shows that at Pluto's surface temperature, the solubility limits for the two phases are 3% (of N_2:CH_4) and 5% (of CH_4:N_2). The dilution of CH_4 in the N_2 matrix produces a shift in the minima of the CH_4 absorptions: the smaller the shift, the higher the CH_4 abundance (Protopapa et al., 2015).

* Some feature names mentioned in this paper are now formalized while others are informal

To understand how, and in which ice phase, CH_4 and N_2 are distributed within the geologic units of Sputnik Planitia, we calculated the shift in the LEISA spectra following the method described in Section 3.4, and we show the result in Figure 6.

The highest values of the band shift index in the map refer to areas characterized by N_2-rich ice, while the lowest values indicate CH_4-rich ice. The units with the highest index value are bct in Al-Idrisi Montes and bcp in the Cellular plains. As a general trend, the geologic units in the north and center of the mapping area, especially those within Al-Idrisi Montes and the Cellular plains, have higher values of the shift index than units in the southwest: unit abm in Hillary Montes and Zheng He Montes shows the lowest index values. The central cellular plains of Sputnik Planitia (unit bcp) and unit bct in the northern part of Al-Idrisi Montes are the regions richest in N_2-rich ice. The amount of N_2 slightly decreases from unit bcp to the northern areas of the Cellular plains (units dcp and tbp), and to the lpp unit of the South and East pitted plains. The shift index decreases - and consequently so does the N_2-rich ice abundance – to the west, incorporating units ibm and dmp in Hillary Montes, pmp and abm in Southwest buffer, and abm, ibm and pmp in Tenzing Montes. The units covering the southernmost and easternmost areas of the South and East pitted plains (dpp, pmp, and spp) have index values around 0.004, the transition point between the N_2-rich and CH_4-rich ices. This north-to-south trend of increasing N_2 abundance has previously been noted by S chmitt et al., (2017), and Protopapa et al. (2017).

Figure 6: Variation of the CH_4 band shift index across the geologic units of Sputnik Planitia. The highest values of the band shift index in the map (light grey) indicate areas characterized by N_2-rich ice, while the lowest values (dark grey) indicate CH_4-rich ice.

4.1.2 CH_4 from LEISA spectra

* Some feature names mentioned in this paper are now formalized while others are informal

406 CH_4 ice displays a large number of absorption bands in Pluto's spectra, organized in triplets or
407 in single broad bands (Figure 3 and Tables 2 and 3). We used equation 1 to calculate the
408 integrated band depths of each CH_4 signature listed in Table 2, and we present them in Figure 7.
409 The areas with the most suppressed absorptions in almost all CH_4 ranges considered - Range
410 1, Range 2, Range 4, and 1.48 μm (Fig. 7 a,b,d,e) - are units drt and bct in Al-Idrisi Montes, and
411 units drt and abm in Baret Montes. Hillary and Tenzing Montes, on the other hand, show deeper
412 CH_4 absorptions, with values similar to units bct and dcp. At 1.48 μm, units bcp and dcp of the
413 Cellular plains and unit lpp of the South and East pitted plains have similar band depth values. In
414 CH_4 Range 1, Range 2, and Range 4 this similarity also extends to units lpp and pmp of the
415 South and East pitted plains.
416 In many **aspects**, the CH_4 Range 3 map (Fig. 7c) appears to be the inverse of the other four
417 panels: the absorption bands are more suppressed in units bcp, dcp, and tbp of the Cellular
418 plains, where the intensities are similar to Al-Idrisi and Baret Montes, and in unit bct of Al-Idrisi
419 Montes. Furthermore, the CH_4 absorption is deeper in the Southwest buffer and Tenzing Montes
420 provinces.
421 Schmitt et al. (2017) found the same trend observed here for the four ranges of CH_4 triplets:
422 the intensity of the CH_4 bands is high inside units bcp and dcp of the Cellular plains in Ranges 1,
423 2, and 4, whereas the strength of the band in Range 3 decreases in the very same areas, but not in
424 the southwestern territories corresponding to the Southwest buffer and Tenzing Montes
425 provinces.

426 Fig. 7: Maps of variation of the integrated band depths of the main CH_4 absorptions*: Range 1 (1.30-1.43 μm; A), Range 2*
427 *(1.59-1.83 μm; B), Range 3 (1.90-2.00 μm; C), Range 4 (2.09-2.48 μm; D), and the single band at 1.48 μm (E). The Range 3 map*
428 *(C) shows opposite trends compared to the other four spectral ranges, a behavior that was previously observed in other studies*
429 *(e.g. Schmitt et al, 2017).*
430

431 *4.1.3 CH_4 from model spectra*

* Some feature names mentioned in this paper are now formalized while others are informal

Figure 8 displays the amount of CH_4 diluted in the N_2-rich phase (panel a) and the temperatures (panel b) estimated by the models. The maps in Figure 8a and 8b show that the amount of CH_4 diluted in N_2 and the temperature are both very low in the northern, western, and central regions of Sputnik Planitia, and increase in the south and west. A similar trend was already found by Protopapa et al. 2017 (see their figure 5 panel C). The highest temperature and CH_4 content are found in unit lpp of Hillary Montes. Here the concentration of CH_4 reaches 9.1%, with an estimated temperature of 53 K. Units dpp in South pitted plains, lpp in East pitted plains, ibm in Hillary Montes, pmp and spp in Southwest buffer, and pmp and ibm in Tenzing Montes have CH_4 content between 5% and 7%, and high temperatures, between 52 and 58 K. The remaining provinces across the mapping area show CH_4 content below 5%, reaching a minimum in unit lpp of South pitted plains (0.4%), dpp of West pitted plains (0.3%) and abm of Tenzing Montes (0.05%). CH_4 in unit dcp in the Cellular plains accounts for 0.06%, which increases to 1.3% and 1.7% in units tbp and dcp respectively.

Units abm in Zheng He Montes and pmp in Tenzing Montes, Baret Montes, and Southwest buffer have the highest temperatures, ranging between 55K and 58K. Units drt, bct and dcp, on the other hand, show temperatures ranging between 43 and 45 K.

The fraction of CH_4 diluted in N_2 estimated in the models, and the corresponding predicted temperatures are consistent with the results from Protopapa et al. (2017), which showed a dilution content of CH_4 in N_2 in the Sputnik Planitia region ranging between 0.1% and 5%.

Pure CH_4 can also be found in Sputnik Planitia but always in very small amounts, below 1.5% (Figure 9a and b). The grain size ranges between 0.004 and 2 mm. Only one unit shows a larger grain size, sh in Astrid Colles (23.6 mm).

* Some feature names mentioned in this paper are now formalized while others are informal

Fig. 8: *Maps of percentage variation of CH_4 diluted in N_2-rich ice (A) and temperatures (B) estimated by the spectral modeling.*

Fig. 9: *Maps of variation of pure CH4 areal mass fraction (A) and grain size (A) estimated by the spectral modeling. Pure CH4 covers almost all geologic units in Sputnik Planitia, but its percentage is very low, below 1.5%.*

4.1.4 N_2 from LEISA spectra

N_2 was discovered on the surface of Pluto through the detection of its absorption band at 2.15 µm (Owen et al., 1993), located in a spectral region dominated by the CH_4 Range 4 absorption (Figure 3). This band is relatively weak, and the fact that it is clearly observed in almost all Pluto's spectra means that the N_2 layer is thick enough to allow the light to travel for a significant path length (on the order of centimeters) before being absorbed or reflected (Grundy et al., 1993; Cruikshank et al., 2015). The strong absorptions of CH_4, on the other hand, only need a layer some microns thick to be clearly observable in a spectrum. N_2 is, therefore, the most abundant ice on Pluto's surface, and it is contaminated by smaller amounts of CH_4, CO and other minor constituents (Cruikshank et al., 1984).

The 2.15 µm integrated band depth variation map is shown in Figure 10.

The deepest N_2 absorptions are localized in small areas, namely in unit bct at the northern end of Al-Idrisi Montes, and in spp of the West pitted plains. Unit bcp of the Cellular plains, and units lpp and spp in the South pitted plains, also show deep N_2 absorptions. The band intensity decreases northwards, in units dcp and tbp of the Cellular plains, eastward, in units lpp, dpp and pmp of the E pitted plains, and southwards, in units dpp and pmp of the S pitted plains. The western areas have, on average, weaker or even null N_2 absorption. In fact, unit abm in Hillary and Tenzing Montes shows negligible amounts of N_2. Low N_2 content is also observed in units abm and drt of Al-Idrisi Montes, abm of Zheng He Montes, and all the units of Baret Montes, Southwest buffer and Tenzing Montes. In the east, Challenger Montes show similar, suppressed intensities, standing out from its surroundings. A comparison with Figure 6, shows that the very

* Some feature names mentioned in this paper are now formalized while others are informal

same provinces with weak N_2 absorptions also have small values of the shift parameter, confirming the prevalence of CH_4-rich ice.

Fig 10: Map of variation of the integrated band depth of N_2 at 2.15µm.

4.1.5 N_2 from model spectra

For the temperature values estimated by the models, the phase diagram suggests that most N_2 within Sputnik Planitia is in the form of N_2:CH_4 ice. The N_2-rich phase can coexist with increasing amounts of pure N_2 in the β-form if the temperature rises.

Figure 11 and Figure 12 show the areal mass fraction, in the "A" panels, and the grain size, in the "B" panels, of N_2:CH_4 ice and of pure β-N_2 respectively.

From Figure 11a, we can observe high amounts of N_2:CH_4 covering the very central regions of Sputnik Planitia, corresponding to units bcp in the Cellular plains and lpp and spp of the South pitted plains. In the West, units abm of Al-Idrisi Montes, dpp of West pitted plains and Hillary Montes, abm of Southwest buffer and Tenzing Montes also show high abundance of N_2. In the remaining territories, the areal mass fraction of N_2-rich ice decreases sharply, dropping below 10%. A similar trend was observed in Protopapa et al. (2017). However, the difference in the absolute numbers of abundance are to be attributed to differences in the modeling (e.g., Hapke parameters, areal versus intimate mixture). The geologic units where N_2:CH_4 abundance is low, though, correspond to areas where pure β-N_2 has high concentrations (Figure 12a). Units dcp and tbp in the northern part of the Cellular plains, bct and ibm in Al-Idrisi Montes, abm, ibm and spp in Hillary Montes, pmp and and spp in Southwest buffer, ibm and pmp in Tenzing Montes, and lpp, dpp, spp, and pmp of East and South pitted plains have pure β-N_2 areal mass fraction ranging between 35.4% and 98.6%.

* Some feature names mentioned in this paper are now formalized while others are informal

The grain size of the N_2:CH_4 ice is below 200 mm in most provinces. Some units in the west show, on the other hand, coarser grain sizes, reaching 800 mm. For pure β-N_2, the grain size is always very large, on average above 350 mm.

Fig. 11 Maps of variation of N_2:CH_4 areal mass fraction (A) and grain size (B) estimated by the spectral modeling.

Fig. 12 Maps of variation of pure β-N_2 areal mass fraction (A) and grain size (B) estimated by the spectral modeling.

4.1.6 Distribution of CH_4-rich and N_2-rich ices

The distribution of CH_4-rich and N_2-rich ices can be inferred by integrating the abundance maps shown previously with correlation plots between the CH_4-band shift index and the CH_4 and N_2 integrated band depths.

Figure 13a shows the scatter plots of the CH_4 integrated band depths in Ranges 1 (top panel), 2 (middle panel), and 4 (bottom panel) versus the CH_4 shift index. We grouped these spectral indices together because they show similar trends with the band position index. The points are organized in two groups, separated in the plots by a dotted line. The first group (G1), above the line, shows increasing band strength with increasing values of the shift parameter. The second group (G2), below the dotted line, also shows a positive trend, but the points are more dispersed. Furthermore, the values of the CH_4 integrated band depths in G2 are lower than the units in G1. The Pearson correlation coefficient calculated for the data belonging to G1 and G2 confirm the positive correlations. For G1, CH_4 Range 1 has a moderate correlation with the CH_4 shift (ρ = 0.44), while for Range 2 (ρ = 0.78) and Range 4 (ρ = 0.82) the correlation coefficient has higher values. The points belonging to G2 appear more dispersed, but a positive trend is still visible. The correlation coefficient is ρ = 0.24 for the Range 1, ρ = 0.62 for the Range 2, and ρ = 0.74 for the Range 4.

* Some feature names mentioned in this paper are now formalized while others are informal

The units included in G1 show increasing shift index with integrated band depths associated with a west-east trend. The units covering the western provinces show the most suppressed CH_4 absorptions in Ranges 1, 2, and 4, and smaller values of the shift index. Moving toward the central and eastern territories, the two spectral parameters increase in value.

Group G2 includes **the following** units, in order of increasing values of the shift index and integrated band depths: drt, ibm, abm of Baret Montes, drt of Al-Idrisi Montes, sh of Columbia Colles, drt of Hillary Montes, abm of Al-Idrisi Montes, tbp of the Cellular plains, and lpp, ibm, bct, and dcp of Al-Idrisi Montes. All these units, excepting sh and tbp, are located on the western edge of Sputnik Planitia.

The depth of an absorption band **is controlled by several physical parameter**, primarily the amount of ice, grain diameter, and the single particle phase function. Generally, the greater the amount of ice, or the larger the grain size, or the more a grain scatters incident sunlight preferentially in the forward direction (Verbiscer et al., 2006), the deeper the absorptions.

To examine the influence of the scattering on the best fit models, we examined the H-band (1.59-1.82 μm) range of the spectrum from spp unit of North Pitted Plains. We used this spectrum because the surface is mostly smooth (i.e. no mountains slopes) and likely minimizes changes in the spectrum due to phase, emission or incidence angles**. We find that changes in the Henyey-Greenstein *g*-value affects best-fit parameters like temperature and dilution**. Because we adopt the global value for the Henyey-Greenstein *g*-value from Verbiscer et al (2019) which is based on a fit to visible, not near-infrared, data at 0.55 μm, our best-fit values for temperature and dilution should be considered preliminary, as additional analysis would be required to understand the local *g*-values in the H-band in each region we examined. For the

* Some feature names mentioned in this paper are now formalized while others are informal

scope of this paper, we will focus on abundance and grain size variation as the main parameters **controlling** the spectra shape and the bands depth.

Based on the abundance relationship alone, we might be led to conclude from Figure 13a that the increase in CH_4 band strength with the CH_4-shift index is due to an increase in CH_4 abundance. When the shift index was presented in section 3.2, though, we specified that higher index values correspond to lower amounts of CH_4-rich ice. Therefore, a trend in abundance, opposite of what observed in Figure 13a, is expected if grain scattering properties are not taken into account: the CH_4 integrated band depth should be less intense - or, the abundance of CH_4 should decrease - with increasing values of the shift index. This trend, then, can be explained by a difference in the scattering properties of particles within spectral Ranges 1, 2, and 4.

Figure 13b displays the integrated band depths of CH_4 Range 3 (top panel), 1.48 μm band (middle panel), and N_2 absorption band at 2.15 μm (bottom panel). In contrast to the three plots in Figure 13a, these spectral parameters show a clear and single trend with the CH_4 shift index.

As we observed in Figure 7, the CH_4 Range 3 absorption shows a very different abundance distribution across Sputnik Planitia compared to the other CH_4 absorptions. This discrepancy is also reflected in the plots showed in Figure 13b, where the intensity of the band shows a decrease in strength with increasing band shift, consistent with the definition of the CH_4 shift index. The Pearson correlation coefficient between Range 3 and the shift index is equal to -0.67, proving that an anti-correlation exists. We also observe that the band intensity decreases from the western to the central and eastern units, indicating a higher abundance of CH_4-rich ice in the western mountain ranges. Some exceptions are observed: units abm, ibm, and lpp of Al-Idrisi Montes have CH_4 absorption values in Range 3 similar to the Cellular plains, South and East pitted plains, and the four Colles provinces, while units bct and dcp have the most suppressed band

* Some feature names mentioned in this paper are now formalized while others are informal

values. The **scatter plot of the** CH_4 band at 1.48 μm **as a function of the CH_4 band shift results in an elongated cloud, without any measurable slope**, but rather a flat trend. The correlation coefficient is indeed $\rho = -0.12$. Finally, the bottom panel of Figure 13b shows a positive correlation ($\rho = 0.68$) between the intensity of the N_2 band at 2.15 μm and the CH_4 band shift: the abundance of N_2-rich ice increases where the CH_4-shift index has higher values.

The unexpected behavior of the strongest CH_4 absorptions (Ranges 1, 2, 4) has been previously observed, mainly in Schmitt et al. (2017). The authors compared the strength of the CH_4 main absorptions with a CH_4-band shift parameter and observed that the data relative to Sputnik Planitia were offset with respect to the rest of Pluto's surface.

The absorptions plotted in Figure 13A do not increase, or decrease, in depth linearly with a variation of abundance of CH_4, grain size or forward scattering, but they anyway tend to saturate quickly with increasing abundance of CH_4, or with increasing grain size or forward scattering. Therefore, these three ranges cannot reliably be used to infer the CH_4 abundance and, in turn, to understand if abundance or grain size can in fact explain the unexpected trend. The absorption in Range 3 and the band centered at 1.48 μm are weaker, and a larger quantity of CH_4 would be necessary to make them saturated. Therefore, the plots in Figure 13B are more reliable for understanding how CH_4-rich and N_2-rich ices distribute across Sputnik Planitia. Furthermore, the trends in Figure 13B are consistent with the results from the models shown in Figures 8, 11 and 12. The geologic units with the lowest value of the shift index are mostly located in the southwestern mountain ranges, mainly Hillary and Zheng He Montes. Indeed, the models for units abm and ibm of these areas show **the highest** concentration of CH_4-rich ice. The central part of the Cellular plains and the East and South pitted plains show high abundance of N_2:CH_4 ice or of pure β-N_2, as well as high values of CH_4-shift index and of N_2 integrated band depth.

* Some feature names mentioned in this paper are now formalized while others are informal

598 The hypothesis we can formulate to understand the trends of Figure 13A, based on the data
599 shown thus far, is that N_2 and CH_4 are mixed with, or in close contact with patches of, some
600 contaminants, or that there are differences in the single particle phase functions. The effect of
601 these materials or surface particles that are more backscattering would be to suppress the CH_4
602 band depths - leaving the band shift unaltered - on the western regions where they may be more
603 exposed and, therefore, more abundant. The CH_4 band at 1.48 μm is minimally affected by
604 contaminants since its trend represents a transition between the absorptions in Figure 13A and
605 the CH_4 absorption in Range 3 of Figure 13b. This last feature doesn't seem to be sensitive to
606 contaminants, but rather to a variation in the abundance of CH_4 or N_2 ices.
607 To support this idea, we plotted the CH_4 integrated band depths in Ranges 1, 2, and 4 against
608 the CH_4 integrated band depth in Range 3 (Figure 14). The three plots clearly show a lack of
609 correlation between the represented parameters, the Pearson coefficients being $\rho = 0.34$ (Range
610 1), $\rho = 0.11$ (Range 2), and $\rho = 0.01$ (Range 4). The low or null correlations suggest that the
611 **physical property controlling** the depth of the CH_4 absorptions in Ranges 1, 2, and 4 is not
612 affecting the absorption in Range 3. Because of the different sensitivity of the four ranges to the
613 variation in CH_4 ice abundance and grain size, we can exclude these two **physical** parameters as
614 the main reason for the trend observed in Figure 13a.
615 It is worth noticing from Figure 14 that units bct and dcp in Al-Idrisi Montes have the most
616 suppressed absorptions in Range 3, but quite intense values in Ranges 1, 2, and 4. Indeed, these
617 two units show the deepest bands among the units belonging to group G2 (Figure 13A). Unit drt
618 in Baret and Al-Idrisi Montes has very suppressed bands in all CH_4 ranges, while in Hillary
619 Montes the same unit has quite deep absorption in Range 3, but weak intensities in the other CH_4
620 ranges.

* Some feature names mentioned in this paper are now formalized while others are informal

Fig 13: ***(A)*** *Scatter plot showing the correlation between the CH_4 integrated band depth in Ranges 1 (top), 2 (middle), and 4 (bottom) with the CH_4 shift index. The data are split into two groups, separated by a dotted curve. The points belonging to group G1, above the curve, show increasing band strength with increasing values of the shift parameter. The second group (G2), below the dotted line, also shows a positive trend, but the points are more dispersed. Furthermore, the values of the CH_4 integrated band depths in G2 are lower than the units in G1. The positive trends in both groups contradicts the definition of the CH_4 shift index, i.e. higher index values correspond to lower of CH_4-rich ice amount. Therefore, a trend opposite of what observed in panel A is expected: the CH_4 integrated band depth should be less intense - or, the abundance of methane should decrease - with increasing values of the shift index.* ***(B)*** *Scatter plot showing the correlation between the CH_4 integrated band depth in Range 3 (top), at 1.48 μm (middle), and the N2 integrated band depth at 2.15 μm (bottom) with the CH_4 shift index. As opposite to the three plots in panel A, these spectral parameters show a clear and single trend with the CH_4 shift index, in agreement with the definition of the CH_4 shift index.*

Fig 14: *Scatter plot showing the correlation between the CH_4 integrated band depths in Ranges 1 (top), 2 (middle), and 4 (bottom) versus the CH_4 integrated band depth in Range 3. The plots clearly show a lack of correlation between the represented parameters, indicating that the factor influencing the depth of the CH_4 absorptions in Ranges 1, 2, and 4 doesn't have any (or it has negligible) effect on the absorption in Range 3.*

4.2 CO

Figure 15 displays the spatial distribution **of the CO absorption** across Sputnik Planitia, centered at 1.58 μm. The **CO absorption is generally weak; the** deepest **ones** occur in units abm in Southwest buffer and units lpp and spp on the eastern perimeter of the Cellular plains. Unit bcp in the Cellular plains, units ibm and pmp in Tenzing Montes, and units lpp and spp in the South and East pitted plains, also show high CO content. The band intensity decreases in the northern portion of Sputnik Planitia, in units dcp and tbp, and in the eastern and southern units of the South and East pitted plains, dpp and pmp. The regions mostly depleted in CO (where the integrated band depth is close to 0) are units abm in Zheng He and Hillary Montes, and drt in Baret Montes. CO content in Al-Idrisi Montes is low and quite constant in all its geologic units, excepting bct, where the band intensity decreases even more. The CO distribution in the Cellular plains, South and East pitted plains, Hillary Montes, and Baret Montes closely resembles the N_2 trend observed in Figure 11. Other areas, on the other hand, show an anti-correlation with the N_2 distribution. The most remarkable differences are observed for units bct and ibm in Al-Idrisi Montes, in the North and West pitted plains, and in the abm units of the Cellular plains, Southwest buffer and Tenzing Montes.

* Some feature names mentioned in this paper are now formalized while others are informal

More complex is the comparison with the CH_4 integrated band depth maps of Figure 7. As we described before, CH_4 absorptions are deeper in Ranges 1, 2, 4 and in the 1.48 μm band in the Cellular plains and South and East pitted plains provinces, and in some units of Hillary Montes and Southwest buffer. Units abm and drt of Al-Idrisi and Baret Montes instead show the weakest CH_4 absorptions. The CO integrated band depth map shows the same trend in the very same provinces. CH_4 Range 3, on the other hand, shows the opposite results, the band being more intense where the other CH_4 and the CO absorptions are shallower.

We investigated the correlation between CH_4 and N_2 absorptions with CO in Figure 16. The scatter plot of CH_4 in Ranges 1, 2, and 4 versus the CO integrated band depth is displayed in Figure 16a. On average, CO correlates well to the three CH_4 absorptions, the Pearson linear correlation coefficient being 0.64 for Range 1, 2, and 4. We notice, though, that the units do not distribute in the same way, but they can be split into two groups, separated in the three panels of Figure 16a by a vertical dotted line. The units on the left side have a sparse distribution and no apparent trend. They are all located on the western edge of Sputnik Planitia, excepting unit tbp in the Cellular plains and unit sh in Columbia Colles. The points on the right portion of the plots belong to units in the central and eastern parts of Sputnik Planitia, excepting the Southwest buffer and Tenzing Montes. For these units, the correlation between the integrated band depths of CO and CH_4 is also not evident, having a flat distribution.

Figure 16b shows the CO integrated band depth plotted against the integrated band depth of CH_4 in Range 3 and at 1.48 μm, and of N_2. The only clear correlation occurs between CO and the band at 1.48 μm, with ρ=0.53, while the correlation coefficient for CH_4 band in Range 3 and N_2 are negligible, being 0.09 and 0.12 respectively.

* Some feature names mentioned in this paper are now formalized while others are informal

If we compare these results with Figure 13, we can notice some similarities. CH_4 in Ranges 1, 2, and 4 showed an unexpected trend in Figure 13a, the absorptions becoming deeper with increasing values of the CH_4 shift parameter. The abundance of CH_4 or its grain size cannot explain the discrepancy, since they weakly influence the depth of those bands. CH_4 in Range 3 and N_2, on the other hand, have a trend consistent with the definition of the CH_4 shift index: low values of the index indicate dominance of CH_4-rich ice, while high values of the index imply high abundances of N_2-rich ice.

Comparing Figure 13a with Figure 16a, we observe that geologic units showing deeper CH_4 absorptions and higher values of the CH_4 shift index also have strong CO bands. Similarly, units having a random distribution in Figure 13a (group G2) also have a sparse distribution and low CO values in Figure 16a (on the left side of the dotted line). **The top and bottom panels of Figure 16b are not useful for any definitive interpretation, since the CO integrated band depth doesn't have any clear correlation with either integrated band depth of CH_4 in Range 3 or N_2.**

Grundy et al. (2013, 2014), and Schmitt et al. (2017) noticed that CO is almost absent in areas dominated by CH_4-rich ice, but it is abundant in N_2-rich areas. The comparison of the CH_4 shift index map in Figure 6 with the CO map in Figure 15 leads to the **confirm** of the authors' conclusion for almost all geologic units in Sputnik Planitia, with a few exceptions. Units bct in Al-Idrisi Montes, drt in Baret and Hillary Montes, and dpp and spp in the West pitted plains are the most evident: CO absorption is suppressed where the shift indicates dominance of N_2-rich ice.

The correlation between CO and N_2 is also evident when comparing Figure 15 with the N_2:CH_4 (Figure 11a) and pure β-N_2 (Figure 12a) maps. Units with high amounts of N_2-rich ices,

* Some feature names mentioned in this paper are now formalized while others are informal

like bcp and dcp in the Cellular plains, and spp in South pitted plains, or with considerable presence of pure β-N_2, such as lpp in East pitted plains, have strong CO intensities. We also notice that the CO band is weaker where no pure β-N_2 is observed, like Zheng He Montes, and drt in Baret Montes.

Fig. 15: Map of variation of CO integrated band depth at 1.58 µm.

Fig 16: ***(A)*** *Scatter plot showing the correlation between the CH_4 integrated band depth in Ranges 1 (top), 2 (middle), and 4 (bottom) with the CO integrated band depth. Because rhe data shows to different trends, we split them into two groups, separated by a vertical dotted line. The units on the left side have a positive trend but a sparse distribution, the points on the right portion of the plots show a flat distribution.* ***(B)*** *Scatter plot showing the correlation between the CH_4 integrated band depth in Range 3 (top), at 1.48 µm (middle), and the N_2 integrated band depth at 2.15 µm (bottom) with the CO integrated band depth. The only clear correlation occurs between CO and the band at 1.48 µm, while the correlation coefficient for CH_4 band in Range 3 and N_2 are negligible.*

4.3 H_2O

The presence of crystalline H_2O ice on Pluto's surface was investigated and proved by numerous works, e.g. Grundy et al. (2016), Protopapa et al. (2017); Cook et al. (2019), and Cruikshank et al. (2020).

In our models we consider H_2O ice in two forms, crystalline and amorphous.

The spatial variation of the crystalline H_2O ice as predicted in the models is presented in Figure 17. The left panel (Figure 17a) depicts the areal mass fraction, the right panel (Figure 17b) the grain size. The mountain ranges extending along the western boundary of Sputnik Planitia are the only provinces hosting crystalline H_2O ice, excepting Columbia Colles in the east. The H_2O ice abundance ranges between 2% and 42%.

Unit abm in the mountain ranges of Baret and Hillary Montes show the highest percentage of crystalline H_2O ice (37% to 42%). Al-Idrisi Montes displays a lower percentage, ranging between ~25% and ~35% across its constituent units. The units in Southwest buffer and Tenzing Montes, and the drt unit in Baret Montes, show a decrease in crystalline H_2O ice, being between ~9% and ~18%. The grain size in all the units is smaller than 6 mm. The largest grains are found

* Some feature names mentioned in this paper are now formalized while others are informal

in the Southwest buffer, followed by Hillary and Tenzing Montes. In all the other units, the crystalline H_2O ice grain size is estimated to be smaller than 0.2 mm.

The estimate of the amount of H_2O ice from LEISA data is not a trivial task. Indeed, the main H_2O ice absorptions occur at 1.5 µm, the location of the gap in the CH_4:N_2 optical constants, and at 2.02 µm, where CH_4 shows stronger absorptions with increasing wavelengths. Furthermore, the absorption around 2.0 µm is partly cut out by the optical constants gap. Keeping this in mind, we calculated the H_2O integrated band depth by applying equation 1 with the parameters listed in Table 2 for the spectra of the geologic units having crystalline H_2O predicted by the models.

Fig. 17: Maps of variation of Crystalline H_2O areal mass fraction (A) and grain size (B) estimated by the spectral modeling.

Figure 18 shows the mutual variation of the crystalline H_2O areal mass fraction, the H_2O integrated band depth, and the CH_4 shift parameter. Crystalline H_2O ice correlates well to the H_2O integrated band depth (top, left panel; ρ=0.55). No correlation, on the other hand, exists between the H_2O areal mass fraction (top, right panel), the H_2O integrated band depth (bottom, left panel), and the shift parameter (ρ=-0.04 and ρ=-0.05), suggesting that H_2O does not influence the CH_4 band shift.

Fig. 18: *Mutual variation of the crystalline H_2O areal mass fraction, the H_2O integrated band depth, and the CH_4 shift index. Crystalline H_2O ice well correlates with the H_2O integrated band depth (top, left panel), while no correlation exists between the H_2O areal mass fraction (top, right panel) and the H_2O integrated band depth (bottom, left panel) and the shift parameter, suggesting that H_2O do not influence the CH_4 band shift.*

The correlation between H_2O spectral indicators and CH_4 and N_2 integrated band depths is explored in Figure 19.

CH_4 integrated band depths in Ranges 1, 2, and 4 (Figure 19a-f) show a moderate anti-correlation with the crystalline H_2O areal mass fraction (panels a, b, c), and a strong anti-

* Some feature names mentioned in this paper are now formalized while others are informal

753 correlation with the H_2O integrated band depth (panels d, e, f). Pearson correlation coefficient
754 ranges between -0.90 and -0.96 for the plots on the right panels.
755 The correlation is less strong for the integrated band depths of CH_4 in Range 3 and at 1.48
756 μm, and N_2 at 2.15 μm. In the three left panels of Figure 19 (panels g, h, i), the Pearson
757 coefficient's values are in the interval -0.26 to -0.33, while in the panels on the right (j, k, l) the
758 parameter ranges between -0.06 and -0.78.
759 The geologic units having H_2O ice are the same forming group G2 in Figure 13a, or placed on
760 the left side of group G1, characterized by low integrated band depths and low shift index values.
761 The negative correlation observed in Figure 19a-f suggests that H_2O ice can contribute to the
762 suppression of the strong CH_4 ice absorptions and can explain the anomalous trend observed in
763 Figure 13a. For some units, though, H_2O is **neither** the only, **nor** the main, contributor.
764 Unit drt in Al-Idrisi and Baret Montes has the strongest absorptions in the 2.0 μm region, but
765 with moderate fractions of crystalline H_2O ice (28.5% and 18.1% respectively). The same is
766 observed for unit abm in Zheng He and Hillary Montes. The discrepancy **between the**
767 **crystalline H_2O areal mass function and the H_2O integrated band depths** suggests that
768 crystalline H_2O is contributing to the absorption around 2.0 μm, but the influence of some other
769 material must be invoked to justify such deep absorptions in this spectral area. Because CH_4
770 integrated band depths are also very suppressed, we can deduce that H_2O and other contaminants
771 are influencing the CH_4 **absorptions** in Ranges 1, 2, and 4 as well. Previous work (e.g.
772 Cruikshank et al., 2015; Schmitt et al., 2017; Protopapa et al., 2017) has noticed a correlation
773 between H_2O ice and tholins on Pluto, which in Sputnik Planitia is seen at the low-latitude
774 mountain ranges of western Sputnik Planitia. It is therefore likely that tholins, or **other material**
775 **with a positive spectral slope**, is significantly contributing to the suppression of CH_4

* Some feature names mentioned in this paper are now formalized while others are informal

absorptions in Ranges 1, 2, and 4 in units like drt of Baret and Al-Idrisi Montes, and abm in Zheng He and Hillary Montes.

Unit drt in Hillary Montes shows weaker H_2O integrated band depth than the drt units in the other two provinces, but crystalline H_2O accounts for 22.6% of the total composition. The area of unit drt in Hillary Montes is less extensive than the units in Baret and Al-Idrisi Montes, and it is surrounded by units abm and ibm. Unit abm in Baret, Hillary and Zheng He Montes has the highest percentage of crystalline H_2O and significant H_2O absorption.

The amount of H_2O ice decreases moving south from the northwestern mountain ranges. Unit ibm shows a lower, but still considerable, amount of H_2O ice than abm. The lowest abundance of H_2O ice is seen in units lpp in Hillary Montes, abm and ibm in Tenzing Montes, lpp in Al-Idrisi Montes, and pmp and abm in Southwest buffer. These regions also show medium to low CO content, with the exception of unit abm in Southwest buffer, for which the CO integrated band depth has the deepest value (Figures 15 and 16).

Fig 19: ***(A-F)*** *Scatter plot showing the correlation between the CH_4 integrated band depth in Ranges 1 (top), 2 (middle), and 4 (bottom) with the H2O crystalline areal mass fraction (A, B, C), and with the H_2O integrated band depth (D, E, F). All the represented parameters show clear anti-correlations, suggesting that water ice can contribute to the suppression of the strong methane ice absorptions. For some units, though, H_2O is not the only, or the main, contributor. Unit drt in Al-Idrisi and Baret Montes, and unit abm in Zheng He and Hillary Montes have the strongest absorptions in the 2.0 µm region, but moderate fractions of crystalline water ice. The discrepancy between the two water ice parameters suggests that crystalline H_2O is contributing to the absorption around 2.0 µm, but the influence of some other material must be invoked to justify such deep absorptions in this spectral area.* ***(G-L)*** *Scatter plot showing the correlation between the CH_4 integrated band depth in Ranges 3 (top), at 1.48 µm (middle), and N_2 integrated band depth at 2.15 µm (bottom) with the H_2O crystalline areal mass fraction (G, H, I), and with the H_2O integrated band depth (J, K, L). The correlation between these parameters is less pronounced than in the previous panels, and indication that crystalline H_2O minimally influence the depth of the CH_4 absorptions in Range 3 and at 1.48 µm, and of N_2.*

4.4 ***Negative spectral slope*** *materials: NSS endmember and Pluto tholins*

The MVIC instrument of the Ralph spectrometer revealed an extended region of material with positive spectral slope and low albedo, named Cthulhu Macula (Buie et al., 2010; Grundy et al., 2016), the existence of which was also inferred from previous ground-based observations (Cruikshank et al., 2015). This material also covers the low-latitude mountain ranges of western

* Some feature names mentioned in this paper are now formalized while others are informal

Sputnik Planitia, seen here in units drt, abm and, in smaller amounts, ibm (Schmitt et al., 2017). This material is interpreted to be tholins, organic compounds that assume colorations in the visible spectrum - from yellow, to red, to brown - when bombarded with high-energy electrons or UV radiation. Tholins don't have a clear spectral feature in the NIR range, but they can **weaken** the CH_4 **absorption** band at 2.32 μm, within Range 4 (Schmitt et al., 2017), when the two are mixed together. Comparing the spectrum of Cthulhu, rich in tholins, with that of Kiladze, an impact crater within East Tombaugh Regio where H_2O is pure and abundant (Cook et al., 2019), shows that around 2 μm they have similar shapes. Therefore, disentangling the contribution to the resulting spectrum of H_2O from CH_4 and negative spectral slope material is not easy.

Figures 20A and 20B show the distribution of areal mass fraction and grain size of the NSS endmember across Sputnik Planitia.

The NSS endmember occurs mainly in units ibm, bct, drt of Al-Idrisi Montes, abm, ibm, dmp and drt of Baret Montes, abm, ibm, dmp, drt and spp of Hillary Montes, pmp and spp of Southwest buffer, and ibm and pmp of Tenzing Montes. The abundance ranges between 14% and 38.5%. In the northern regions of Sputnik Planitia, the NSS endmember accounts for 38.4% in unit tbp and 26.9% in dcp, while in the east, this endmember composes between 20.7% and 33.2% of the sh units in the Colles provinces and the dpp and pmp units.

In the units where the NSS endmember is present, we observe a moderate negative trend of the abundance of this component with the integrated band depths of CH_4 in Range 1 (ρ = -0.34), Range 2 (ρ = -0.48), and Range 4 (ρ = -0.55; Figure 21a). The NSS endmember is not correlated with the CH_4 in Range 3 (ρ = -0.0007), while it has a moderate and slight anti-correlation with

* Some feature names mentioned in this paper are now formalized while others are informal

829 the CH_4 band at 1.48 μm (ρ = -0.35) and the N_2 absorption at 2.15 μm (ρ = -0.28; Figure 21b),
830 respectively.
831 Unit drt in Baret and Al-Idrisi Montes hosts the highest amount of NSS endmember, followed
832 by unit abm in Baret and Zheng He Montes, unit tbp in the Cellular plains, units dmp, drt and lpp
833 in Hillary Montes, and unit dmp in Baret Montes. Unit drt and unit abm of Baret Montes also
834 have very suppressed absorptions in the CH_4 Ranges 1, 2 and 4, the integrated band depth being
835 close to 0.0. The same suppressed absorptions are also observed in Figure 21b for the CH_4
836 absorption at 1.48 μm, and for the N_2 feature.
837 Both Figures 21a and 21b do not show a north-south or east-west trend. Units belonging to
838 provinces in the east and south of Sputnik Planitia share similar NSS endmember percentages,
839 and analogous CH_4 integrated band depth values.
840 In Figure 22, the abundance of the NSS endmember is compared to the CH_4 shift index (top
841 panel), the integrated band depth of H_2O ice (central panel), the areal mass fraction of crystalline
842 H_2O ice (bottom panel).
843 The correlation coefficient of the top panel is equal to -0.36, denoting that a slight dependence
844 between the shift value and the spectra's negative slope exists. In the other two panels, the
845 represented quantities do not show any clear correlation. Indeed, if we do not consider units drt
846 in the middle and bottom panels, the correlation coefficient drops close to 0. The trend in the
847 middle panel of Figure 22 confirms the difficulty to disentangle H_2O from tholins in the
848 spectrum, and the necessity to use a radiative transfer model.
849 Assuming that variations in scattering properties do not yield significant changes in the
850 modeled parameters, we can conclude that tholins are primarily responsible for the suppression
851 of CH_4 absorptions in Ranges 1, 2, and 4 in the units located on the west provinces of Sputnik

* Some feature names mentioned in this paper are now formalized while others are informal

Planitia. For some of these units, like drt in Baret and Al-Idrisi Montes and abm in Baret Montes, tholins are the major contributors of the observed trend of Figure 13a. For the other units in the same area, tholins and H_2O ice both play a role in suppressing CH_4 signatures. Tholins and H_2O ice do not affect the shape and depth of CH_4 absorption in Range 3 and of N_2 feature at 2.15 μm.

Fig. 20: *Maps of variation of NSS endmember areal mass fraction (A) and grain size (B) estimated by the spectral modeling.*

Fig 21: ***(A)*** *Scatter plot showing the correlation between the CH_4 integrated band depth in Ranges 1 (top), 2 (middle), and 4 (bottom) with the NSS endmember areal mass fraction. A moderate negative trend between the abundance of the* ***NSS endmember*** *with the integrated band depths of CH_4 in Range 1, Range 2, and Range 4 is observed.* ***(B)*** *Scatter plot showing the correlation between the CH_4 integrated band depth in Range 3 (top), at 1.48 μm (middle), and the N_2 integrated band depth at 2.15 μm (bottom) with the* ***NSS endmember*** *areal mass fraction. The* ***NSS endmember*** *is not correlated with the CH_4 in Range 3, while it has a moderate and slight anti correlation with the CH_4 band at 1.48 μm and the N_2 absorption at 2.15 μm.*

Fig 22: *Scatter plot showing the correlation between the CH_4 band shift index (top), H_2O integrated band depth (middle), and crystalline H_2O areal mass fraction (bottom) versus the NSS endmember areal mass fraction. The top panel shows a slight dependence between the shift value and the* ***negative spectral slope****, while in the other two panels, the represented quantities do not show any clear correlation.*

In our analysis, we examined several refractory materials that are featureless (i.e. they show no absorption bands) and only display a positive, neutral or negative spectral slope in the wavelength range we have examined (Figure 4). The use of kaolinite, a phyllosilicate, in our models consistently returned better fits to the data than any other material, including Plutonian tholins.

In general, hydrated materials display bands at around 1.4 and 1.9 μm due to OH stretch, with the latter band being the stronger of the two. Because the optical constants for diluted CH_4 in N_2 are highly uncertain in the 1.82-2.11 μm range, we have excluded this band from our work and therefore we cannot fully assess the presence (or absence) of a hydration band around 1.9 μm. The weaker band around 1.4 μm, which is in a spectral window that is analyzed in this work, is blended with several weak CH_4 bands.

Kaolinite also has an identifiable band around 2.3 μm, but like the 1.9 μm region, it is excluded from our analysis due to uncertain optical constants of diluted CH_4 in N_2. Thus, we cannot confirm if kaolinite specifically is present or not, but rather it likely shares spectral properties with what is **observed** – a negative spectral slope.

* Some feature names mentioned in this paper are now formalized while others are informal

883 Tholins produced in Pluto's atmosphere and on Pluto's surface are a likely candidate for the
884 negative spectral slope material on its surface. Tholins, which are typically red at visible
885 wavelengths, can have a slope in the near-infrared spectral region that ranges from positive to
886 negative. The fact that studies of the chemistry of Pluto's atmosphere (e.g. Bertrand & Forget, 2017;
887 Cheng et al., 2017; Gladstone et al., 2016) produce tholins with a negative spectral slope at near-
888 infrared wavelengths supports the idea that the negative spectral slope material present on Pluto is
889 caused by tholins. To date, however, the optical constants for Plutonian tholins are limited, and their
890 use in our analysis returns non-physical solutions.
891 As explained in Section 3.3, we selected four geologic units rich in red material to test the
892 Plutonian tholins introduced by Cruikshank et al. (2016): unit drt in Al-Idrisi, Hillary, and Baret
893 Montes, and sh in Columbia Colles. Figure 23 shows the LEISA average spectra superimposed upon
894 the best fit model obtained by considering Plutonian tholins as a NSS endmember. Table 5 shows
895 compositional details resulting from the modeling.
896 When Plutonian tholin is used as the NSS endmember, we typically find very small grain sizes
897 (Table 5) and the Hapke code reaches the small grain limit for pure Hapke theory (0.8 μm diameter).
898 The code, though, does not jump to the Rayleigh scattering regime (which accounts for particles
899 smaller than 1 micron), likely because that would increase χ^2. We also commonly find that the best fit
900 temperature and dilution are increased, sometimes to the limits of our search space (maximum 60 K
901 and 20% dilution CH_4 in N_2).
902 Specifically comparing models where the NSS endmember is kaolinite or the Plutonian tholin,
903 those models with kaolinite had $\chi 2$ values about a half that of models with Plutonian tholin.
904 These findings lead us to conclude that **a surface component with a** negative spectral slope must
905 be present in the Sputnik Planitia regions we have examined, and which is perhaps uniformly present
906 on Pluto, but our current understanding of Plutonian tholins is not sufficient to match the
907 observations, and so more laboratory-based spectroscopic measurements are required.

* Some feature names mentioned in this paper are now formalized while others are informal

Figure 23: *LEISA spectra, averaged for unit drt in Al-Idrisi, Hillary and Baret montes, and unit sh in Columbia Colles, overlapped by the corresponding Hapke theory-based best fit model. In this case, the modeling made use of the Pluto tholins optical constants, in place of the* ***NSS endmember*** *ones. The spectra are offset for clarity.*

Table 5: Parameters used to model four LEISA spectra with a modified version of the Hapke theory (i.e. Hapke 1993, 2012), by using Pluto tholins.

Province*	T (K)	CH_4 fraction (%)	Component	Unit	Mass fraction	Grain diameter (mm)	Fractional Area	Areal mass fraction (%)
DRT								
Baret Montes	44	11.1	N_2:CH_4	A	1.000	32.1	0.159	**15.9**
			Pluto tholin	B	0.039	0.0008	0.841	**3.3**
			Crystalline H_2O		0.802	0.093		**67.4**
			Amorphous H_2O		0.159	0.003		**13.4**
Hillary Montes	44	0.70	pure CH_4	A	0.001	0.58	0.625	**0.1**
			N_2:CH_4		0.999	1,464.2		**62.4**
			Pluto tholin	B	$2.0*10^{-05}$	0.59	0.375	**0.0**
			Crystalline H_2O		1.000	0.008		**37.5**
Al-Idrisi Montes	49	2.9	N_2:CH_4	A	1.000	18.8	0.192	**19.2**
			Pluto tholin	B	0.025	$8.0*10^{-4}$	0.808	**2.1**
			Crystalline H_2O		0.384	0.072		**31.0**
			Amorphous H_2O		0.590	0.010		**47.7**
SH								
Columbia Colles	60	19.1	pure CH_4	A	0.002	0.13	0.573	**0.1**
			N_2:CH_4		0.028	5.96		**1.6**
			β-N_2		0.970	634.9		**55.6**
			Pluto tholin	B	0.008	$8.0*10^{-4}$	0.427	**0.4**
			Crystalline H_2O		0.992	0.038		**42.3**

5. Correlation of spectral results and observed geology

5.1 Blocky mountains and inter-block material.

The chaotic, angular, blocky mountains (unit abm), form a discontinuous buffer between Sputnik Planitia and the uplands to the west. The mountain blocks typically reach >10 km in diameter and are mostly contained within the ranges of Al-Idrisi, Baret, Hillary, Tenzing, and Zheng He Montes. Isolated mountain blocks are also seen within the dcp unit of the Cellular

* Some feature names mentioned in this paper are now formalized while others are informal

921 plains, the largest being Coleda de Dados Colles. The inter-block material (unit ibm) consists of
922 chaotically oriented, close-packed blocks, typically reaching a few to several km across, that
923 occur interstitially to and can also embay the abm unit. The blocks are similar to, but smaller
924 than, the blocks forming the abm unit. The finer texture of unit ibm compared to abm may
925 indicate breaking up of mountain blocks into smaller fragments and/or size filtering thereafter
926 (White et al., 2017; O'Hara & Dombard, 2020). The mountain blocks that form these units are
927 randomly oriented and have been hypothesized to consist of fragments of the H_2O ice crust that
928 have been detached by tectonism and intruded, transported, and rotated by glacial N_2 ice (White
929 et al., 2017).
930 Crystalline H_2O ice is indeed present to **various** degrees in both units, with areal mass
931 fractions ranging between 9.3% and 47.1% (Figure 17a). The abundance of crystalline H_2O ice
932 within unit abm is broadly constant between Al-Idrisi, Baret, and Hillary Montes (varying
933 between 35.4% and 41.9%), although there is a dip to 25.1% at Zheng-He Montes. To the south
934 of Hillary Montes, there is a substantial decrease in the abundance from 18.3% at the Southwest
935 buffer to 9.3% at Tenzing Montes. The abundance of NSS endmember within abm reaches a
936 maximum in the low northern latitudes: Al-Idrisi Montes shows none, Zheng He, Baret and
937 Hillary Montes show 41.6%, 36.7%, and 27.8% respectively, and the Southwest buffer and
938 Tenzing Montes show none. The NSS endmember maximum in the central Montes correlates to
939 the occurrence of dark tholins coating Zheng He, Baret and Hillary Montes, which unlike Al-
940 Idrisi and Tenzing Montes are co-latitudinal with the equatorial maculae that extend in a
941 discontinuous belt around Pluto. The maculae are interpreted to represent tholins that have
942 formed via ultraviolet irradiation of CH_4 in Pluto's atmosphere, settled out onto the surface, and
943 accumulated to form a superficial, but contiguous, layer (Moore et al., 2016; Grundy et al.,

* Some feature names mentioned in this paper are now formalized while others are informal

944 2018). This process occurs across Pluto's entire surface, but the low latitude uplands within the
945 permanent diurnal zone are the only location where climatic conditions are mild enough on
946 obliquity timescales such that the layer is not dissipated by regular volatile mobilization (Binzel
947 et al., 2017; Earle et al., 2017, 2018). Grundy et al. (2018) estimated that unperturbed tholin
948 accumulation would coat the surface to a thickness of ~3.5 m over 1 Gyr, a result supported by
949 Johnson et al. (2020). The elevated abundance of NSS endmember within the abm unit of the
950 central Sputnik mountain ranges, in combination with the observation that they are coated by a
951 dark material whereas peaks in the northern and southern ranges are not, therefore indicates that
952 these dislodged crustal blocks are sufficiently stable in their grounded state, surrounded by N_2
953 ice of Sputnik Planitia, to accumulate tholins to the extent that they form a contiguous layer over
954 millions of years. As noted in Section 4, it is difficult to disentangle the effects of H_2O ice and
955 negative spectral slope material at around 2 μm, and previous works (e.g. Cruikshank et al.,
956 2015, Schmitt et al., 2017, Protopapa et al., 2017) have accordingly identified a correlation
957 between the abundance of H_2O ice and tholins, which may form part of the explanation for the
958 generally high abundance of H_2O ice within the central Sputnik mountain ranges (especially
959 Baret Montes).

960 For both the abm and ibm units, there is a pronounced minimum in the abundance of volatile
961 ices for the central Sputnik mountain ranges. The areal mass fraction of N_2:CH_4 and β-N_2 in abm
962 is 64.6% at Al-Idrisi, which dips to 33.3% and 21.4% in Zheng He and Baret Montes
963 respectively, before increasing to 34.7% in Hillary Montes, 81.3% in the Southwest buffer, and
964 89.3% at Tenzing Montes. We interpret this pattern to be a consequence of the extensive tholin
965 coverage in the central ranges, and it is notable that it is anti-correlated to the NSS endmember,
966 the abundance of which reaches a maximum in these ranges. For those ranges not coated with

* Some feature names mentioned in this paper are now formalized while others are informal

967 tholins, the elevated abundance of volatiles in the southern mountain ranges (81.3-89.3%)
968 relative to those in the north (64.6%) is interpreted to be a consequence of the highly variable
969 insolation and climate zones across the latitudinal extent of Sputnik Planitia that derive from
970 Pluto's high obliquity (presently 123°) (Hamilton et al., 2016; Binzel et al., 2017; Earle et al.,
971 2017). Modeling of the N_2 cycles on Pluto over seasonal and astronomical timescales by
972 Bertrand et al. (2018) shows that over one obliquity cycle in Pluto's current orbital configuration,
973 the latitudes of Sputnik Planitia (25°S - 30°N) are dominated by N_2 condensation, entirely
974 incorporating Tenzing Montes between 9°S and 22°S, whereas the northern regions between
975 30°N and 50°N are dominated by N_2 sublimation, mostly incorporating Al-Idrisi Montes
976 between (25°N - 42°N)**.** This effect may explain the paucity of interstitial N_2 ice separating the
977 mountain blocks of northern ranges such as Al-Idrisi (Fig. 25a), relative to the blocks of Tenzing
978 Montes, the flanks of which appear to be inundated by N_2 ice plains that are elevated by as much
979 as a kilometer above those of Sputnik Planitia (Fig. 25b), implying voluminous N_2 ice
980 accumulation amongst the blocks here. The extensive coating of the southern mountains by such
981 condensed volatiles likely explains the lower detections of H_2O ice here relative to the northern
982 mountains, where the H_2O ice is more exposed. Volatile condensation is especially enhanced in
983 southern Sputnik at present as these regions are entering winter, whereas the northern regions are
984 entering summer.

985 A similar effect may be seen in the areal mass fraction of pure CH_4 ice in unit abm, which
986 while forming less than a few percent of this unit, shows a general increase from north to south:
987 it is absent at Al-Idrisi, Zheng He, Baret, and Hillary Montes, increases to 0.4% at the Southwest
988 buffer, and to 1.4% at Tenzing Montes (the highest areal mass fraction for any unit in any
989 province in the mapping area). For the latter range, N_2 absorption is especially suppressed (Fig.

* Some feature names mentioned in this paper are now formalized while others are informal

990 10). N_2 and CH_4 will both deposit at low elevations, but the higher abundance of N_2 relative to
991 CH_4 in Pluto's atmosphere, in combination with the warmer atmosphere at high elevations
992 inhibiting N_2 precipitation (Moore et al., 2018; Bertrand et al., 2020a), means that deposition of
993 N_2 dominates at lower elevations, whereas CH_4 is mostly deposited at high elevation. Therefore,
994 both the very high elevation of Tenzing Montes (rising to >5 km above mean radius) and their
995 equatorial latitude make them a natural setting for the precipitation of CH_4 ice under Pluto's
996 present obliquity and seasonal conditions. The volatile transport modeling of Bertrand et al.
997 (2019) found that at higher latitudes, CH_4 deposits are only stable on a seasonal timescale for
998 Pluto's current orbital configuration, but at lower latitudes, such deposits at high elevation would
999 grow thicker and potentially subsist across multiple Pluto years, as in the case of the bright CH_4
1000 deposits that are seen to coat the summits of Pigafetta and Elcano Montes within Cthulhu
1001 Macula, the crests of which rise to almost 4 km above mean radius (Bertrand et al., 2020a). The
1002 CH_4 at Tenzing Montes is not **characterized by** a bright coating **unlike** the summits of the co-
1003 latitudinal Pigafetta and Elcano Montes, which may be due to (i) the overall low abundance of
1004 pure CH_4 ice here (1.4%), (ii) the lower albedo contrast between CH_4 frost and H_2O ice as
1005 compared to CH_4 frost and the dark blanket of tholins, and (iii) perhaps also the fact that Tenzing
1006 Montes were seen at a very high solar incidence angle (~77°) during the New Horizons flyby,
1007 which minimizes the visibility of the albedo contrast between the CH_4 frost and H_2O ice.
1008
1009 *5.2 Bright chaotic terrain*
1010 The bright, chaotic terrain unit (bct) is confined to a single region to the north of Al-Idrisi
1011 Montes. It consists of high albedo plains interspersed with darker blocks reaching several km
1012 across. The unit is crossed by east-west oriented troughs and scarps, and is at a slightly lower

* Some feature names mentioned in this paper are now formalized while others are informal

elevation (by ~0.5 km) than unit ibm to the south, making it amongst the lowest elevation regions of anywhere in Sputnik Planitia and its borders (reaching 3 km below mean radius). The fact that the unit displays a geomorphology that is more characteristic of the fluted, valleyed uplands to the north **led** White et al. (2017) to hypothesize that it may represent an early stage in the formation of the chaotic, angular, blocky mountains, whereby tectonically weakened H_2O ice crust is in the process of fragmenting as it is being infiltrated by glacial N_2 ice that has overflowed from Sputnik Planitia, or condensed directly onto it from the atmosphere in large quantities on account of the terrain's very low elevation. This hypothesis is supported by the composition of bct, very similar to the ibm unit, which is interpreted to represent small H_2O ice crustal blocks that have been dislodged and coated by the glacial N_2 ice. β- N_2 is the most abundant component in bct and ibm (54.8% and 41.2% respectively), followed by crystalline H_2O ice (25.5 % and 34.9%), the NSS endmember (14% and 21.3%), and N_2:CH_4 (5.7% and 2.5%). The abundance of N_2 in this area is also confirmed by LEISA spectra: Figures 6 and 10 show that unit bct has the highest CH_4 band shift parameter and deepest N_2 absorption band of any unit.

5.3 Dark, Ridged Terrain

The dark, ridged terrain (unit drt) consists of low albedo, subparallel ridges with crest-to-crest spacing of several hundred meters to a few km, which mainly separate Baret and Al-Idrisi Montes from the uplands of Viking Terra to the west, although a smaller occurrence is also seen separating Hillary Montes from the dark-pitted, marginal plains. The ridges tend to align parallel to the edge of Sputnik Planitia. Unit drt displays the highest areal mass fraction of the NSS endmember of any unit (38.5%-53.4%), followed by N_2:CH_4 (21.5%-38.7%), and H_2O ice

* Some feature names mentioned in this paper are now formalized while others are informal

(18.1%-28.5%). The high abundance of NSS endmember reflects the fact that this unit displays the most contiguous and complete coverage by tholins of any unit. The ridges have been variously interpreted to be compressional in origin, whereby they form due to buoyant, mobile H_2O ice blocks being pushed towards the uplands by convective motions in Sputnik Planitia, with a weaker, darker, overlying layer folding in response to the compressive forces (White et al., 2017; Ahrens & Chevrier, 2019), or depositional, whereby they are recessional moraines of dark tholins deposited as the N_2 ice glaciers responsible for entraining and translating the H_2O ice mountains retreated (Howard et al., 2017). White et al. (2017) hypothesized that this dark material represents tholins like those coating Cthulhu Macula and Baret, Zheng He, and Hillary Montes, while Ahrens and Chevrier (2019) interpreted the ridges to be formed from a thin layer of CH_4-H_2O ice overlain on a H_2O ice-based glacier. Our spectral analysis and modeling does not suggest that the dark material is especially enriched in CH_4, with between 0.5% and 0.8% CH_4 being diluted in the N_2:CH_4 (Fig. 8A) that forms between 21.5% and 38.7% of the unit by areal mass fraction. The prevalence of the NSS endmember that characterizes this unit, and its very low albedo, **leads** us to conclude that the deformed layer is more likely composed of tholins rather than a CH_4-H_2O ice mixture.

There is always a sharp and well-defined boundary between unit drt and adjoining units – the dark tholins are always tightly confined to within the unit's boundaries and do not spread beyond its borders, implying that whatever process has created this unit, it has acted to densely concentrate the tholins within the unit. In addition, whereas the drt units of Baret and Hillary Montes are mostly located within the equatorial, permanent diurnal zone (13°N to 13°S) that harbors the maculae and the tholin-covered mountain ranges, that of Al-Idrisi Montes extends to higher latitudes (20°N to 30°N), suggesting that accumulation directly via settling from the

* Some feature names mentioned in this paper are now formalized while others are informal

atmosphere alone cannot explain the density of tholins here, as it can for the tholin coverage on the mountain ranges. Since the low albedo N_2 ice plains of northern Sputnik Planitia (encompassing units dcp and tbp, see section 5.5) are interpreted to have high levels of tholins entrained within them, the same compressive forces that White et al. (2017) and Ahrens and Chevrier (2019) hypothesized formed the ridges may have also concentrated tholins within N_2 ice separating the mountain blocks, dredged them to the surface, and formed them into the sub-parallel ridges. We further discuss unit drt in section 5.4, in which we argue that Columbia Colles, mapped by White et al. (2017) as scattered hills, displays geomorphological and spectral characteristics associated with unit drt.

5.4 Scattered hills

The scattered hills form a unit (sh) in eastern Sputnik Planitia consisting of km-sized hills with up to 500 m topographic relief that have been carried by N_2 ice valley glaciers flowing from East Tombaugh Regio into the Cellular plains of Sputnik Planitia (White et al., 2017). In addition, there are Challenger and Columbia Colles, larger conglomerations of such hills that form roughly rectangular masses measuring several tens of km across, and which have been interpreted to be grounded in shallow N_2 ice here at the edge of Sputnik basin (White et al., 2017). Given that these hills appear to be subject to the motions of N_2 ice (both glacial and convective) in this region of Sputnik Planitia, White et al. (2017) and Howard et al. (2017) hypothesized that they represent chunks of the pitted uplands that have been broken off through glacial erosion and transported in the N_2 ice. Geologic mapping of the pitted uplands and the CH_4 ice bladed terrain of Tartarus Dorsa to the east indicates that the pitted uplands are likely a lower-elevation extension of the bladed terrain that is experiencing deposition of volatile ices

* Some feature names mentioned in this paper are now formalized while others are informal

1082 that have sublimated from Sputnik Planitia (Moore et al., 2018). This would imply that the pitted
1083 uplands, and the scattered hills derived from them, are predominantly composed of CH_4 ice.
1084 Our spectral modeling of the discrete ranges of hills that form unit sh shows a relatively
1085 consistent pattern: hills in the South-East pitted plains and Astrid, Challenger, and Soyuz Colles
1086 show a composition that is predominantly β-N_2 (64.4%-79%), followed by the NSS endmember
1087 (19.7%-32.4%), with a small areal mass fraction of N_2:CH_4 (1.3%-3.6%). These hills are located
1088 within the portion of Sputnik Planitia that is interpreted to be experiencing net N_2 ice deposition
1089 under Pluto's current climatic and obliquity conditions (White et al., 2017, Bertrand et al., 2018),
1090 and the dominance of β- N_2 in the spectra reflects this. In 315 m/pixel imaging of the hills, they
1091 show a similarly high albedo **with respect** to the surrounding N_2 ice plains, and their surface
1092 relief appears smoothened, indicating that they have accumulated a contiguous coating of N_2 ice
1093 (Fig. 26a). This coating is thick enough to obscure the spectral signal from the material
1094 composing the hills themselves, so we cannot confirm spectroscopically whether the hills are
1095 composed of H_2O or CH_4 ice (both of which are less dense than N_2 ice, allowing the hills to
1096 float, and both of which are rigid enough at Pluto conditions to support the topographic relief
1097 exhibited by the hills).
1098 A notable exception to the trend is Columbia Colles, which displays a composition that is
1099 more similar to the dark, ridged terrain (unit drt) than the other scattered hills (cf. Fig. 24N to the
1100 drt units in Figs. 24A, B, and F). Like the other scattered hills, Columbia Colles displays
1101 substantial β-N_2 (45.5%) and NSS endmember (21.7%), with a small areal mass fraction of
1102 N_2:CH_4 (0.05%), but also displays a large areal mass fraction of crystalline H_2O (32.8%). The
1103 H_2O ice may be attributed to the fact that Columbia Colles are the only portion of the unit sh to
1104 display a consistent covering by dark red tholins, the spectral signature of which, as noted earlier,

* Some feature names mentioned in this paper are now formalized while others are informal

1105 is difficult to distinguish from that of H_2O ice. Unit drt also shows significant crystalline H_2O
1106 (18.1%-28.5%) and NSS endmember (38.5%-53.4%), but with N_2:CH_4 (21.5%-38.7%) in place
1107 of β-N_2, which is absent. Portions of Columbia Colles display a quite well-developed ridged
1108 fabric, with ridge crests separated by 1-2 km (very similar to the separation of the ridge crests of
1109 unit drt, Figs. 26b and 26c). White et al. (2017) mapped Columbia Colles as part of unit sh on
1110 account of its proximity to the other scattered hills and close spatial relationship to Challenger
1111 Colles (a discontinuous "bridge" of hills 60 km long joins the two conglomerations). The
1112 distinct dark red color of Columbia Colles, its more explicitly ridged texture compared to
1113 anything seen elsewhere within unit sh, and the fact that Columbia Colles is the only portion of
1114 unit sh that contacts the surrounding uplands (as do the occurrences of unit drt in Baret and Al-
1115 Idrisi Montes, and possibly also that in Hillary Montes if the dark-pitted, marginal plains that
1116 bound it represent uplands terrain of Cthulhu Macula covered by thin N_2 ice), however, are
1117 characteristics that are more diagnostic of unit drt. Unit drt is interpreted to represent an
1118 accumulation of dark tholins superposed on lighter-toned H_2O ice blocks that have eroded from
1119 Pluto's ancient H_2O ice crust along the western margin of Sputnik Planitia (section 5.3), whereas
1120 Columbia Colles, and the rest of the scattered hills, are interpreted to consist of blocks of CH_4 ice
1121 that were eroded more recently from the pitted uplands of East Tombaugh Regio. Therefore,
1122 while we hypothesize that the same processes have probably caused the concentration of dark
1123 surface material at the western dark ridged terrain as well as Columbia Colles, and its
1124 arrangement into subparallel ridges, the material forming Columbia Colles is still distinct
1125 stratigraphically and compositionally from that forming the western dark ridged terrain, and so
1126 mapping Columbia Colles as unit sh, rather than drt, remains justified. The processes forming the
1127 ridges are not known for certain, but compression of the underlying blocky material and glacial

* Some feature names mentioned in this paper are now formalized while others are informal

recession have both been invoked (Howard et al., 2017; White et al., 2017; Ahrens and Chevrier, 2019).

5.5 Cellular plains

The Cellular plains of Sputnik Planitia represent the portion of the N_2 ice sheet that is experiencing solid-state convection from thermal input within or below the glacier (Stern et al., 2015; Moore et al., 2016; McKinnon et al., 2016; Trowbridge et al., 2016). The plains dominate the central and northern portions of Sputnik Planitia, i.e. the part of Sputnik Planitia corresponding to the Sputnik basin itself, where the N_2 ice is sufficiently thick (>1 km) to support convection (McKinnon et al., 2016). The cells tend to be ovoid in planform, are defined by a reticulate network of troughs with central ridges, and exhibit pitting on a scale of hundreds of meters to a few km (Moore et al., 2016; White et al., 2017). The timescale of surface renewal via convection has been estimated to be ~420,000 to ~890,000 years (McKinnon et al., 2016; Trowbridge et al., 2016; Buhler & Ingersoll, 2018). White et al. (2017) divided the Cellular plains into three units based primarily on albedo. The bright, Cellular plains (unit bcp) occupy the central portion of Sputnik Planitia, extending to ~30°N. They display a normal reflectance of 0.78 to 0.86 (Buratti et al., 2017) and are interpreted to be the region of Cellular plains that are presently experiencing net deposition of fresh, bright N_2 frost from the northern regions of Sputnik Planitia (Protopapa et al. 2017; Bertrand et al., 2018, 2020b). The dark, Cellular plains (unit dcp, with a normal reflectance of ~0.69), and dark, trough-bounding plains (unit tbp, with a normal reflectance of ~0.52-0.60) occur in the northern and western portions of Sputnik Planitia, and are interpreted to be presently experiencing net sublimation (Protopapa et al. 2017; Bertrand

* Some feature names mentioned in this paper are now formalized while others are informal

et al., 2018, 2020b). With the exception of Alcyonia Lacus in Al-Idrisi Montes, all three units of the Cellular plains are confined to the Cellular plains in this study.

Unsurprisingly, the most abundant component of all three units is N_2 ice, the CH_4 fraction diluted in N_2 always being below 1%. This observation is also confirmed by the high values of the CH_4 band shift index, and by the depth of N_2 absorption band. Unit bcp is dominated by N_2:CH_4, which accounts for 99.9% of its areal mass fraction, corroborating the interpretation that the high albedo of unit bcp is due to current deposition of fresh N_2 frost on its surface White et al. (2017). Units dcp and tbp are instead dominated by β-N_2 ice: dcp shows 68.2% β-N_2 and 4.9% N_2:CH_4, whereas tbp shows 53.9% β-N_2 and 7.6% N_2:CH_4. The remainders of these units are mainly occupied by NSS endmember: 26.9% for dcp and 38.4% for tbp. Based on the results of Protopapa et al. (2017) and Schmitt et al. (2017), White et al. (2017) interpreted unit dcp to be representative of the material filling the Sputnik basin, specifically N_2 ice that **is associated with** a relatively high concentration of tholins that first settled onto the surface by katabatic and condensation flows (Bertrand et al., 2020b) and then became entrained within the ice by convective motion across the history of the existence of Sputnik Planitia (White et al., 2017). This N_2/tholin mixture is only exposed in the north and west where the net sublimation of the N_2 ice means that it is not blanketed by a fresh layer of bright N_2 frost as seen in the rest of Sputnik Planitia, including unit bcp (Bertrand et al., 2018, 2020b). In the case of the lower albedo unit tbp, confined to the northern edge of Sputnik Planitia, White et al. (2017) interpreted this to be where tholins in the N_2 ice had become especially concentrated at cell boundaries through a combination of convective motion of the ice and the very high sublimation rates encountered here (higher than anywhere else in Sputnik Planitia across an obliquity cycle). In accordance with this hypothesis, we find that the proportions of NSS endmember within these three Cellular

* Some feature names mentioned in this paper are now formalized while others are informal

1173 plains units correlate to their albedos, and indicate a progressively increasing tholin content
1174 within darker plains.
1175 Alcyonia Lacus is an irregular, 30 km long by 10 km wide expanse of N_2 ice plains that is
1176 surrounded by units abm and ibm of Al-Idrisi Montes, and which was mapped as dcp by White et
1177 al. (2017) (Fig. 27a). While the plains do show the same albedo as unit dcp within Sputnik
1178 Planitia, they are separated from the Cellular plains by the mountain range, so cannot strictly be
1179 described as "cellular". The absence of pits indicates that it is being resurfaced by some means
1180 other than sublimation, and/or that its rheology is unable to support pit topography. Its relatively
1181 smooth boundaries, whereby the surrounding mountains and hills do not intrude into its interior,
1182 indicate that this feature may have actively modified its boundaries. It has variously been
1183 interpreted as once being a "pond" of liquid N_2 maintained during an era of high atmospheric
1184 pressure, and which has since frozen (Stern et al., 2017), or an active glacial feature in which
1185 flow of the N_2 ice closes any sublimation pits and shepherds blocky H_2O ice material to its edges
1186 (White et al., 2017). Spectral modeling shows that its composition is broadly similar to that of
1187 the dcp unit proper within Sputnik Planitia, exhibiting 53.9% β-N_2, 20.7% NSS endmember, and
1188 1.9% N_2:CH_4, but with an additional H_2O ice component, comprising 23.6%. Sub-resolution
1189 H_2O ice fragments floating within the N_2 ice of the lacus may cause this. The presence of the
1190 NSS endmember suggests that, like unit dcp within the Cellular plains, Alcyonia Lacus also
1191 consists of "mature" N_2 ice that has entrained a high concentration of tholins within its volume
1192 over the course of its existence, but given its geographic isolation from Sputnik Planitia (the two
1193 are separated by 65 km), it most likely formed independently from Sputnik Planitia and
1194 separately acquired its tholins. White et al. (2017) hypothesized that the lacus may be situated at
1195 a localized zone of high geothermal flux that is mobilizing the N_2 ice and causing any blocky

* Some feature names mentioned in this paper are now formalized while others are informal

H_2O fragments within the zone of mobilization to drift to its edges, and if the lacus is long-lived, then it is possible that such continual mobilization has also allowed gradual entrainment of tholins within the N_2 ice to levels comparable to that seen within unit dcp of the Cellular plains.

5.6 Non-Cellular plains

The non-Cellular plains of Sputnik Planitia are those that are interpreted to not be currently experiencing solid-state convection. These plains dominate the southern and eastern regions of Sputnik Planitia, but there are also small occurrences seen interstitially to mountain and Cellular plains units at the western and northern boundaries. As with the Cellular plains, these plains exhibit pitted textures, but the pits can reach much larger diameters (typically >1 km). The transition from cellular to non-Cellular plains is interpreted to reflect thinning of the volatile ice layer, and perhaps also declining heat flow (McKinnon et al., 2016). The non-Cellular plains are not convecting, but they have nevertheless very recently resurfaced via glacial flow of the N_2 ice from which they are formed, possibly on a timescale as short as tens of thousands of years (Wei et al., 2018). The non-Cellular plains universally show a high normal reflectance (0.78 to 0.86), like that of the bright Cellular plains. This is true even for the small patches of non-Cellular plains located at the northern and western edges of Sputnik Planitia (the North pitted plains and West pitted plains provinces), which are situated within the portion of Sputnik Planitia that is currently experiencing net sublimation and which abut the darker plains units (dcp and tbp) (White et al., 2017; Bertrand et al., 2018, 2020b).

β-N_2 and N_2:CH_4 are the most abundant components of the non-Cellular plains: in the southern region of Sputnik Planitia, the deeply pitted plains (unit dpp), lightly pitted plains (unit lpp), sparsely pitted plains (unit spp), patchy, pitted, marginal plains (unit pmp), and dark-pitted

* Some feature names mentioned in this paper are now formalized while others are informal

marginal plains (unit dmp) display between 59.2% and 100% N_2:CH_4 and β-N_2 by areal mass fraction. The proportion of N_2:CH_4 and β-N_2 versus NSS endmember within these plains appears to correlate to the extent to which the plains display deep pits. The plains units exhibiting the largest pits (typically reaching ~1 km in diameter, but which can reach several km) are the deeply pitted plains, which are primarily concentrated in the southernmost region of Sputnik Planitia where they dominate the South pitted plains province, and the dark-pitted, marginal plains, which form a buffer between the mountain ranges of Hillary and Baret Montes and the uplands of Cthulhu Macula. The pits in both of these units tend to cluster together in tightly packed swarms that form curved, wavelike patterns (White et al., 2017), and where they are large enough for their floors to be resolved and not obscured by shadows cast by the pit walls, the floors invariably display a low albedo (<0.17 normal reflectance, Buratti et al., 2017). This low albedo material has been interpreted to be tholins covering the pit floors (White et al., 2017), which in the case of dpp may be tholins entrained within the N_2 ice that have been released via sublimation to build up on the floors of the pits as a lag, and in the case of dmp may be tholins of Cthulhu Macula, whereby the N_2 ice covering the macula is thin enough for the pits to extend all the way through the ice, exposing the tholins of Cthulhu Macula underneath. Our models show that both units exhibit NSS endmember: 20.7% for dpp in the South pitted plains, and 38.9% to 61.4% for dmp in Baret and Hillary Montes respectively. The high abundance of NSS endmember in the latter may be a consequence of the lower solar incidence angle of the imaging covering unit dmp relative to dpp, meaning that shorter shadows are cast by the pit walls across pit floors in dmp, and so higher proportions of the pit floors are visible. Pits within dpp in southern Sputnik Planitia are mostly small enough for shadows to cast across their entire floors.

* Some feature names mentioned in this paper are now formalized while others are informal

In contrast to these plains units that display large and deep pits, the lightly pitted plains and sparsely pitted plains were interpreted by White et al. (2017) to be experiencing only superficial sublimation of N_2 ice, and are instead undergoing mantling by ongoing deposition of N_2 frost, as well as glacial creep of the N_2 ice that is infilling any large pits that do exist. Any sublimation occurring within these plains is therefore insufficient to counter these processes and to create large pits that expose tholins entrained within the N_2 ice, meaning that neither of these units is interpreted to display non-volatile components (i.e. NSS endmember) in their composition. Accordingly, both of these units are dominated by N_2:CH_4 and β-N_2 in the South and East pitted plains (>99% by areal mass fraction), with no NSS endmember observed.

The patchy, pitted marginal plains (unit pmp) are interpreted to represent relatively thin N_2 ice (probably no more than a few hundred meters) that has condensed on rugged, low-lying uplands terrain bordering Sputnik Planitia, explaining why this unit shows a hummocky texture on a scale of several km, whereas the other plains units of Sputnik Planitia are flat. Unit pmp borders the plains of southern Sputnik Planitia, which we interpret to be a geologic consequence of the preferential deposition of volatile ices that is presently occurring within this equatorial, permanently diurnal zone (Bertrand et al., 2018), a phenomenon that is also manifested compositionally by the deeper N_2 band depth in N_2 ice plains at southerly latitudes (Fig. 10). As described in section 5.1, it is for this same reason that we interpret unit abm of Tenzing Montes, which is embayed by elevated N_2 ice plains of unit pmp, to display a high areal mass fraction of N_2:CH_4 compared to the northern mountain ranges. The elevated N_2 ice plains of unit pmp that cover the southeast margin of Sputnik Planitia (Fig. 27b) show some geomorphological similarities to the elevated plains that separate the blocks of Tenzing Montes, including scarps leading from unit pmp down to Sputnik Planitia. Unit pmp shows a similarly dense concentration

* Some feature names mentioned in this paper are now formalized while others are informal

of pits to units dpp and dmp, although the pits of pmp show a smaller size range, never reaching >1 km in diameter. The presence of NSS endmember within unit pmp (areal mass fractions range between 20.8% and 33.2%), however, indicates that its pits do display tholins on their floors that are detectable by LEISA.

The non-Cellular plains at the eastern and southern boundaries of Sputnik Planitia are dominated by β-N_2 ice, with typically only a few percent of N_2:CH_4. But of this N_2:CH_4, Figure 8a shows that the percentage of CH_4 diluted in N_2 is generally high (>4%), whereas it is low for the rest of the plains of Sputnik Planitia (generally <2%). For the southern plains (unit dpp in South pitted plains), the elevated CH_4 content may be interpreted as a manifestation of the general increase in volatile abundance that is seen towards the southern end of Sputnik Planitia, whereby the low insolation that is presently encountered here is conducive to deposition of both CH_4 and N_2 in low-lying areas (deposition of N_2 at low elevation tends to dominate at more northerly, and more insolated, latitudes). Yet the elevated CH_4 content that is seen along Sputnik Planitia's eastern boundary may instead be an indication of CH_4-rich material being transported from the pitted uplands of East Tombaugh Regio by the N_2 ice glaciers that lead from there into Sputnik Planitia. As noted in section 5.4, the pitted uplands likely represent a lower-elevation extension of the bladed terrain, and so their composition is likely CH_4-based (Moore et al., 2018), and the scattered hills (unit sh) have accordingly been interpreted as km-sized blocks of such material that have been transported into Sputnik Planitia (albeit which are coated by freshly-deposited N_2 ice). Yet given that these eastern non-Cellular plains incorporate the active glaciers leading from the uplands, their elevated CH_4 content may be an indication of recently eroded, sub-resolution CH_4-rich material that is being carried on the surface of the glaciers – the lateral moraine trails that have been identified at these glaciers (White et al., 2017, Howard et al.,

* Some feature names mentioned in this paper are now formalized while others are informal

2017) likely represent such sub-resolution material (Fig. 27c). As this material is transported farther to the west, into the interior of Sputnik Planitia, it becomes dissipated, lowering its concentration within the N_2 ice, and it becomes coated by freshly deposited N_2 ice (as has happened to the large scattered hills), resulting in low CH_4 percentages here.

While the non-Cellular plains are concentrated within southern and eastern Sputnik Planitia, units dpp and spp also form small expanses at its western and northern edges (the North and West pitted plains provinces), surrounded by the mountains and Cellular plains. Units dpp and spp within these provinces display a high albedo that is akin to the bright plains of central and southern Sputnik Planitia, and which contrasts with the darker plains of the surrounding Cellular plains (Fig. 27d). That the north and west pitted plains provinces are located within the portion of Sputnik Planitia that is presently experiencing net sublimation of N_2 ice from the surface, and yet still present a high albedo, implies two possible scenarios: (i) the plains may be experiencing net sublimation like the surrounding dark Cellular plains, with the exception that the body of the N_2 ice forming them does not contain a high concentration of tholins that would be exposed at the surface by the sublimation, or (ii) the plains are in fact localized zones of net deposition of N_2 ice rather than sublimation, causing them to be coated by a fresh, bright layer of N_2 frost in the same manner as the plains in the south and east of Sputnik Planitia. These bright northern and western plains differ in composition from their southeastern counterparts: they display units dpp and spp and are composed almost entirely of N_2:CH_4 (>99%), in contrast to the β-N_2 and NSS endmember that form unit dpp in the south, and the β-N_2 and N_2:CH_4 that form unit spp in the south (Fig. 24). The most notable compositional difference is the absence of NSS endmember from unit dpp in the northern and western plains. This suggests that tholins are not covering pit floors here, in contrast to pits in unit dpp in the southern and eastern plains, and indicates that

* Some feature names mentioned in this paper are now formalized while others are informal

tholins are not entrained within the N_2 ice of unit dpp in the north and west. Sublimation of the N_2 ice to form the pits is not exhuming any entrained tholins, meaning that none can build up as a lag on the pit floors. If these northern and western plains are experiencing net sublimation, like the darker, cellular plains surrounding them, then the absence of entrained tholins means that the albedo of the plains will remain high regardless of how much N_2 ice sublimates from the surface. In fact, the presence of localized plains that consistently display a high albedo, and which are therefore consistently cooler than the surrounding darker plains, may actually act to partially offset the predominant sublimation that occurs within this part of Sputnik Planitia, and allow them to retain more of the bright N_2 ice that does deposit on them, in what would essentially be a runaway albedo effect (see point 3 in section 5.7).

This does require, however, that the plains are bright to begin with, which is related to the question of how bright, non-Cellular plains were established in these marginal areas of Sputnik Planitia. They evidently represent portions of the plains at the margins of Sputnik Planitia where the N_2 ice is insufficiently thick to support convection, and within which entrained tholins are absent, in contrast to the dark, adjacent Cellular plains. This observation seems to imply that convection within the Cellular plains is an efficient process for entraining tholins and ensuring that they remain trapped within the convection cells and cannot migrate to adjacent N_2 ice that is not convecting. The fact that dark pit floors are seen in pitted plains of the southern non-Cellular plains suggests that glacial flow of N_2 ice from the center of Sputnik Planitia to its southern regions may play a role in transferring tholin-entrained N_2 ice of the convective cells outside of the convective regime. There is evidence for this in the form of elongated, "extinct" cells extending from the southern boundary of the bright Cellular plains that are defined by chains of joined, dark-floored pits that describe polygonal outlines (Fig. 27e), and which White et al.

* Some feature names mentioned in this paper are now formalized while others are informal

(2017) interpreted to be formerly active convection cells that were moved southwards and their planforms distorted by lateral flow of the ice in this region of Sputnik Planitia. In the case of the bright, non-Cellular plains of the North and West pitted plains, however, it may be that convective motion in the adjacent Cellular plains acts to effectively segregate any tholins entrained within the non-Cellular plains and trap them in the convection cells, thereby brightening the non-Cellular plains and initiating the runaway albedo effect whereby sublimation of N_2 ice remains dominant in the dark Cellular plains, but becomes less effective relative to deposition of N_2 ice in the bright, non-Cellular plains.

5.7 Possible processes responsible for the observed diversity of ice mixtures in Sputnik Planitia

The diversity of ice mixtures and N_2 or CH_4 enrichment at the surface of the plains of Sputnik Planitia may in part be a consequence of various phenomena that would not manifest in geomorphology that is resolvable by New Horizons imaging. These include: (1) Differences in ice thickness (related to different bedrock topography and glacial flow), which would impact deep ice convection and entrainment of tholins, as well as the subsurface heat flow. Within the convective cells, the subsurface heat flow would be larger at the centers than at the edges of the cells. (2) Eolian processes disrupting the surface ice (changes in albedo, composition, grain size, etc.) such as (a) warming by the atmospheric downward sensible flux, (b) mechanical erosion, and (c) atmospheric transport, surface accumulation of haze particles or dark materials and subsequent darkening of the ice (or brightening if ice grains are transported too). Bertrand et al. (2020b) investigated these processes and showed that the former and the latter could significantly impact the surface ice and the volatile sublimation-condensation rates and therefore

* Some feature names mentioned in this paper are now formalized while others are informal

1356 the surface composition. (3) Albedo and composition positive feedbacks have been shown to be
1357 very efficient in Sputnik Planitia (Earle et al., 2018, Bertrand et al., 2020b). In particular,
1358 Bertrand et al. (2020b) showed that a local decrease in N_2 ice surface albedo from 0.7 to 0.65
1359 during northern spring is sufficient to turn a N_2 condensation-dominated region into a
1360 sublimation-dominated region (see Fig. 16 in Bertrand et al., 2020b). The processes mentioned in
1361 (1) and (2) can locally trigger a change in surface albedo and composition that is likely to
1362 amplify with time (e.g. local deposition of N_2 ice on bright surfaces and removal on dark
1363 surfaces) (4) The composition of the surface ice can also be impacted by ice segregation (e.g.
1364 formation of a CH_4-rich layer on top of a N_2-rich ice) and by the relaxation of the surface ice
1365 toward a ternary phase equilibrium, whose timescale and properties can vary locally depending
1366 on the local surface and atmospheric conditions (Protopapa et al., 2017, Schmitt et al., 2017, Tan
1367 and Kargel, 2019). (5) Transport of gaseous CH_4 by the near-surface winds in Sputnik Planitia
1368 can also favor CH_4 saturation above the surface at specific locations, and subsequent
1369 condensation and enrichment of the ice in CH_4. This is illustrated by Figure 28, which shows the
1370 diurnal mean near surface CH_4 atmospheric mixing ratio and the diurnal net CH_4 deposition in
1371 Sputnik Planitia, as predicted for July 2015 by global climate modeling of Pluto (Bertrand et al.,
1372 2020b). The 3D simulations show that the near-surface air in Sputnik Planitia is enriched in N_2
1373 (depleted in CH_4) compared to the air outside the basin. This is due to N_2 sublimation in Sputnik
1374 Planitia (and subsequent injection of cold N_2-rich air in the atmosphere) and to the confinement
1375 of this N_2-rich air by the high relief boundaries of the basin (Forget et al., 2017, Bertrand et al.,
1376 2020b). The near-surface northern regions of Sputnik Planitia were particularly depleted in CH_4
1377 in 2015 due to the north-to-south sublimation flow that transports gaseous CH_4 southward. Note
1378 that the wind patterns predicted by the model inside Sputnik Planitia become different at ~1 km

* Some feature names mentioned in this paper are now formalized while others are informal

above the surface, with a strong western boundary current and an anticlockwise wind spiral (see Bertrand et al., 2020b). Figure 28 (left) shows that higher amounts of near-surface gaseous CH_4 are obtained locally near the boundaries of the basin, or near the blocky mountains of the western and southern sides. This is due to downslope transport of the air which is outside the basin or above the blocky mountains and which is enriched in gaseous CH_4 (due to the absence of N_2 sublimation or the occurrence of local sublimation of CH_4-rich frosts that formed on these terrains). As a result, CH_4 deposition onto the plains of Sputnik Planitia is favored in the western, eastern and southern edge of Sputnik Planitia, and in particular near the blocky mountains and near the steepest slopes of the eastern side of Sputnik Planitia (Figure 28, right), where the air is highly enriched in gaseous CH_4 coming from the sublimation of the CH_4-rich Bladed Terrains.

Figure 24 A-O: Pie plots summarizing the composition of the geologic units in each province, as returned by the application of the Hapke-based spectral modeling.

Figure 25. Contrast between the northernmost mountain range of Al-Idrisi Montes and the southernmost range of Tenzing Montes. (a) Al-Idrisi Montes show minimal interstitial N_2 ice plains between mountain blocks. LORRI image is 76 m/pixel and centered at 37.6°N, 156.3°E, with illumination from the top. (b) Several of the mountain blocks of Tenzing Montes are partly engulfed by N_2 ice plains that are elevated by up to a kilometer above the surrounding N_2 ice plains of Sputnik Planitia, and separated from them by scarps (white arrows). MVIC image is 315 m/pixel and centered at 13.6°S, 176.7°E, with illumination from the top.

Figure 26. Scattered hills (unit sh) and dark ridged terrain (unit drt). (a) Scattered hills of Astrid and Soyuz Colles, which display smooth topographic relief and a high albedo, indicating that the hills, like the surrounding plains, have been coated by ongoing N_2 ice deposition. MVIC image is 315 m/pixel and centered at 14.7°N, 184.5°E, with illumination from the left. (b) Dark ridges situated between Baret Montes and dark-pitted, marginal plains of Sputnik Planitia, which were mapped as unit drt by White et al. (2017). White arrows indicate ridges spaced 1-2 km apart that align roughly parallel to the border of the unit with the N_2 ice plains. LORRI image is 117 m/pixel and centered at 11.4°N, 157.5°E, with illumination from the top. (c) Columbia Colles, located at the eastern margin of Sputnik Planitia, which were mapped as unit sh by White et al. (2017.) White arrows indicate ridges spaced 1-2 km apart that resemble those highlighted in (a). The comparable geomorphology and albedo of Columbia Colles to occurrences of unit drt in the west suggest that similar processes have affected Columbia Colles, which are otherwise separated stratigraphically and compositionally from unit drt. MVIC image is 315 m/pixel and centered at 28.7°N, 196.5°E, with illumination from the left.

Figure 27. Plains units of Sputnik Planitia described in sections 5.5 and 5.6. (a) Alcyonia Lacus, mapped by White et al. (2017) as an isolated occurrence of dark Cellular plains surrounded by mountains and blocky material of Al-Idrisi Montes. LORRI image is 117 m/pixel and centered at 36.4°N, 151.6°E, with illumination from the top-right. (b) Hummocky N2 ice plains of unit pmp covering low-lying uplands of Krun Macula (dark terrain at lower right). Scarps (white arrows) separate unit pmp from the flat plains of Sputnik Planitia, similar to those seen at Tenzing Montes (Fig. 26b). MVIC image is 315 m/pixel and centered at 5.8°S, 191.2°E, with illumination from the left. (c) Glacial flow of nitrogen ice from the bright pitted uplands of East Tombaugh Regio (bottom) into Sputnik Planitia. Dark, converging flow bands (white arrows) are seen in valleys that connect upland flats to Sputnik Planitia, and are interpreted to be moraine trails consisting of CH4-rich material eroded from the pitted uplands by N2 ice glaciation. MVIC image is 315 m/pixel and centered at 3.7°N, 193.6°E, with illumination from the top-right. (d) High-albedo, pitted plains of units dpp and spp located at the western edge of Sputnik Planitia, occurring interstitially to convective cells of the dark, Cellular plains (unit dcp). MVIC image is 315 m/pixel and centered at 20.3°N, 155.1°E, with illumination from the top. (e) Dense fields of aligned (unit dpp) in southern Sputnik Planitia. Across the center of the image, they are seen to form chains of

* Some feature names mentioned in this paper are now formalized while others are informal

joined, dark-floored pits that trace elongated, polygonal outlines that enclose sparsely pitted plains (unit spp), and which extend southwards from the bright, Cellular plains (unit bcp) at top left. MVIC image is 315 m/pixel and centered at 6.0°S, 179.7°E, with illumination from the left.

Figure 28: Results from the global climate model of Pluto obtained for July 2015 from simulations similar to those presented in Bertrand et al., 2020b. Left: Diurnal mean near-surface (~20 m) atmospheric CH_4 mass mixing ratio in the region of Sputnik Planitia, with near-surface winds. Right: Net diurnal CH_4 deposition onto the surface.

6. Conclusions

In this study of Sputnik Planitia, we have compared spectroscopic data of this region acquired by New Horizons' LEISA instrument to the geomorphology as mapped by White et al. (2017) using visible and panchromatic imaging acquired by the LORRI and LEISA instruments.

Sputnik Planitia is a unique geologic formation in our Solar System: it is a young and deep impact crater basin, hosting a large variety of diverse terrain types, who's surface veneer is made up of volatile ices captured by the cold trap created by its peculiar morphological shape. Terrain units typical of the basin's western rims, were also found inside the cellular plains, like the abm mountains, while the pitted plains covering the whole eastern edge of the planitia, are also frequent, in small patches, in most of the western territory.

The idea behind this work was then to comprehend if, and in which amount, the processes responsible for the ice deposition inside the basin influence the surface composition of units belonging to the very same geological type, but that are spatially separated.

We fit the units' average spectra with and Hapke theory-based modeling, and we created scatter plots comparing the integrated band depths of the main endmember's absorptions, to have a better vision of how the different surface components influence each other, and how this is reflected in the resulting surface spectra.

The analysis of the CH_4 integrated band depths in five wavelength ranges revealed their different sensitivities to variations in composition, grain size, and scattering properties.

* Some feature names mentioned in this paper are now formalized while others are informal

We expected to observe an anticorrelation between the CH_4 absorptions and the CH_4 shift index, and a positive trend between the N_2 integrated band depth and the shift parameter: spectral units hosting a large amount of N_2-rich ice would show high values of the shift parameter, whereas in areas where the CH_4-rich ice dominates, the CH_4 absorptions should manifest as small or null shifts. For three out of these six spectral indicators, the results were actually the opposite. The scatter plot of the CH_4 integrated band depths versus the shift index in Ranges 1, 2, and 4 showed, in fact, a positive correlation. We further noticed that the geologic units having weak CH_4 absorptions but small values of the CH_4 shift index are all located within the western mountain ranges, in addition to Columbia Colles. These units are also those that display the deepest absorptions relating to H_2O and tholins, leading us to the conclusion that the weakness of the CH_4 absorptions in Ranges 1, 2, and 4 for these units is not a consequence of low abundance of this material, but rather of a high concentration of other materials that mask its spectral signature or that surface particles in these units are more backscattering than those in the cellular plains. The broad CH_4 absorptions in Ranges 1, 2, and 4 saturate quickly, even though not linearly, with increasing CH_4 abundance, grain size, or forward scattering, while the absorption in Range 3 and the band centered at 1.48 μm, being weaker, require a larger quantity of CH_4 for reaching the saturation level. This conclusion is also supported by the absence of trends between the CH_4 absorptions in Ranges 1, 2, and 4 and the band in Range 3 (Figure 14).

We explored the correlation between the CH_4 and N_2 absorptions with the other endmembers considered - CO, H_2O, NSS endmember - to understand which one is the most responsible for the unexpected suppression of the absorptions in Ranges 1, 2, and 4 observed in Figure 13A.

From the comparison between the trends in Figure 13A and Figure 16A (CH_4 integrated band depths in Ranges 1, 2, and 4 versus the CO integrated band depth), we notice that geologic units

* Some feature names mentioned in this paper are now formalized while others are informal

showing deeper CH_4 absorptions and higher values of the CH_4 shift index also have strong CO bands. CH_4 in Range 3 and N_2, on the other hand, do not show any correlation to CO (Figure 16B). Grundy et al. (2013, 2014) and Schmitt et al. (2017) noticed, however, a strong correlation between CO and N_2, but not between CO and CH_4. Comparing the CO abundance map (Figure 15) to the areal mass fraction maps of N_2:CH_4 (Figure 11a) and pure β-N_2 (Figure 12a) confirms the observed connection between CO and N_2. The fact that this link doesn't manifest in the scatter plots of Figure 16 can signify that the contaminants affect the depth of the CO absorption as well, and that CO is not responsible for the observed anomaly in Figure 13A.

We then explored the mutual variation of the CH_4 and N_2 integrated band depths with the abundance of crystalline H_2O and the NSS endmember returned by the modeling. The results (from Figure 18 to Figure 22) indicate that the NSS endmember (likely tholins) or more backscattering particles are primarily responsible for the suppression of CH_4 absorptions in Ranges 1, 2, and 4 in the western mountainous units of Sputnik Planitia.

The Hapke theory-based modeling is a powerful tool to investigate the nature of the endmembers covering a planetary surface, but it is limited by the availability and the quality of the optical constants. For instance, in our modeling we could not include the contribution of the CO because of lack of reliable optical constants, making its important contribution to the observed spectra only partially explored. The same can be concluded for the refractory non-ice material responsible for the observed negative spectral slope in the NIR spectra. Because there is very little published information on the optical constants for tholins with a composition relevant to Pluto's surface, the nature of the non-ice material is still unknown.

The spectroscopic analyses of this study have provided additional insight into the geological processes that have shaped Sputnik Planitia, and in some instances they reveal aspects of the

* Some feature names mentioned in this paper are now formalized while others are informal

geology that is not apparent within the visible and panchromatic imaging that was used to define the geological units in the mapping of White et al. (2017). For non-plains units, a general increase in volatile abundance from the north to the south of Sputnik Planitia is seen, manifested especially by the higher areal mass fraction of N_2:CH_4 at the expense of H_2O ice for the southernmost mountains (unit abm) as compared to the northernmost ones. Higher amounts of pure CH_4 are also seen at the southern mountains, which are a natural site for CH_4 deposition owing to their high elevation and the lower insolation they are presently receiving; the existence of a thin veneer of pure CH_4 ice is only apparent in the spectra, and not in the visible imaging. Topography within southern Sputnik Planitia (specifically the scattered hills, Tenzing Montes and Krun Macula) that appears inundated by N_2 ice is interpreted as a geomorphological consequence of the increased deposition of volatiles occurring here, which is predicted by climate modeling (Bertrand et al., 2018; 2020b). The NSS endmember that has been identified in the spectra correlates to the existence of tholins within certain units, and are coating the low-latitude mountain ranges of Zheng He, Baret, and Hillary Montes (i.e. those that are co-latitudinal with the tholin-covered Cthulhu Macula in the uplands to the west) and the dark ridged terrain (unit drt); covering the floors of large pits within non-cellular plains; and are entrained within the exposed N_2 ice of Sputnik Planitia within the northern dark cellular plains and trough-bounding plains (units dcp and tbp). Our spectral and geomorphological observations have also revealed that Columbia Colles, which belong to the CH_4 ice-based scattered hills that have been eroded from the pitted uplands of East Tombaugh Regio (unit sh), appear to have been affected by processes somewhat similar to those that have formed the dark ridged terrain along the western boundary of Sputnik Planitia, which is based on much older, H_2O ice-based crustal material that also forms the western mountain ranges. Elevated CH_4

* Some feature names mentioned in this paper are now formalized while others are informal

concentrations within N_2:CH_4 ice of the eastern non-cellular plains may represent sub-resolution, CH_4-rich material that has been recently eroded from the pitted uplands of East Tombaugh Regio, and which is being transported into Sputnik Planitia by N_2 ice glaciers. The spectral analysis has also revealed compositional and/or directional scattering differences between the handful of occurrences of northern non-cellular plains and the surrounding cellular plains, all of which are located within the portion of Sputnik Planitia that is presently experiencing net sublimation of volatiles, and which do not therefore exhibit a surface layer of bright, freshly-deposited N_2 ice. The compositional differences between the cellular and non-cellular plains here hint at the effectiveness of convection in entraining and trapping tholins within the body of the cellular plains, while preventing the spread of such tholins to abutting non-cellular plains.

The results of this paper form a testament to the dynamism of volatile mobilization within the plains of Sputnik Planitia and its mountain ranges, with many factors including surface elevation, Pluto's highly variable climate with latitude, and endogenous factors (i.e. convection) all playing important roles in explaining our spectroscopic and geomorphological observations. As described by Bertrand et al. (2020b) Sputnik Planitia does represent the "beating heart" of Pluto that regulates its atmospheric circulation through such volatile mobilization, and the effects of this have consequences across the rest of the dwarf planet. Outside of Sputnik Planitia, both latitudinal and longitudinal variations in the distribution of surface volatiles have been described. The eastwards sequence of equatorial terrains from the bright pitted uplands of East Tombaugh Regio through the bladed terrain deposits of Tartarus Dorsa to the dark, tholin covered, cratered plains of Cthulhu Macula appear to manifest a surficial composition sequence from dominance by nitrogen directly to the east of Sputnik Planitia, to increasing dominance of methane ice farther to the east culminating in the bladed terrain deposits (Moore et al., 2018), eventually

* Some feature names mentioned in this paper are now formalized while others are informal

terminating at the volatile-poor expanse of Cthulhu Macula to the west of Sputnik Planitia. Development of albedo contrasts is heightened in the equatorial region, owing to its relatively stable climate (Earle et al., 2018), and is a powerful driving force behind the very pronounced segregation of volatile-rich and -poor terrains at the equator. The drastic climate cycles experienced by the northern latitudes promotes mixing of volatiles and causes them to neither be substantially eroded nor accumulated relative to the equatorial region, but longitudinal variation is still apparent, from the smooth, mantled, undulating uplands of Hayabusa and Pioneer Terrae to the northeast of Sputnik Planitia, to the very flat, heavily cratered, partly eroded plains of Vega and Venera Terrae to the northwest. At both at low and high latitudes, the observed longitudinal variation of uplands geomorphology may indicate an origin related to the retrorotation of Pluto's atmosphere that is controlled by Sputnik Planitia, and both further high-resolution, long-term global climate model simulations and comprehensive analysis of the spectral properties of terrains beyond Sputnik Planitia will complement geological observations to expand our understanding of volatile mobilization across Pluto in general.

* Some feature names mentioned in this paper are now formalized while others are informal

References

Ahrens, C. J., & Chevrier, V. F. (2019). Compressional Ridges on Baret Montes, Pluto as Observed by New Horizons. *Geophysical Research Letters*, *46*(24), 14328–14335. https://doi.org/10.1029/2019GL085648

Bertrand, T., Forget, F., Umurhan, O. M., Grundy, W. M., Schmitt, B., Protopapa, S., Zangari, A. M., White, O. L., Schenk, P. M., Singer, K. N., Stern, A., Weaver, H. A., Young, L. A., Ennico, K., & Olkin, C. B. (2018). The nitrogen cycles on Pluto over seasonal and astronomical timescales. *Icarus*, *309*, 277–296. https://doi.org/10.1016/j.icarus.2018.03.012

Bertrand, T., Forget, F., Umurhan, O. M., Moore, J. M., Young, L. A., Protopapa, S., Grundy, W. M., Schmitt, B., Dhingra, R. D., Binzel, R. P., Earle, A. M., Cruikshank, D. P., Stern, S. A., Weaver, H. A., Ennico, K., & Olkin, C. B. (2019). The CH 4 cycles on Pluto over seasonal and astronomical timescales. *Icarus*, *329*(December 2018), 148–165. https://doi.org/10.1016/j.icarus.2019.02.007

Bertrand, Tanguy, Forget, F., Schmitt, B., White, O. L., & Grundy, W. M. (2020a). Equatorial mountains on Pluto are covered by methane frosts resulting from a unique atmospheric process. *Nature Communications*, *11*(1), 1–7. https://doi.org/10.1038/s41467-020-18845-3

Bertrand, T., Forget, F., White, O., Schmitt, B., Stern, S. A., Weaver, H. A., Young, L. A., Ennico, K., & Olkin, C. B. (2020b). Pluto's Beating Heart Regulates the Atmospheric Circulation: Results From High-Resolution and Multiyear Numerical Climate Simulations. *Journal of Geophysical Research: Planets*, *125*(2), 1–64. https://doi.org/10.1029/2019JE006120

Bertrand, Tanguy, & Forget, F. (2016). Observed glacier and volatile distribution on Pluto from atmosphere-topography processes. *Nature*, *540*(7631), 86–89. https://doi.org/10.1038/nature19337

Bertrand, Tanguy, & Forget, F. (2017). 3D modeling of organic haze in Pluto's atmosphere. *Icarus*, *287*, 72–86. https://doi.org/10.1016/j.icarus.2017.01.016

Binzel, R. P., Earle, A. M., Buie, M. W., Young, L. A., Stern, S. A., Olkin, C. B., Ennico, K., Moore, J. M., Grundy, W., Weaver, H. A., Lisse, C. M., & Lauer, T. R. (2017). Climate zones on Pluto and Charon. *Icarus*, *287*, 30–36. https://doi.org/10.1016/j.icarus.2016.07.023

Brunetto, R., Caniglia, G., Baratta, G. A., & Palumbo, M. E. (2008). Integrated Near-Infrared Band Strengths of Solid CH 4 and Its Mixtures with N 2 . *The Astrophysical Journal*, *686*(2), 1480–1485. https://doi.org/10.1086/591509

Buhler, P. B., & Ingersoll, A. P. (2018). Sublimation pit distribution indicates convection cell surface velocities of ~10 cm per year in Sputnik Planitia, Pluto. *Icarus*, *300*, 327–340. https://doi.org/10.1016/j.icarus.2017.09.018

Buie, M. W., Grundy, W. M., Young, E. F., Young, L. A., & Stern, S. A. (2010). Pluto and charon with the hubble space telescope. II. Resolving changes on pluto's surface and a map for charon. *Astronomical Journal*, *139*(3), 1128–1143. https://doi.org/10.1088/0004-6256/139/3/1128

Buratti, B. J., Hofgartner, J. D., Hicks, M. D., Weaver, H. A., Stern, S. A., Momary, T., Mosher, J. A., Beyer, R. A., Verbiscer, A. J., Zangari, A. M., Young, L. A., Lisse, C. M., Singer, K., Cheng, A., Grundy, W., Ennico, K., & Olkin, C. B. (2017). Global albedos of Pluto and Charon from LORRI New Horizons observations. *Icarus*, *287*, 207–217. https://doi.org/10.1016/j.icarus.2016.11.012

Cheng, A. F., Summers, M. E., Gladstone, G. R., Strobel, D. F., Young, L. A., Lavvas, P.,

* Some feature names mentioned in this paper are now formalized while others are informal

Kammer, J. A., Lisse, C. M., Parker, A. H., Young, E. F., Stern, S. A., Weaver, H. A., Olkin, C. B., & Ennico, K. (2017). Haze in Pluto's atmosphere. *Icarus*, *290*, 112–133. https://doi.org/10.1016/j.icarus.2017.02.024

Cheng, A. F., Weaver, H. A., Conard, S. J., Morgan, M. F., Barnouin-Jha, O., Boldt, J. D., Cooper, K. A., Darlington, E. H., Grey, M. P., Hayes, J. R., Kosakowski, K. E., Magee, T., Rossano, E., Sampath, D., Schlemm, C., & Taylor, H. W. (2008). Long-range reconnaissance imager on New Horizons. *Space Science Reviews*, *140*(1–4), 189–215. https://doi.org/10.1007/s11214-007-9271-6

Cook, J. C., Dalle Ore, C. M., Protopapa, S., Binzel, R. P., Cruikshank, D. P., Earle, A., Grundy, W. M., Ennico, K., Howett, C., Jennings, D. E., Lunsford, A. W., Olkin, C. B., Parker, A. H., Philippe, S., Reuter, D., Schmitt, B., Singer, K., Stansberry, J. A., Stern, S. A., … Tegler, S. C. (2019). The distribution of H2O, CH3OH, and hydrocarbon-ices on Pluto: Analysis of New Horizons spectral images. *Icarus*, *331*, 148–169. https://doi.org/10.1016/j.icarus.2018.09.012

Cruikshank, D. P, Clemett, S. J., Grundy, W. M., Stern, S. A., Olkin, C. B., Binzel, R. P., Cook, J. C., Ore, C. M. D., Earle, A. M., Smith-Ennico, K., Jennings, D. E., Howett, C. J. A., Linscott, I. R., Lunsford, A. W., Parker, A. H., Parker, J. W., Protopapa, S., Reuter, D. C., Singer, K. N., … Hiroi, T. (2016). PLUTO AND CHARON: THE NON-ICE SURFACE COMPONENT. *Lunar and Planetary Science Conference XLVII*, 46–47. https://doi.org/10.1038/ngeo2474.

Cruikshank, D.P., Grundy, W. M., DeMeo, F. E., Buie, M. W., Binzel, R. P., Jennings, D. E., Olkin, C. B., Parker, J. W., Reuter, D. C., Spencer, J. R., Stern, S. A., Young, L. A., & Weaver, H. A. (2015). The surface compositions of Pluto and Charon. *Icarus*, *246*, 82–92. https://doi.org/10.1016/j.icarus.2014.05.023

Cruikshank, D.P., Pilcher, C. B., & Morrison, D. (1976). Pluto: Evidence for Methane Frost Abstract. *Science*, *194*(4268), 836. https://doi.org/10.1126/science.194.4268.935

Cruikshank, Dale P., Dalle Ore, C. M., Scipioni, F., Beyer, R. A., White, O. L., Moore, J. M., Grundy, W. M., Schmitt, B., Runyon, K. D., Keane, J. T., Robbins, S. J., Stern, S. A., Bertrand, T., Beddingfield, C. B., Olkin, C. B., Young, L. A., Weaver, H. A., & Ennico, K. (2020). Cryovolcanic flooding in Viking Terra on Pluto. *Icarus*, *November 2019*, 113786. https://doi.org/10.1016/j.icarus.2020.113786

Cruikshank, Dale P., Hamilton Brown, R., & Clark, R. N. (1984). Nitrogen on Triton. *Icarus*, *58*(2), 293–305. https://doi.org/10.1016/0019-1035(84)90046-0

Douté, S., Schmitt, B., Quirico, E., Owen, T. C., Cruikshank, D. P., De Bergh, C., Geballe, T. R., & Roush, T. L. (1999). Evidence for Methane Segregation at the Surface of Pluto. *Icarus*, *142*(2), 421–444. https://doi.org/10.1006/icar.1999.6226

Earle, A. M., Binzel, R. P., Young, L. A., Stern, S. A., Ennico, K., Grundy, W., Olkin, C. B., & Weaver, H. A. (2017). Long-term surface temperature modeling of Pluto. *Icarus*, *287*, 37–46. https://doi.org/10.1016/j.icarus.2016.09.036

Earle, A. M., Binzel, R. P., Young, L. A., Stern, S. A., Ennico, K., Grundy, W., Olkin, C. B., & Weaver, H. A. (2018). Albedo matters: Understanding runaway albedo variations on Pluto. *Icarus*, *303*, 1–9. https://doi.org/10.1016/j.icarus.2017.12.015

Gladstone, G. R., Stern, S. A., Ennico, K., Olkin, C. B., Weaver, H. A., Young, L. A., Summers, M. E., Strobel, D. F., Hinson, D. P., Kammer, J. A., Parker, A. H., Steffl, A. J., Linscott, I. R., Parker, J. W., Cheng, A. F., Slater, D. C., Versteeg, M. H., Greathouse, T. K., Retherford, K. D., … Tyler, G. L. (2016). The atmosphere of Pluto as observed by New

* Some feature names mentioned in this paper are now formalized while others are informal

1649 Horizons. *Science*, *351*(6279). https://doi.org/10.1126/science.aad8866
1650 Grundy, W. M., Bertrand, T., Binzel, R. P., Buie, M. W., Buratti, B. J., Cheng, A. F., Cook, J. C.,
1651 Cruikshank, D. P., Devins, S. L., Dalle Ore, C. M., Earle, A. M., Ennico, K., Forget, F.,
1652 Gao, P., Gladstone, G. R., Howett, C. J. A., Jennings, D. E., Kammer, J. A., Lauer, T. R., …
1653 Zhang, X. (2018). Pluto's haze as a surface material. *Icarus*, *314*(June), 232–245.
1654 https://doi.org/10.1016/j.icarus.2018.05.019
1655 Grundy, W. M., Binzel, R. P., Buratti, B. J., Cook, J. C., Cruikshank, D. P., Dalle Ore, C. M.,
1656 Earle, A. M., Ennico, K., Howett, C. J. A., Lunsford, A. W., Olkin, C. B., Parker, A. H.,
1657 Philippe, S., Protopapa, S., Quirico, E., Reuter, D. C., Schmitt, B., Singer, K. N., Verbiscer,
1658 A. J., … Young, L. A. (2016). Surface compositions across Pluto and Charon. *Science*,
1659 *351*(6279). https://doi.org/10.1126/science.aad9189
1660 Grundy, W. M. I., & Schmitt, B. (1998). The temperature-dependent near-infrared absorption
1661 spectrum of hexagonal ice. *Journal of Geophysical Research*, *103*, 809–822.
1662 Grundy, W. M., Olkin, C. B., Young, L. A., Buie, M. W., & Young, E. F. (2013). Near-infrared
1663 spectral monitoring of Pluto's ices: Spatial distribution and secular evolution. *Icarus*,
1664 *223*(2), 710–721. https://doi.org/10.1016/j.icarus.2013.01.019
1665 Grundy, W. M., Olkin, C. B., Young, L. A., & Holler, B. J. (2014). Near-infrared spectral
1666 monitoring of Pluto's ices II: Recent decline of CO and N2 ice absorptions. *Icarus*, *235*,
1667 220–224. https://doi.org/10.1016/j.icarus.2014.02.025
1668 Grundy, W. M., Schmitt, B., & Quirico, E. (1993). The Temperature-Dependent Spectra of α and
1669 β Nitrogen Ice with Application to Triton. In *Icarus* (Vol. 105, Issue 1, pp. 254–258).
1670 https://doi.org/10.1006/icar.1993.1122
1671 Grundy, W. M., Schmitt, B., & Quirico, E. (2002). The temperature-dependent spectrum of
1672 methane ice I between 0.7 and 5 μm and opportunities for near-infrared remote
1673 thermometry. *Icarus*, *155*(2), 486–496. https://doi.org/10.1006/icar.2001.6726
1674 Hamilton, D. P., Stern, S. A., Moore, J. M., & Young, L. A. (2016). The rapid formation of
1675 Sputnik Planitia early in Pluto's history. *Nature*, *540*(7631), 97–99.
1676 https://doi.org/10.1038/nature20586
1677 Hapke, B. W. (2012). *THEORY OF REFLECTANCE AND EMITTANCE SPECTROSCOPY* (B.
1678 Hapke (ed.); 2nd ed.). Cambridge University Press.
1679 Hapke, B. W., Nelson, R. M., & Smythe, W. D. (1993). The Opposition Effect of the Moon : The
1680 Contribution of Coherent Backscatter. *Science*, *23*(5107), 509–511.
1681 https://doi.org/10.1126/science.260.5107.509
1682 Howard, A. D., Moore, J. M., Umurhan, O. M., White, O. L., Anderson, R. S., McKinnon, W.
1683 B., Spencer, J. R., Schenk, P. M., Beyer, R. A., Stern, S. A., Ennico, K., Olkin, C. B.,
1684 Weaver, H. A., & Young, L. A. (2017). Present and past glaciation on Pluto. *Icarus*, *287*,
1685 287–300. https://doi.org/10.1016/j.icarus.2016.07.006
1686 Johnson, B. C., Bowling, T. J., Trowbridge, A. J., & Freed, A. M. (2016). Formation of the
1687 Sputnik Planum basin and the thickness of Pluto's subsurface ocean. *Geophysical Research*
1688 *Letters*, *43*(19), 10,068-10,077. https://doi.org/10.1002/2016GL070694
1689 Johnson, P. E., Young, L. A., Protopapa, S., Schmitt, B., Gabasova, L. R., Lewis, B. L.,
1690 Stansberry, J. A., Mandt, K. E., & White, O. L. (2020). Modeling Pluto's minimum
1691 pressure: Implications for haze production. *Icarus*, *August 2019*.
1692 https://doi.org/10.1016/j.icarus.2020.114070
1693 Keane, J. T., Matsuyama, I., Kamata, S., & Steckloff, J. K. (2016). Reorientation and faulting of
1694 Pluto due to volatile loading within Sputnik Planitia. *Nature*, *540*(7631), 90–93.

* Some feature names mentioned in this paper are now formalized while others are informal

https://doi.org/10.1038/nature20120
Khare, B. N., Sagan, C., Arakawa, E. T., Suits, F., Callcott, T. A., & Williams, M. W. (1984). Optical constants of organic tholins produced in a simulated Titanian atmosphere: From soft x-ray to microwave frequencies. *Icarus*, *60*(1), 127–137. https://doi.org/10.1016/0019-1035(84)90142-8
Khare, B. N., Sagan, C., Heinrich, M., Thompson, W. R., Arakawa, E. T., Tuminello, P. S., & Clark, M. (1994). Optical Constants of Triton Tholin: Preliminary Results. *American Astronomical Society, DPS Meeting*, *26*, 1176.
Khare, B. N., Thompson, W. R., Cheng, L., Chyba, C., Sagan, C., Arakawa, E. T., Meisse, C., & Tuminello, P. S. (1993). Production and Optical Constants of Ice Tholin from Charged Particle Irradiation of (1:6) C2H6/H2O at 77 K. In *Icarus* (Vol. 103, Issue 2, pp. 290–300). https://doi.org/10.1006/icar.1993.1071
Lorenzi, V., Pinilla-Alonso, N., Licandro, J., Cruikshank, D. P., Grundy, W. M., Binzel, R. P., & Emery, J. P. (2016). The spectrum of Pluto, 0.40-0.93 μm: I. Secular and longitudinal distribution of ices and complex organics. *Astronomy and Astrophysics*, *585*, 1–12. https://doi.org/10.1051/0004-6361/201527281
Lunine, J. I., & Stevenson, D. J. (1985). Physics and Chemistry of sulfur lakes on Io. *Icarus*, *64*(3), 345–367. https://doi.org/10.1016/0019-1035(85)90060-0
Mastrapa, R. M., Bernstein, M. P., Sandford, S. A., Roush, T. L., Cruikshank, D. P., & Ore, C. M. D. (2008). Optical constants of amorphous and crystalline H2O-ice in the near infrared from 1.1 to 2.6 μm. *Icarus*, *197*(1), 307–320. https://doi.org/10.1016/j.icarus.2008.04.008
Materese, C. K., Cruikshank, D. P., Sandford, S. A., Imanaka, H., & Nuevo, M. (2015). ICE CHEMISTRY on OUTER SOLAR SYSTEM BODIES: ELECTRON RADIOLYSIS of N2-, CH4-, and CO-CONTAINING ICES. *Astrophysical Journal*, *812*(2), 150. https://doi.org/10.1088/0004-637X/812/2/150
Materese, C. K., Cruikshank, D. P., Sandford, S. A., Imanaka, H., Nuevo, M., & White, D. W. (2014). ICE chemistry on outer solar system bodies: Carboxylic acids, NITRILES, and urea detected in refractory residues produced from the UV photolysis of N 2:CH4:Co-containing ices. *Astrophysical Journal*, *788*(2). https://doi.org/10.1088/0004-637X/788/2/111
McKinnon, W. B., Nimmo, F., Wong, T., Schenk, P. M., White, O. L., Roberts, J. H., Moore, J. M., Spencer, J. R., Howard, A. D., Umurhan, O. M., Stern, S. A., Weaver, H. A., Olkin, C. B., Young, L. A., & Smith, K. E. (2016). Convection in a volatile nitrogen-ice-rich layer drives Pluto's geological vigour. *Nature*, *534*(7605), 82–85. https://doi.org/10.1038/nature18289
Merlin, F. (2015). New constraints on the surface of Pluto. *Astronomy and Astrophysics*, *582*, 1–9. https://doi.org/10.1051/0004-6361/201526721
Moore, J.M., McKinnon, W. B., Spencer, J. R., Howard, A. D., Schenk, P. M., Beyer, R. A., Nimmo, F., Singer, K. N., Umurhan, O. M., White, O. L., Stern, S. A., Ennico, K., Olkin, C. B., Weaver, H. A., Young, L. A., Binzel, R. P., & Wilhelms, D. E. (2016). The geology of Pluto and Charon through the eyes of New Horizons. *Science*, *351*(6279).
Moore, Jeffrey M., Howard, A. D., Umurhan, O. M., White, O. L., Schenk, P. M., Beyer, R. A., McKinnon, W. B., Spencer, J. R., Singer, K. N., Grundy, W. M., Earle, A. M., Schmitt, B., Protopapa, S., Nimmo, F., Cruikshank, D. P., Hinson, D. P., Young, L. A., Stern, S. A., Weaver, H. A., … Scipioni, F. (2018). Bladed Terrain on Pluto: Possible origins and evolution. *Icarus*, *300*, 129–144. https://doi.org/10.1016/j.icarus.2017.08.031
Nimmo, F., Hamilton, D. P., McKinnon, W. B., Schenk, P. M., Binzel, R. P., Bierson, C. J.,

* Some feature names mentioned in this paper are now formalized while others are informal

Beyer, R. A., Moore, J. M., Stern, S. A., Weaver, H. A., Olkin, C. B., Young, L. A., & Smith, K. E. (2016). Reorientation of Sputnik Planitia implies a subsurface ocean on Pluto. *Nature*, *540*(7631), 94–96. https://doi.org/10.1038/nature20148

O'Hara, S. T., & Dombard, A. J. (2020). Downhill sledding at 40 AU: Mobilizing Pluto's chaotic mountain blocks. *Icarus*, 113829. https://doi.org/10.1016/j.icarus.2020.113829

Olkin, C. B.; Young, E. F.; Young, L. A.; Grundy, W.; Schmitt, B.; Tokunaga, A.; Owen, T.; Roush, T.; Terada, H. (2007). Pluto's Spectrum from 1.0 to 4.2 μm: Implications for Surface Properties. The Astronomical Journal, Volume 133, Issue 2, pp. 420-431.

Owen, T. C., Roush, T. L., Cruikshank, D. P., Elliot, J. L., Young, L. A., de Bergh, C., Schmitt, B., Geballe, T. R., Brown, R. H., & Bartholomew, M. J. (1993). Surface Ices and the Atmospheric Composition of Pluto. *Science*, *261*(5122), 745–748. https://doi.org/10.1126/science.261.5122.745

Prokhvatilov, A. I., & Yantsevich, L. D. (1983). X-ray investigation of the equilibrium phase diagram of CH4-N2 solid mixtures. *Sov. J. Low Temp. Phys.*, *9*, 94–98.

Protopapa, S. et al. (2021). Surface Composition of Charon. In: Stern, S.A., Young, L. A., Moore, J.M., Grundy, W.M., Binzel, R.P., (Eds.), The Pluto System. University of Arizona Press, Tucson.

Protopapa, S., et al. (2020). Disk-resolved Photometric Properties of Pluto and the Coloring Materials across its Surface. *The Astronomical Journal*, *159*, 74

Protopapa, S., Grundy, W. M., Reuter, D. C., Hamilton, D. P., Dalle Ore, C. M., Cook, J. C., Cruikshank, D. P., Schmitt, B., Philippe, S., Quirico, E., Binzel, R. P., Earle, A. M., Ennico, K., Howett, C. J. A., Lunsford, A. W., Olkin, C. B., Parker, A., Singer, K. N., Stern, A., … Young, L. A. (2017). Pluto's global surface composition through pixel-by-pixel Hapke modeling of New Horizons Ralph/LEISA data. *Icarus*, *287*, 218–228. https://doi.org/10.1016/j.icarus.2016.11.028

Protopapa, S., Grundy, W. M., Tegler, S. C., & Bergonio, J. M. (2015). Absorption coefficients of the methane-nitrogen binary ice system: Implications for Pluto. *Icarus*, *253*, 179–188. https://doi.org/10.1016/j.icarus.2015.02.027

Protopapa, S. et al. (2008) Surface characterization of Pluto and Charon by L and M band spectra. *A&A*, *490*, 365-375.

Quirico, E., & Schmitt, B. (1997). A spectroscopic study of CO diluted in N2 ice: Applications for Triton and Pluto. *Icarus*, *128*(1), 181–188. https://doi.org/10.1006/icar.1997.5710

Reuter, D. C., Stern, S. A., Scherrer, J., Jennings, D. E., Baer, J. W., Hanley, J., Hardaway, L., Lunsford, A., McMuldroch, S., Moore, J. M., Olkin, C. B., Parizek, R., Reitsma, H., Sabatke, D., Spencer, J., Stone, J., Throop, H. B., Van Cleve, J., Weigle, G. E., & Young, L. A. (2009). Ralph: A visible/infrared imager for the new horizons pluto/kuiper belt mission. *New Horizons: Reconnaissance of the Pluto-Charon System and the Kuiper Belt*, *Mvic*, 129–154. https://doi.org/10.1007/978-0-387-89518-5_7

Robbins, S. J., Singer, K. N., Bray, V. J., Schenk, P., Lauer, T. R., Weaver, H. A., Runyon, K., McKinnon, W. B., Beyer, R. A., Porter, S., White, O. L., Hofgartner, J. D., Zangari, A. M., Moore, J. M., Young, L. A., Spencer, J. R., Binzel, R. P., Buie, M. W., Buratti, B. J., … Stern, S. A. (2017). Craters of the Pluto-Charon system. *Icarus*, *287*(July 2015), 187–206. https://doi.org/10.1016/j.icarus.2016.09.027

Schenk, P. M., Beyer, R. A., McKinnon, W. B., Moore, J. M., Spencer, J. R., White, O. L., Singer, K., Nimmo, F., Thomason, C., Lauer, T. R., Robbins, S. J., Umurhan, O. M., Grundy, W. M., Stern, S. A., Weaver, H. A., Young, L. A., Ennico Smith, K., & Olkin, C.

* Some feature names mentioned in this paper are now formalized while others are informal

(2018). Basins, fractures and volcanoes: Global cartography and topography of Pluto from New Horizons. *Icarus*, *314*(June), 400–433. https://doi.org/10.1016/j.icarus.2018.06.008

Schmitt, B., Philippe, S., Grundy, W. M., Reuter, D. C., Côte, R., Quirico, E., Protopapa, S., Young, L. A., Binzel, R. P., Cook, J. C., Cruikshank, D. P., Dalle Ore, C. M., Earle, A. M., Ennico, K., Howett, C. J. A., Jennings, D. E., Linscott, I. R., Lunsford, A. W., Olkin, C. B., … Weaver, H. A. (2017). Physical state and distribution of materials at the surface of Pluto from New Horizons LEISA imaging spectrometer. *Icarus*, *287*, 229–260. https://doi.org/10.1016/j.icarus.2016.12.025

Schmitt, B., & Quirico, E. (1992). Laboratory Data on Near-Infrared Spectra of Ices of Planetary Interest. *American Astronomical Society, 24th DPS Meeting*.

Singer, K. N., McKinnon, W. B., Gladman, B., Greenstreet, S., Bierhaus, E. B., Stern, S. A., Parker, A. H., Robbins, S. J., Schenk, P. M., Grundy, W. M., Bray, V. J., Beyer, R. A., Binzel, R. P., Weaver, H. A., Young, L. A., Spencer, J. R., Kavelaars, J. J., Moore, J. M., Zangari, A. M., … Ennico, K. (2019). Impact craters on Pluto and Charon indicate a deficit of small Kuiper belt objects. *Science*, *363*(6430), 955–959. https://doi.org/10.1126/science.aap8628

Skjetne, H. L., Singer, K. N., Hynek, B. M., Knight, K. I., Schenk, P. M., Olkin, C. B., White, O. L., Bertrand, T., Runyon, K. D., McKinnon, W. B., Moore, J. M., Stern, S. A., Weaver, H. A., Young, L. A., & Ennico, K. (2020). Morphological comparison of blocks in chaos terrains on Pluto, Europa, and Mars. *Icarus*, 113866. https://doi.org/10.1016/j.icarus.2020.113866

Stephan, K., Jaumann, R., Krohn, K., Schmedemann, N., Zambon, F., Tosi, F., Carrozzo, F. G., McFadden, L. A., Otto, K., De Sanctis, M. C., Ammannito, E., Matz, K. D., Roatsch, T., Preusker, F., Raymond, C. A., & Russell, C. T. (2017). An investigation of the bluish material on Ceres. *Geophysical Research Letters*, *44*(4), 1660–1668. https://doi.org/10.1002/2016GL071652

Stern, S. A., Bagenal, F., Ennico, K., Gladstone, G. R., Grundy, W. M., McKinnon, W. B., Moore, J. M., Olkin, C. B., Spencer, J. R., Weaver, H. A., Young, L. A., Andert, T., Andrews, J., Banks, M., Bauer, B., Bauman, J., Barnouin, O. S., Bedini, P., Beisser, K., … Zirnstein, E. (2015). The pluto system: Initial results from its exploration by New Horizons. *Science*, *350*(6258). https://doi.org/10.1126/science.aad1815

Stern, S. A., Binzel, R. P., Earle, A. M., Singer, K. N., Young, L. A., Weaver, H. A., Olkin, C. B., Ennico, K., Moore, J. M., McKinnon, W. B., & Spencer, J. R. (2017). Past epochs of significantly higher pressure atmospheres on Pluto. *Icarus*, *287*, 47–53. https://doi.org/10.1016/j.icarus.2016.11.022

Trowbridge, A. J., Melosh, H. J., Steckloff, J. K., & Freed, A. M. (2016). Vigorous convection as the explanation for Pluto's polygonal terrain. *Nature*, *534*(7605), 79–81. https://doi.org/10.1038/nature18016

Verbiscer, A. J., Peterson, D. E., Skrutskie, M. F., Cushing, M., Helfenstein, P., Nelson, M. J., Smith, J. D., & Wilson, J. C. (2006). Near-infrared spectra of the leading and trailing hemispheres of Enceladus. *Icarus*, *182*(1), 211–223. https://doi.org/10.1016/j.icarus.2005.12.008

Verbiscer, A., Showalter, M., Helfenstein, P., & Buie, M. (2019). The Pluto System at True Opposition. *EPSC-DPS Joint Meeting*, *13*.

Wei, Q., Hu, Y., Liu, Y., Lin, D. N. C., Yang, J., & Showman, A. P. (2018). Young Surface of Pluto's Sputnik Planitia Caused by Viscous Relaxation. *The Astrophysical Journal*, *856*(1),

* Some feature names mentioned in this paper are now formalized while others are informal

L14. https://doi.org/10.3847/2041-8213/aab54f
White, O. L., Moore, J. M., McKinnon, W. B., Spencer, J. R., Howard, A. D., Schenk, P. M., Beyer, R. A., Nimmo, F., Singer, K. N., Umurhan, O. M., Stern, S. A., Ennico, K., Olkin, C. B., Weaver, H. A., Young, L. A., Cheng, A. F., Bertrand, T., Binzel, R. P., Earle, A. M., … Schmitt, B. (2017). Geological mapping of Sputnik Planitia on Pluto. *Icarus*, *287*, 261–286. https://doi.org/10.1016/j.icarus.2017.01.011
Young, L. A., Kammer, J. A., Steffl, A. J., Gladstone, G. R., Summers, M. E., Strobel, D. F., Hinson, D. P., Stern, S. A., Weaver, H. A., Olkin, C. B., Ennico, K., McComas, D. J., Cheng, A. F., Gao, P., Lavvas, P., Linscott, I. R., Wong, M. L., Yung, Y. L., Cunningham, N., … Versteeg, M. (2018). Structure and composition of Pluto's atmosphere from the New Horizons solar ultraviolet occultation. *Icarus*, *300*, 174–199. https://doi.org/10.1016/j.icarus.2017.09.006

* Some feature names mentioned in this paper are now formalized while others are informal

Appendix

Table: CH_4 shift parameter and integrated band depths calculated for the average spectra of the 48 provinces of Sputnik Planitia

Province*	CH_4 shift parameter	Integrated band depths						
		CH_4 Range 1 1.30 - 1.43 μm	CH_4 Range 2 1.59 - 1.83 μm	CH_4 Range 3 1.90 - 2.00 μm	CH_4 Range 4 2.09 - 2.48 μm	CH_4 1.48 μm	N_2 2.15 μm	CO 1.58 μm
ABM								
Baret Montes	0.003	0.08	0.07	0.05	0.12	0.02	0.02	0.009
Cellular plains	0.004	0.29	0.36	0.06	0.58	0.04	0.03	0.04
Hillary Montes	0.001	0.17	0.18	0.08	0.31	0.03	0.01	0.003
Southwest buffer	0.003	0.29	0.32	0.11	0.50	0.04	0.02	0.04
Tenzing Montes	0.002	0.23	0.27	0.10	0.45	0.04	0.01	0.02
Zheng He Montes	0.001	0.19	0.21	0.07	0.36	0.02	0.01	0.00
Al-Idrisi Montes	0.005	0.15	0.23	0.04	0.42	0.17	0.16	0.009
BCP								
Cellular plains	0.006	0.29	0.41	0.05	0.62	0.04	0.06	0.03
BCT								
Al-Idrisi Montes	0.007	0.08	0.18	0.02	0.46	0.004	0.08	0.002
DCP								
Cellular plains	0.005	0.27	0.36	0.05	0.58	0.04	0.04	0.02
Al-Idrisi Montes	0.007	0.14	0.26	0.02	0.48	0.03	0.06	0.01
DMP								
Baret	0.002	0.29	0.34	0.07	0.52	0.05	0.03	0.01

* Some feature names mentioned in this paper are now formalized while others are informal

Montes								
Hillary Montes	0.003	0.29	0.34	0.08	0.52	0.04	0.03	0.02
DPP								
Hillary Montes	0.002	0.27	0.31	0.09	0.49	0.05	0.04	0.01
North pitted plains	0.005	0.25	0.36	0.05	0.58	0.04	0.06	0.02
Cellular plains	0.004	0.30	0.38	0.06	0.58	0.05	0.04	0.02
East pitted plains	0.005	0.29	0.40	0.06	0.59	0.05	0.04	0.03
South pitted plains	0.004	0.30	0.39	0.07	0.60	0.05	0.06	0.02
West pitted plains	0.003	0.30	0.36	0.06	0.57	0.04	0.06	0.02
DRT								
Baret Montes	0.002	0.06	0.05	0.04	0.09	0.008	0.01	0.00
Hillary Montes	0.004	0.15	0.16	0.09	0.27	0.02	0.02	0.00
Al-Idrisi Montes	0.003	0.06	0.05	0.05	0.12	0.002	0.02	0.009
IBM								
Baret Montes	0.003	0.16	0.18	0.07	0.33	0.04	0.02	0.01
Hillary Montes	0.002	0.24	0.28	0.08	0.43	0.04	0.04	0.01
Tenzing Montes	0.003	0.25	0.32	0.10	0.51	0.04	0.03	0.03
Al-Idrisi Montes	0.005	0.11	0.20	0.04	0.40	0.01	0.04	0.008
LPP								
Hillary Montes	0.003	0.31	0.35	0.07	0.57	0.04	0.06	0.00
East pitted plains	0.005	0.30	0.41	0.06	0.62	0.04	0.06	0.03
South pitted plains	0.006	0.27	0.40	0.04	0.62	0.03	0.08	0.03
Cellular plains	0.005	0.29	0.39	0.04	0.60	0.04	0.05	0.04
Al-Idrisi Montes	0.005	0.21	0.30	0.06	0.49	0.03	0.02	0.004
PMP								
East pitted plains	0.004	0.30	0.40	0.07	0.59	0.05	0.04	0.02
Southwest buffer	0.003	0.31	0.36	0.10	0.55	0.05	0.02	0.02

* Some feature names mentioned in this paper are now formalized while others are informal

South pitted plains	0.004	0.29	0.39	0.07	0.58	0.05	0.03	0.02
Tenzing Montes	0.003	0.25	0.36	0.07	0.57	0.03	0.02	0.03
SH								
Astrid Colles	0.005	0.27	0.39	0.05	0.59	0.05	0.04	0.03
Challenger Colles	0.003	0.26	0.34	0.06	0.52	0.03	0.04	0.02
Columbia Colles	0.003	0.18	0.23	0.04	0.40	0.03	0.04	0.01
Soyuz Colles	0.005	0.33	0.40	0.06	0.60	0.04	0.008	0.03
East pitted plains	0.005	0.30	0.40	0.07	0.61	0.03	0.04	0.02
SPP								
Hillary Montes	0.003	0.33	0.39	0.08	0.59	0.04	0.05	0.01
East pitted plains	0.005	0.30	0.38	0.06	0.60	0.02	0.05	0.03
South pitted plains	0.005	0.29	0.40	0.05	0.61	0.04	0.08	0.03
North pitted plains	0.005	0.27	0.35	0.03	0.59	0.04	0.07	0.01
Cellular plains	0.005	0.29	0.38	0.03	0.60	0.04	0.05	0.03
Southwest buffer	0.003	0.33	0.41	0.08	0.62	0.05	0.06	0.03
West pitted plains	0.003	0.30	0.37	0.06	0.59	0.05	0.07	0.02
TBP								
Cellular plains	0.005	0.22	0.21	0.04	0.54	0.02	0.04	0.01

1889

* Some feature names mentioned in this paper are now formalized while others are informal

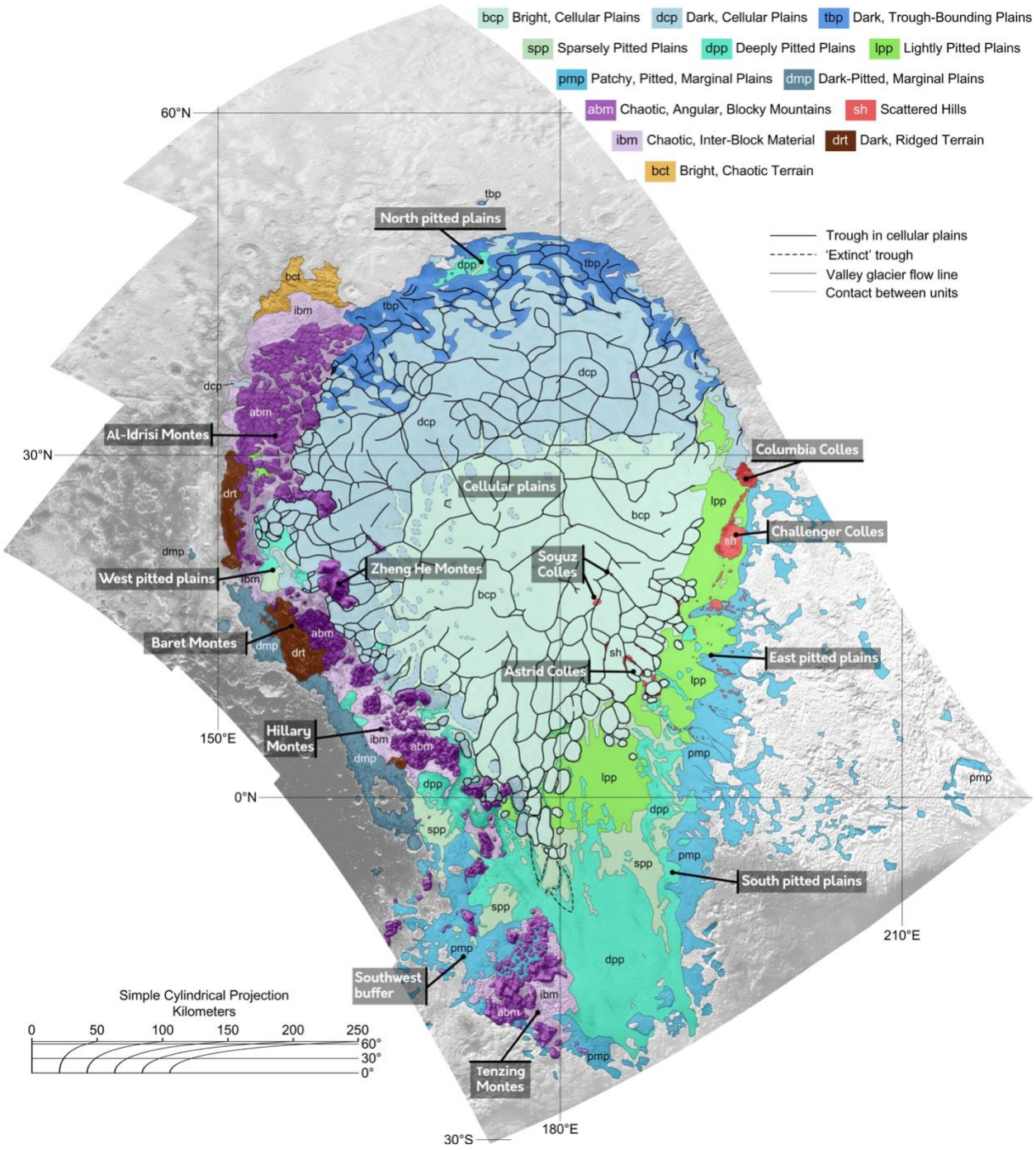

Figure 1: *Geologic units identified in Sputnik Planitia by White et al. (2017) through analysis of New Horizons LORRI images. The original 15 units initially identified were reduced to 13 here, to include only the geologic units within and around Sputnik Planitia. The basemap mosaic is a combination of 12 LORRI images, with a spatial resolution of 386 m/px.*

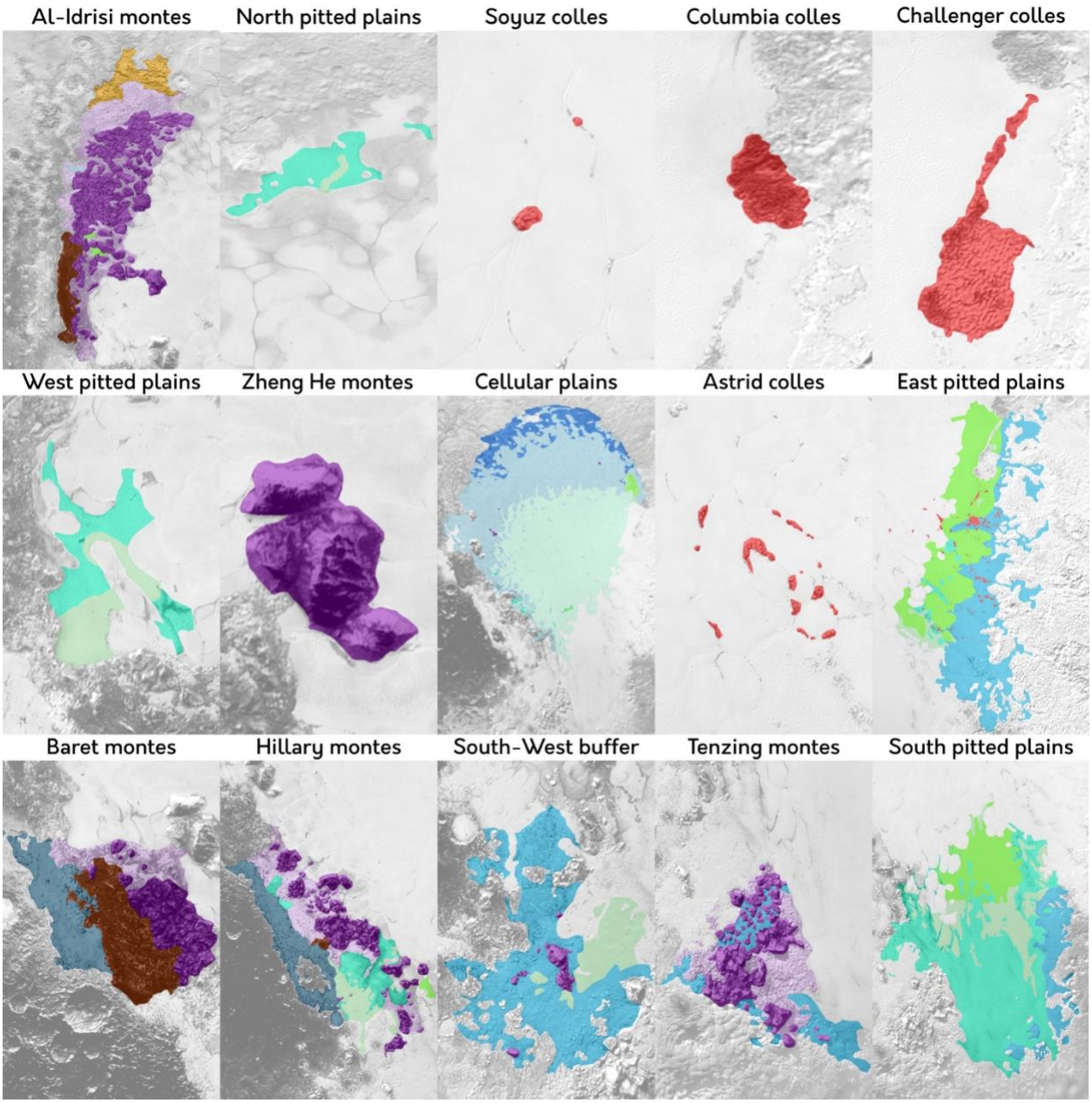

Figure 2: *The 15 provinces that we have divided the Sputnik Planitia geologic map into, with each province containing one or more geologic unit. Indeed, some geologic unit covers areas that are spatially distant and surrounded by very divers terrain types. For example, spp unit can be found in 5 different provinces: in the northernmost part of Sputnik Planitia (North Pitted Plains), embedded in the cellular plains; in the West Pitted Plains, again close to the cellular plains, but also to the blocky mountains; in the Hillary Montes region, surrounded by inter-blocky material; in the South-West Buffer and the South-East Pitted Plains, where the other types of pitted plains dominate.*

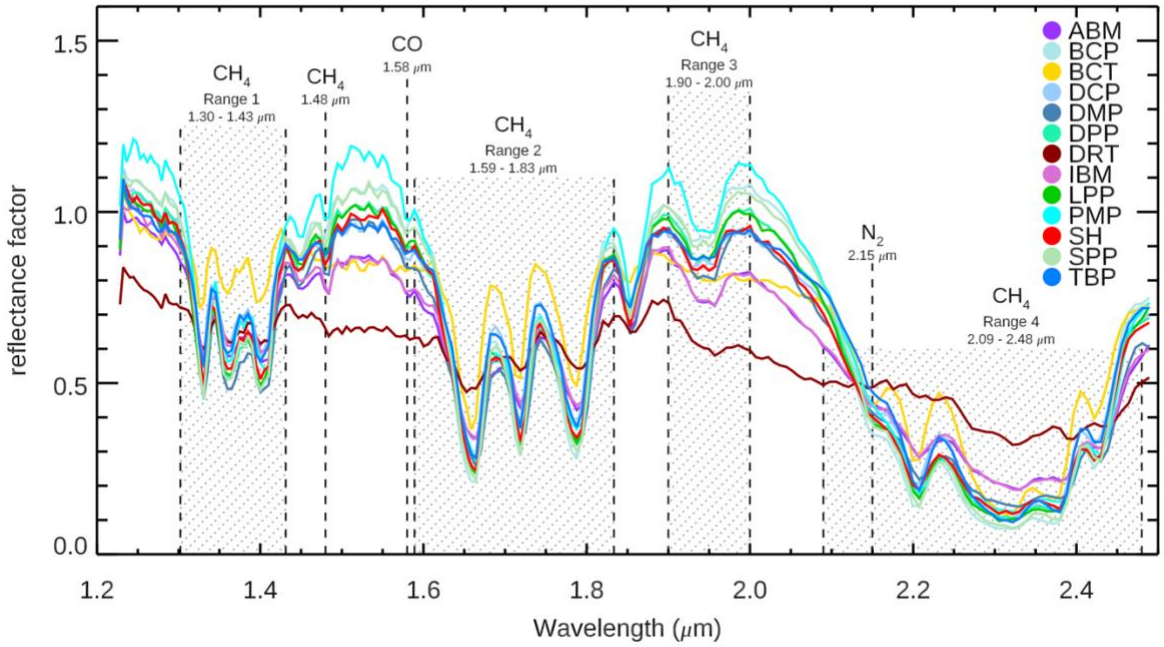

Figure 3: *Average spectra of the 13 geologic units identified by White et al. (2017). The boxes indicate the location of the main absorption bands of CH_4, CO and N_2.*

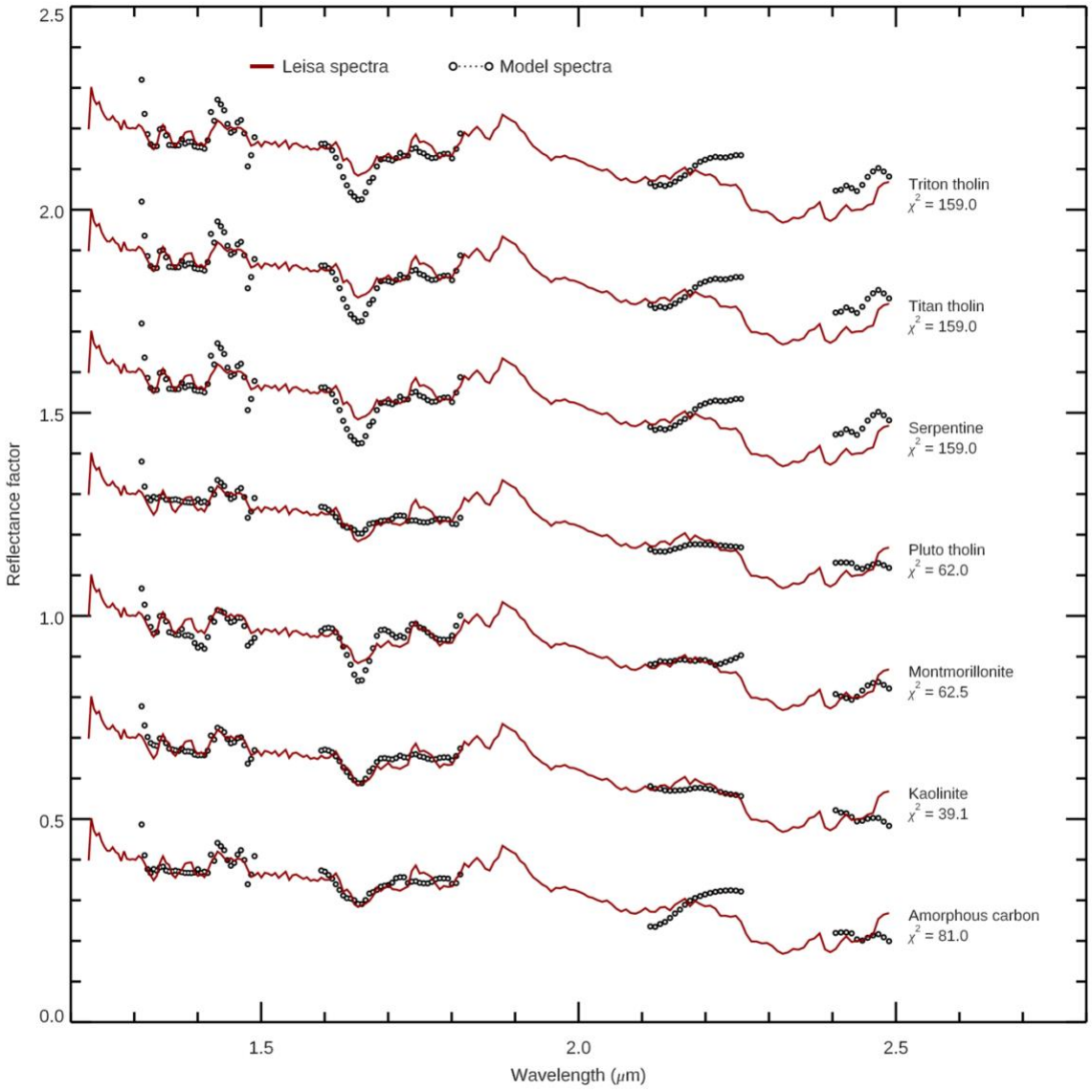

Figure 4: *LEISA spectra of unit drt in Baret overlapped by seven Hapke theory-based best fit models, calculated by considering the optical constants of seven different materials to account for the observed negative spectral slope. The spectra are offset for clarity.*

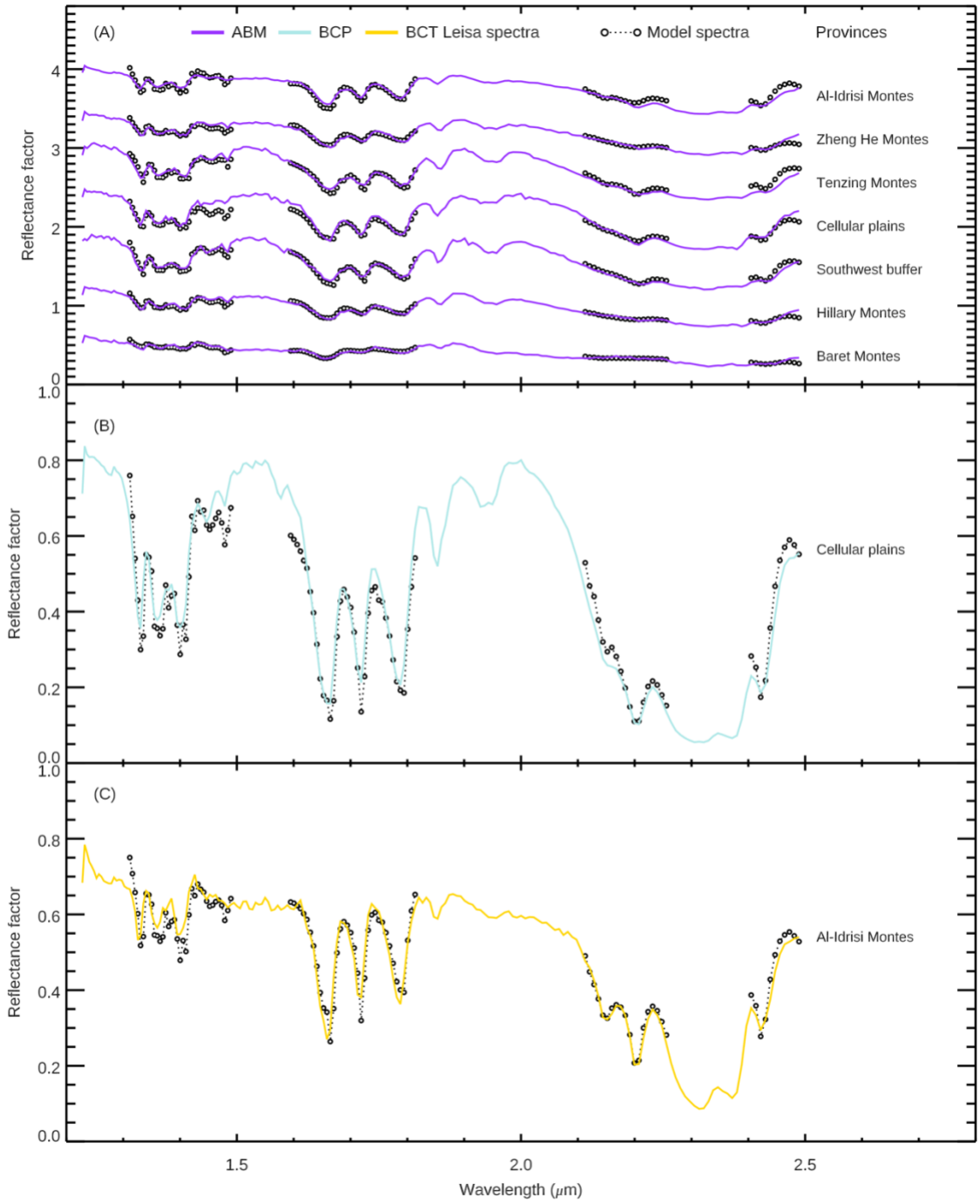
(A)
ABM
BCP
BCT Leisa spectra
Model spectra
Provinces
Al-Idrisi Montes
Zheng He Montes
Tenzing Montes
Cellular plains
Southwest buffer
Hillary Montes
Baret Montes
Reflectance factor
(B)
Cellular plains
Reflectance factor
(C)
Al-Idrisi Montes
Reflectance factor
Wavelength (μm)

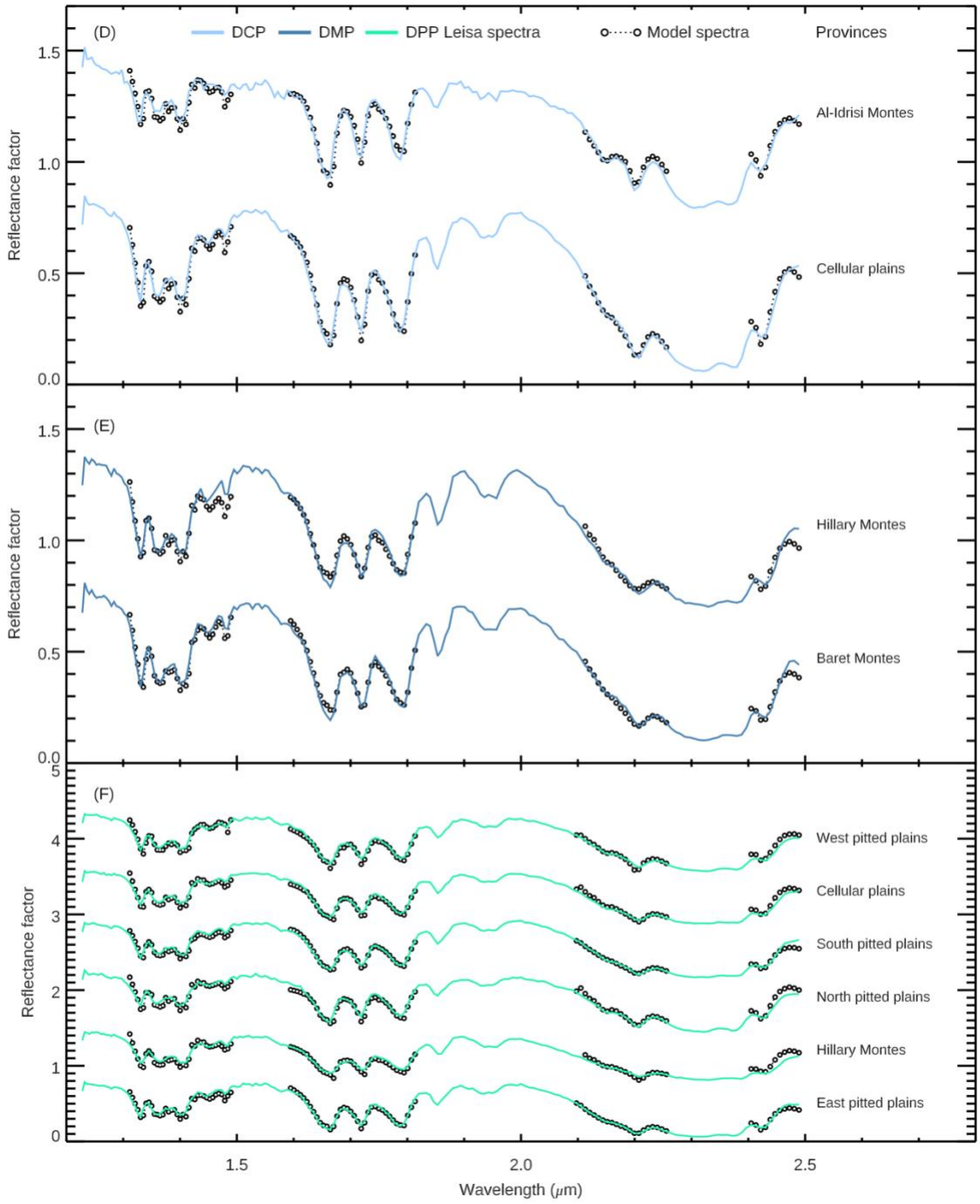
(D)
DCP
DMP
DPP Leisa spectra
Model spectra
Provinces
Al-Idrisi Montes
Cellular plains
(E)
Hillary Montes
Baret Montes
(F)
West pitted plains
Cellular plains
South pitted plains
North pitted plains
Hillary Montes
East pitted plains
Reflectance factor
Wavelength (μm)
0.0
0.5
1.0
1.5
2.0
2.5
0
1
2
3
4
5

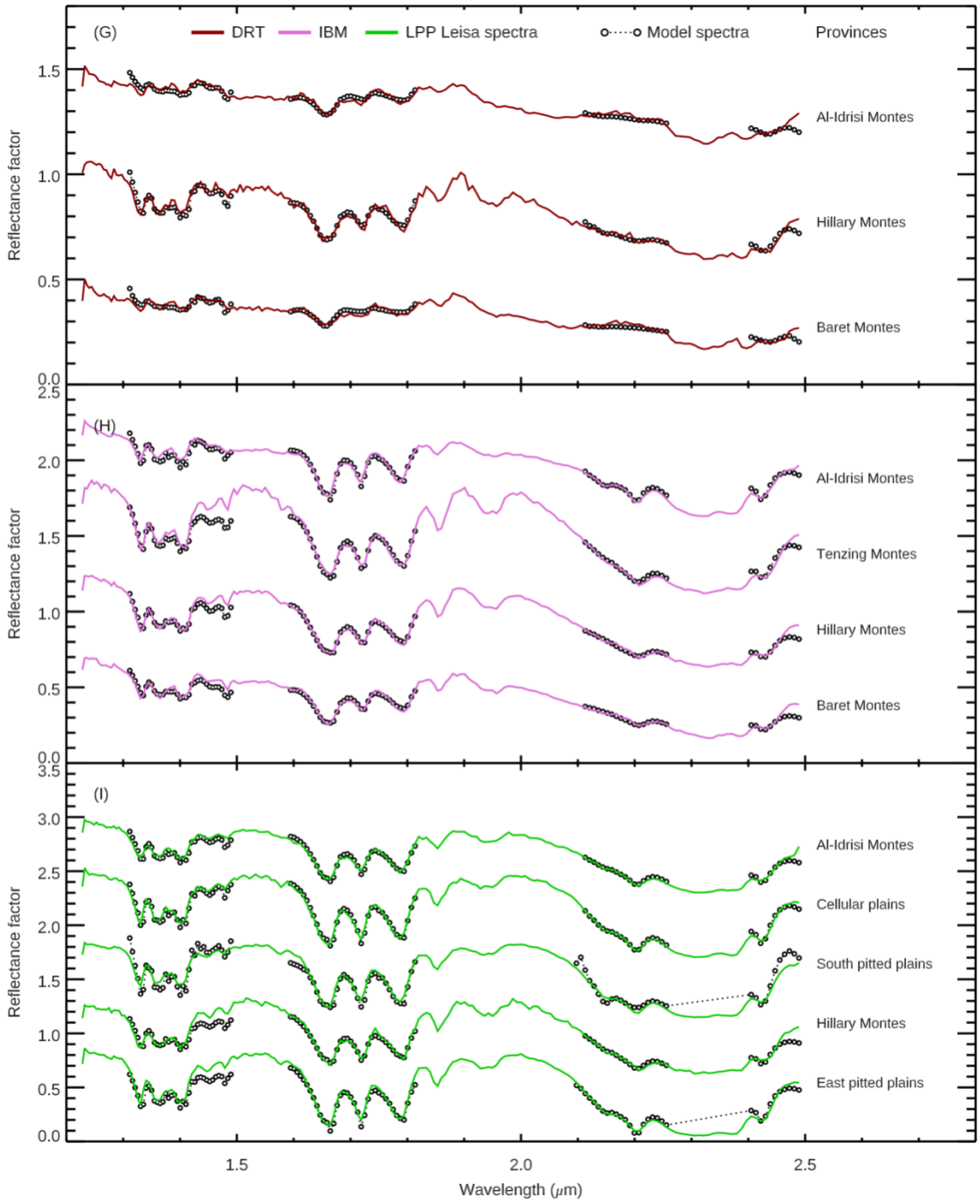
(G)
DRT
IBM
LPP Leisa spectra
Model spectra
Provinces
Al-Idrisi Montes
Hillary Montes
Baret Montes
(H)
Al-Idrisi Montes
Tenzing Montes
Hillary Montes
Baret Montes
(I)
Al-Idrisi Montes
Cellular plains
South pitted plains
Hillary Montes
East pitted plains
Reflectance factor
Wavelength (μm)
1.5
2.0
2.5

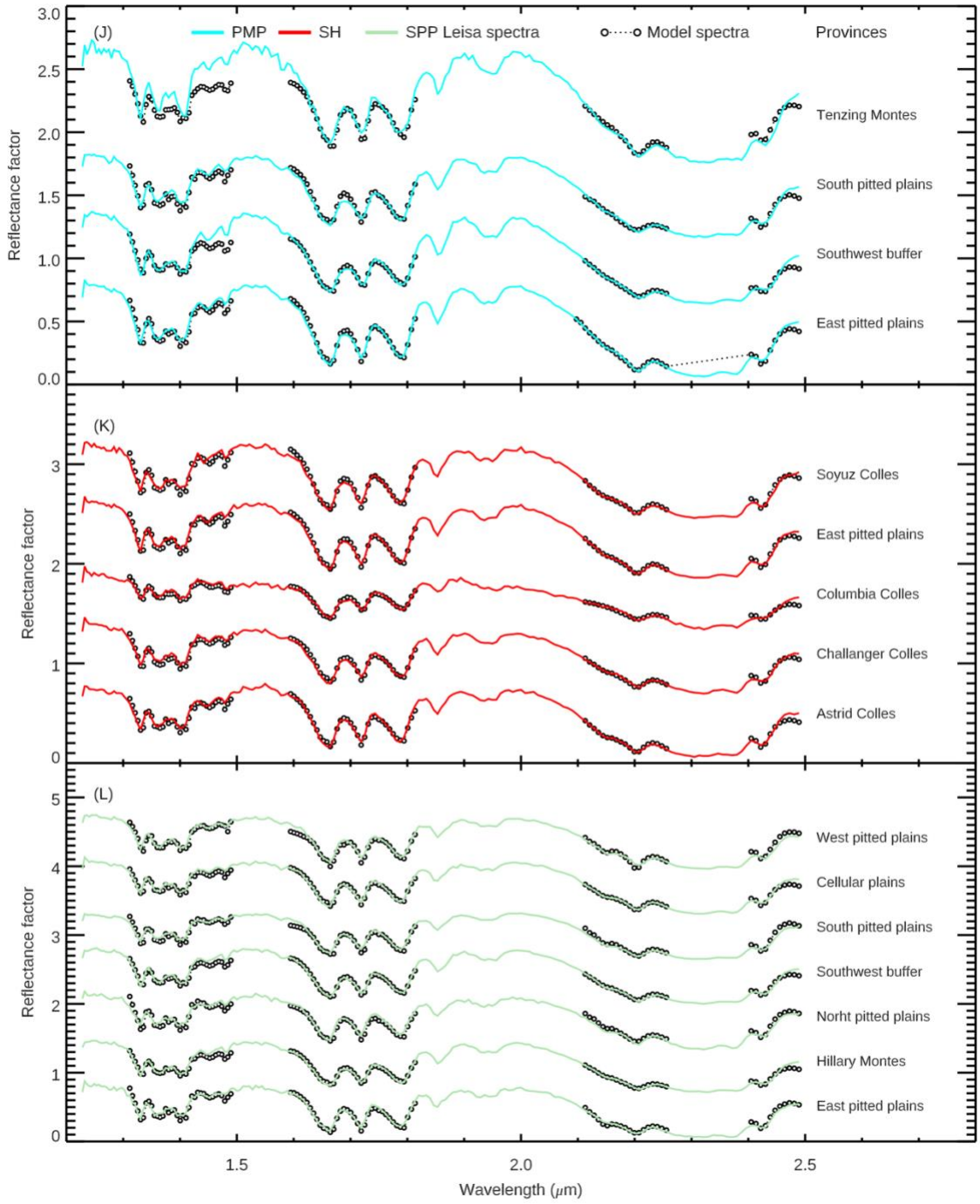
(J)
PMP
SH
SPP Leisa spectra
Model spectra
Provinces
Tenzing Montes
South pitted plains
Southwest buffer
East pitted plains
(K)
Soyuz Colles
East pitted plains
Columbia Colles
Challanger Colles
Astrid Colles
(L)
West pitted plains
Cellular plains
South pitted plains
Southwest buffer
Norht pitted plains
Hillary Montes
East pitted plains
Reflectance factor
Wavelength (μm)

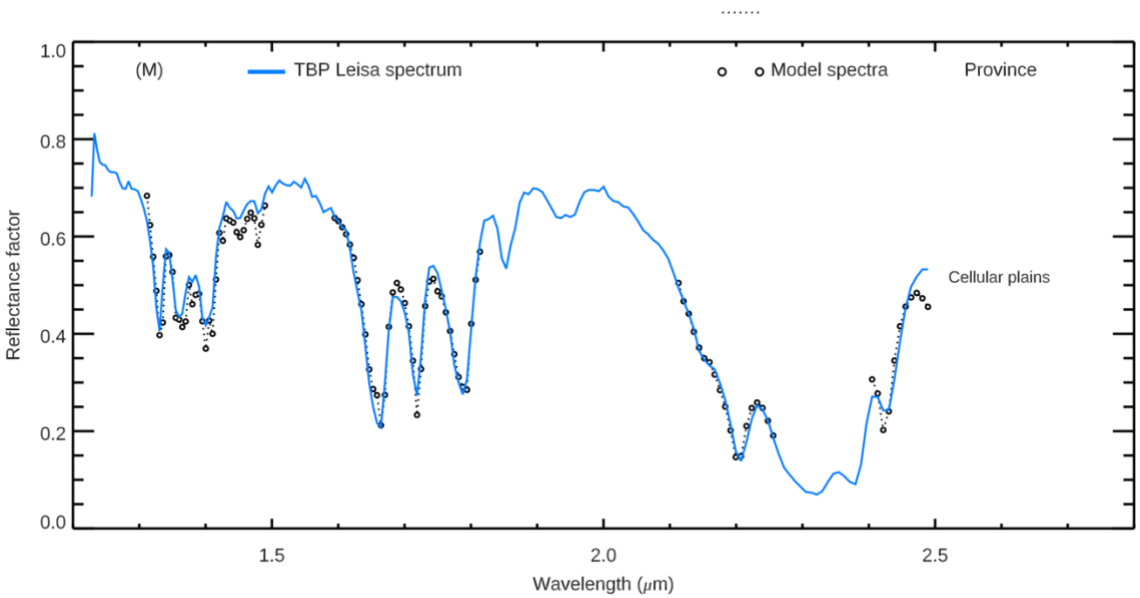

Figure 5A-M: *Comparison between LEISA spectra, averaged for each geologic unit in the 15 provinces, and the models calculated by applying the Hapke theory. Each panel also reports the components used in the models, with their fractional area.*

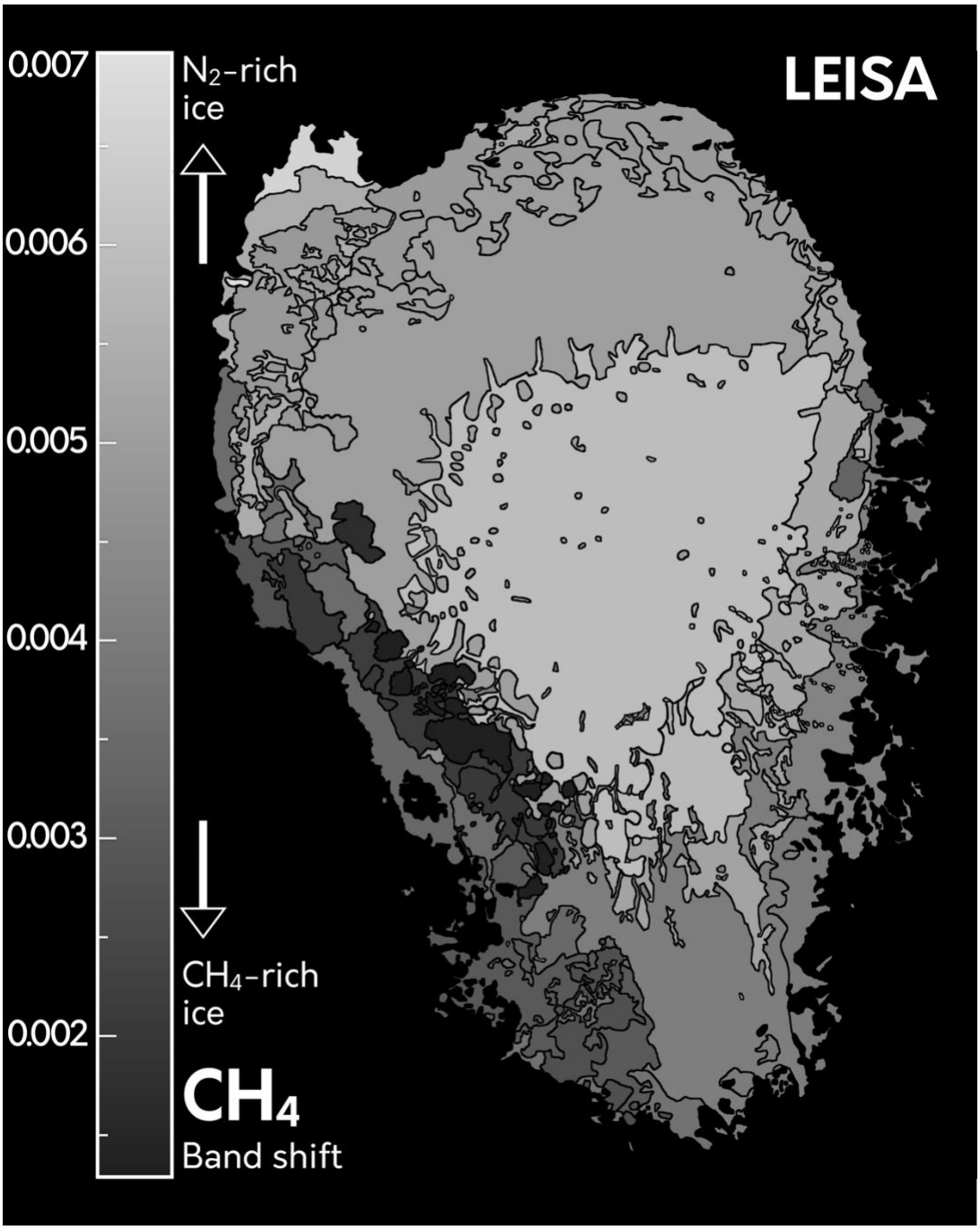

Figure 6: *Variation of the CH_4 band shift index across the geologic units of Sputnik Planitia. The highest values of the band shift index in the map (light grey) indicate areas characterized by N_2-rich ice, while the lowest values (dark grey) indicate CH_4-rich ice.*

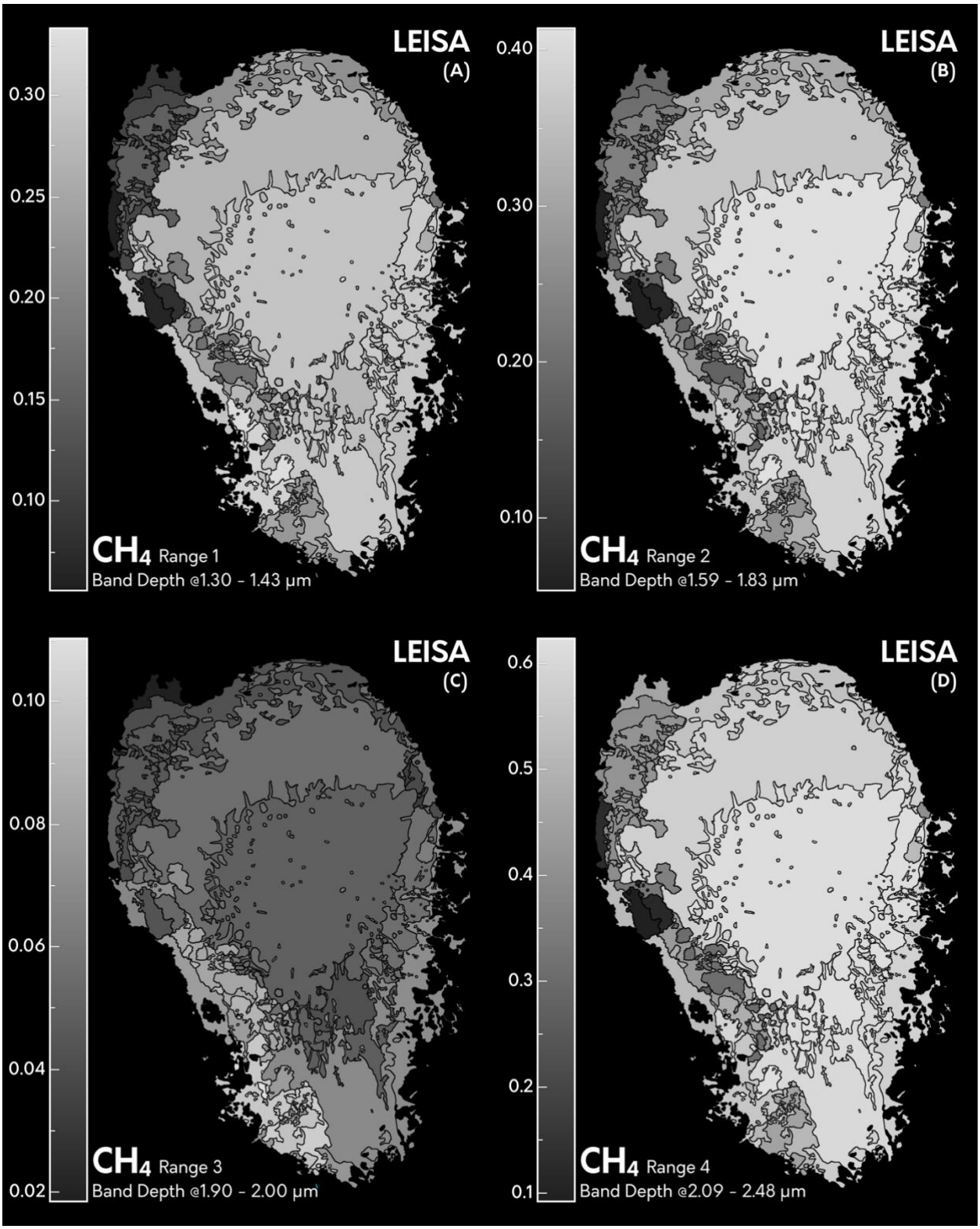
LEISA
(A)
0.30
0.25
0.20
0.15
0.10
CH4 Range 1
Band Depth @1.30 - 1.43 µm
LEISA
(B)
0.40
0.30
0.20
0.10
CH4 Range 2
Band Depth @1.59 - 1.83 µm
LEISA
(C)
0.10
0.08
0.06
0.04
0.02
CH4 Range 3
Band Depth @1.90 - 2.00 µm
LEISA
(D)
0.6
0.5
0.4
0.3
0.2
0.1
CH4 Range 4
Band Depth @2.09 - 2.48 µm

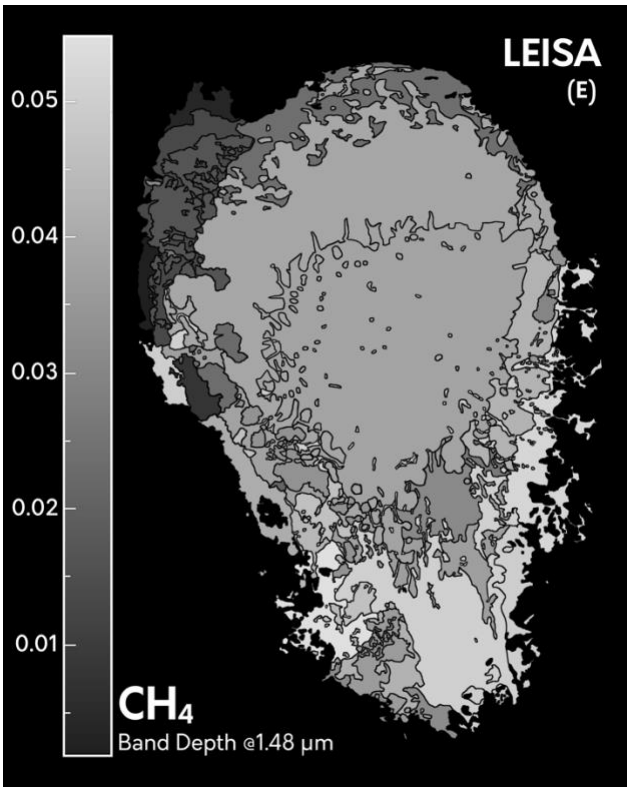

Figure 7 A-E: *Maps of variation of the integrated band depths of the main CH_4 absorptions: Range 1 (1.30-1.43 µm; A), Range 2 (1.59-1.83 µm; B), Range 3 (1.90-2.00 µm; C), Range 4 (2.09-2.48 µm; D), and the single band at 1.48 µm (E). The Range 3 map (C) shows opposite trends compared to the other four spectral ranges, a behavior that was previously observed also in other studies (e.g. Schmitt et al, 2017).*

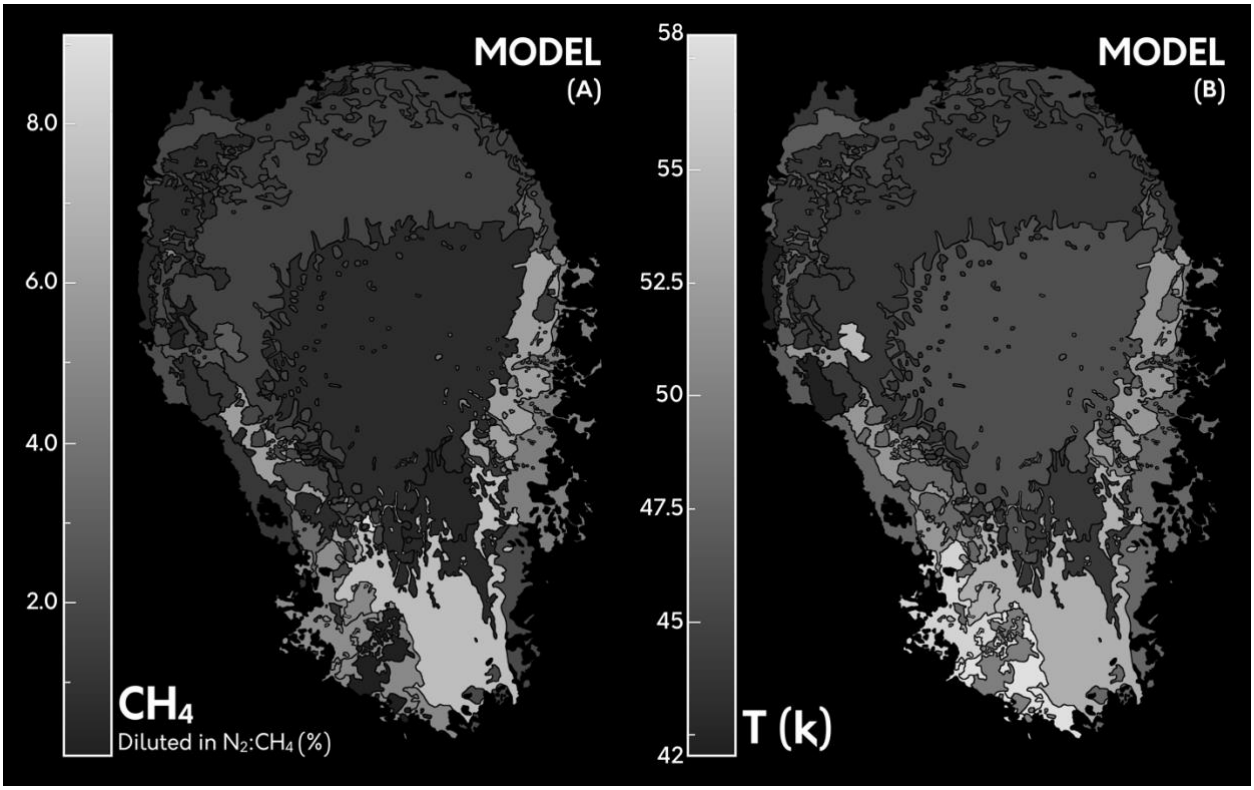

Figure 8A-B: *Maps of percentage variation of CH_4 diluted in N_2-rich ice (A) and temperatures (B) estimated by the spectral modeling.*

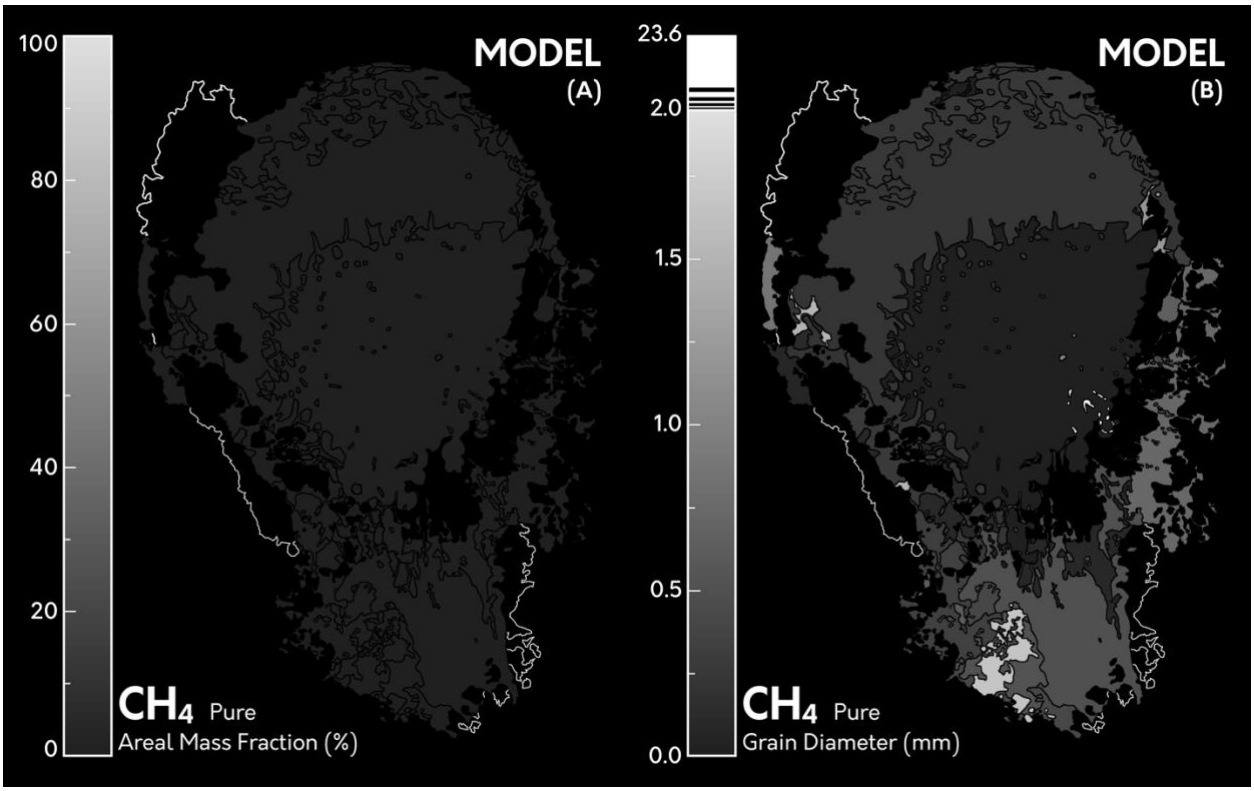

Figure 9A-B: *Maps of variation of pure CH4 areal mass fraction (A) and grain size (A) estimated by the spectral modeling. Pure CH4 covers almost all geologic units in Sputnik Planitia, but its percentage is very low, below 1.5%.*

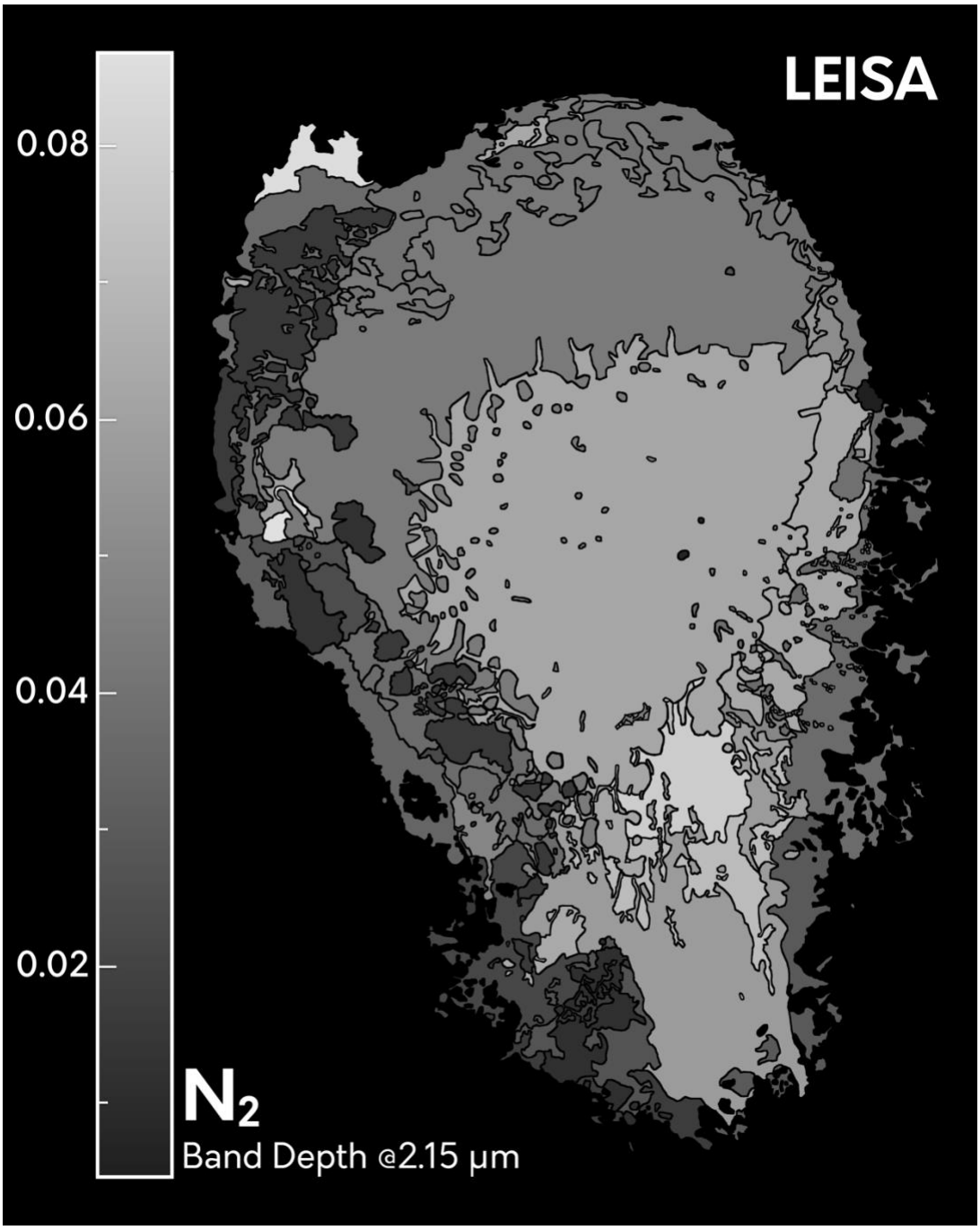

***Figure 10**: Map of variation of the integrated band depth of N_2 at 2.15 µm.*

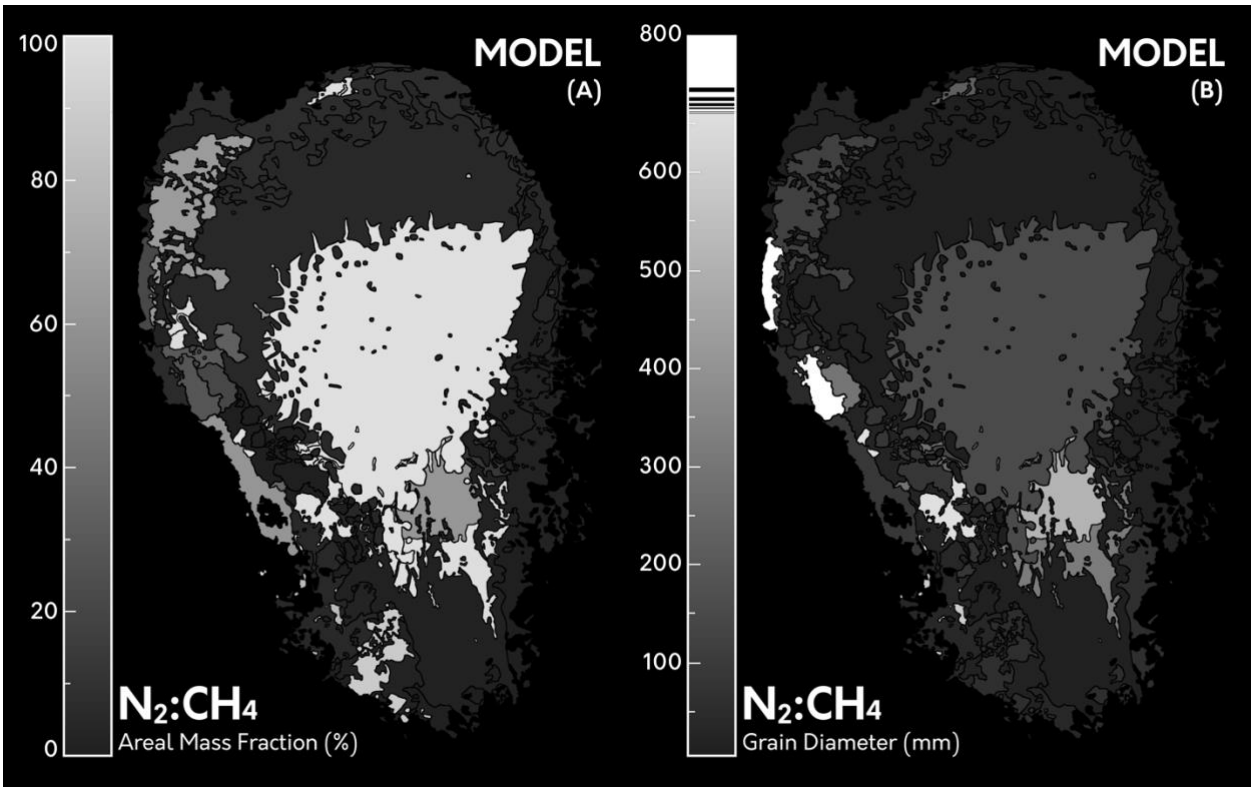

***Figure 11A-B**: Maps of variation of N_2:CH_4 areal mass fraction (A) and grain size (B) estimated by the spectral modeling.*

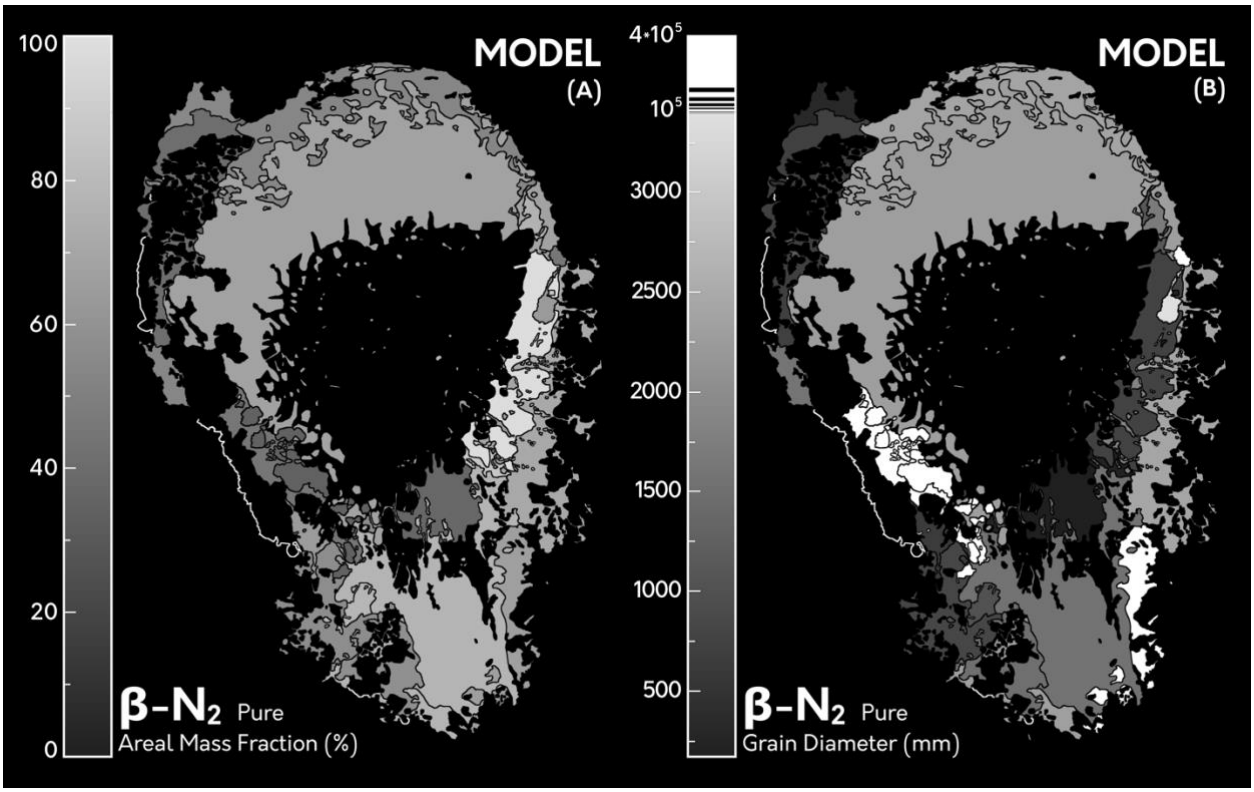

***Figure 12A-B:** Maps of variation of pure β-N_2 areal mass fraction (A) and grain size (B) estimated in the spectral modeling.*

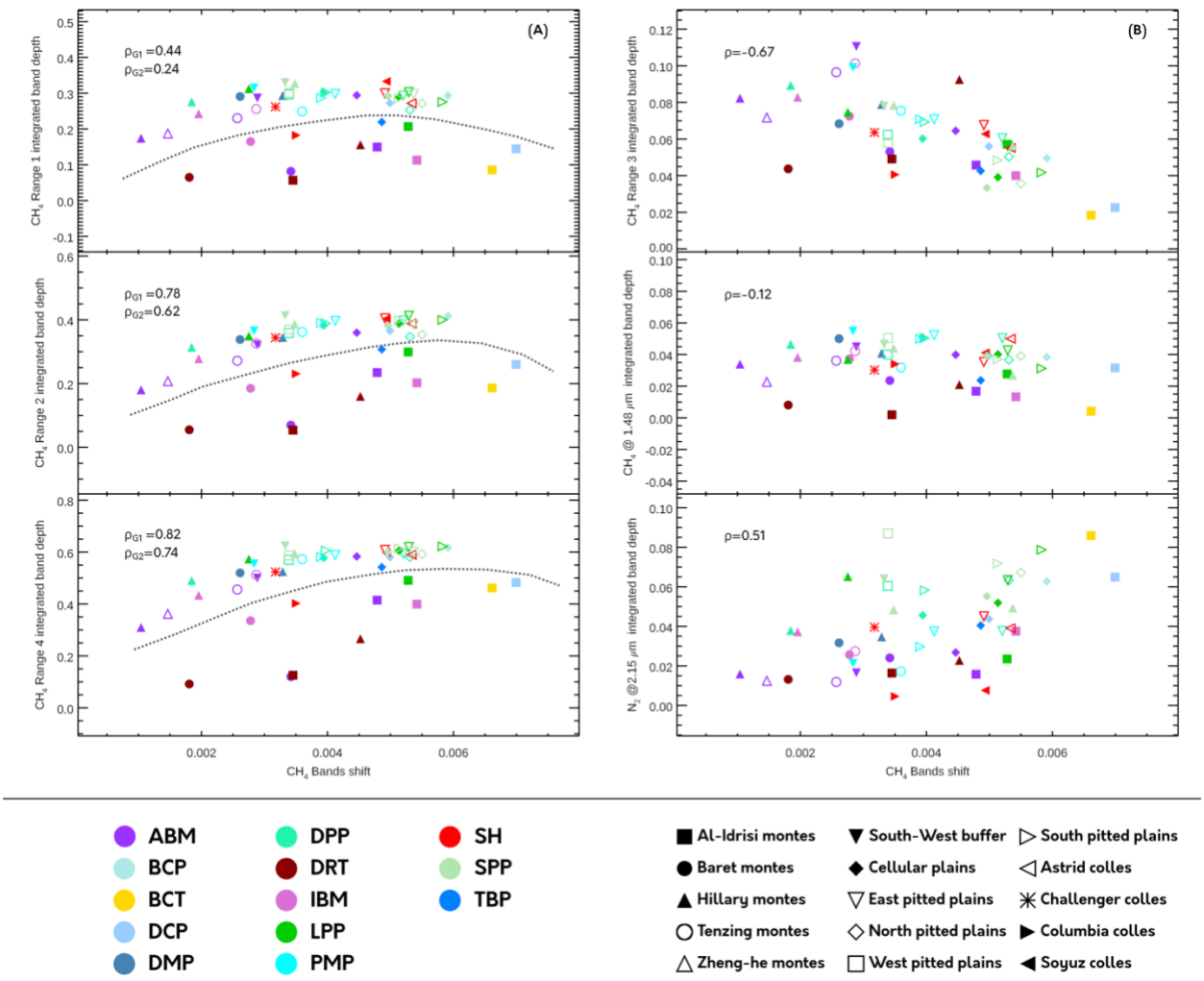

Figure 13: (A) *Scatter plot showing the correlation between the CH4 integrated band depth in Ranges 1 (top), 2 (middle), and 4 (bottom) with the CH4 shift index. The data are split into two groups, separated by a dotted curve. The points belonging to group G1, above the curve, show increasing band strength with increasing values of the shift parameter. The second group (G2), below the dotted line, also shows a positive trend, but the points are more dispersed. Furthermore, the values of the CH4 integrated band depths in G2 are lower than the units in G1. The positive trends in both groups contradicts the definition of the CH4 shift index, i.e. higher index values correspond to lower of CH4-rich ice amount. Therefore, a trend opposite of what observed in panel A is expected: the CH4 integrated band depth should be less intense - or, the abundance of methane should decrease - with increasing values of the shift index.* ***(B)*** *Scatter plot showing the correlation between the CH4 integrated band depth in Range 3 (top), at 1.48 μm (middle), and the N2 integrated band depth at 2.15 μm (bottom) with the CH4 shift index. As opposite to the three plots in panel A, these spectral parameters show a clear and single trend with the CH4 shift index, in agreement with the definition of the CH4 shift index.*

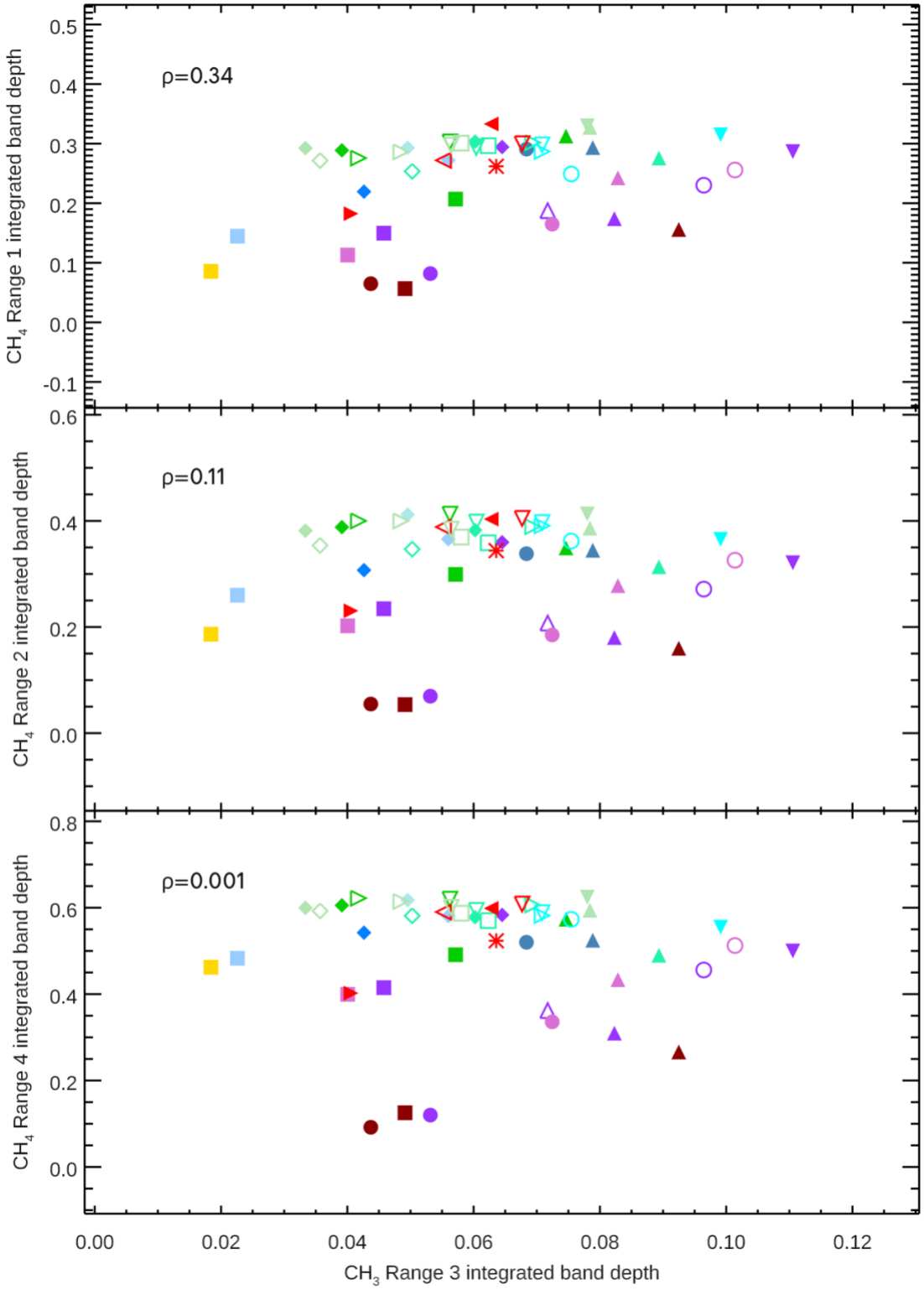

Figure 14: *Scatter plot showing the correlation between the CH4 integrated band depths in Ranges 1 (top), 2 (middle), and 4 (bottom) versus the CH4 integrated band depth in Range 3. The plots clearly show a lack of correlation between the represented parameters, indicating that the factor influencing the depth of the CH4 absorptions in Ranges 1, 2, and 4 doesn't have any (or it has negligible) effect on the absorption in Range 3.*

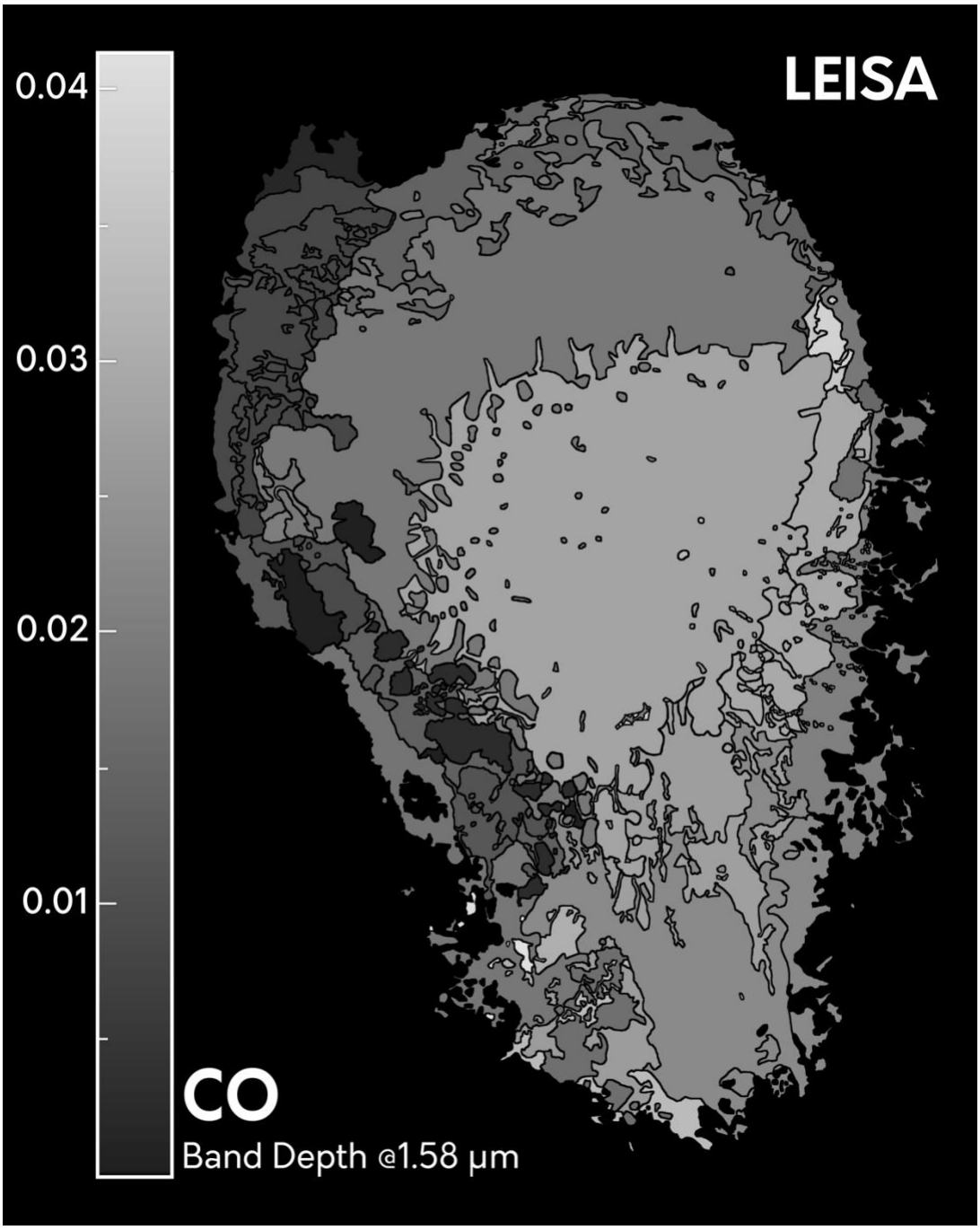

Figure 15: *Maps of variation of CO integrated band depth at 1.58 µm.*

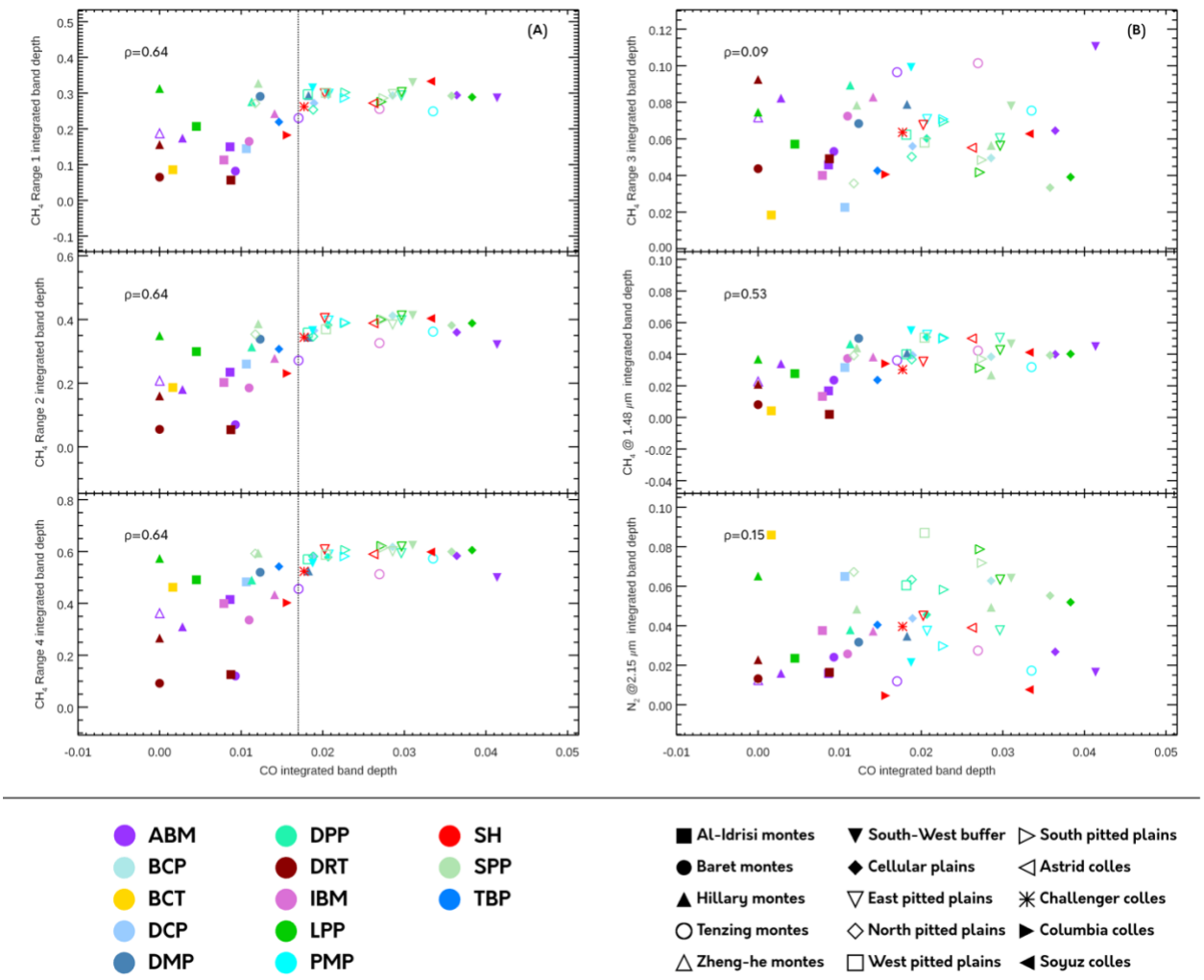

Figure 16: (A) *Scatter plot showing the correlation between the CH_4 integrated band depth in Ranges 1 (top), 2 (middle), and 4 (bottom) with the CO integrated band depth. Because rhe data shows to different trends, we split them into two groups, separated by a vertical dotted line. The units on the left side have a positive trend but a sparse distribution, the points on the right portion of the plots show a flat distribution.* ***(B)*** *Scatter plot showing the correlation between the CH_4 integrated band depth in Range 3 (top), at 1.48 µm (middle), and the N_2 integrated band depth at 2.15 µm (bottom) with the CO integrated band depth. The only clear correlation occurs between CO and the band at 1.48 µm, while the correlation coefficient for CH_4 band in Range 3 and N_2 are negligible.*

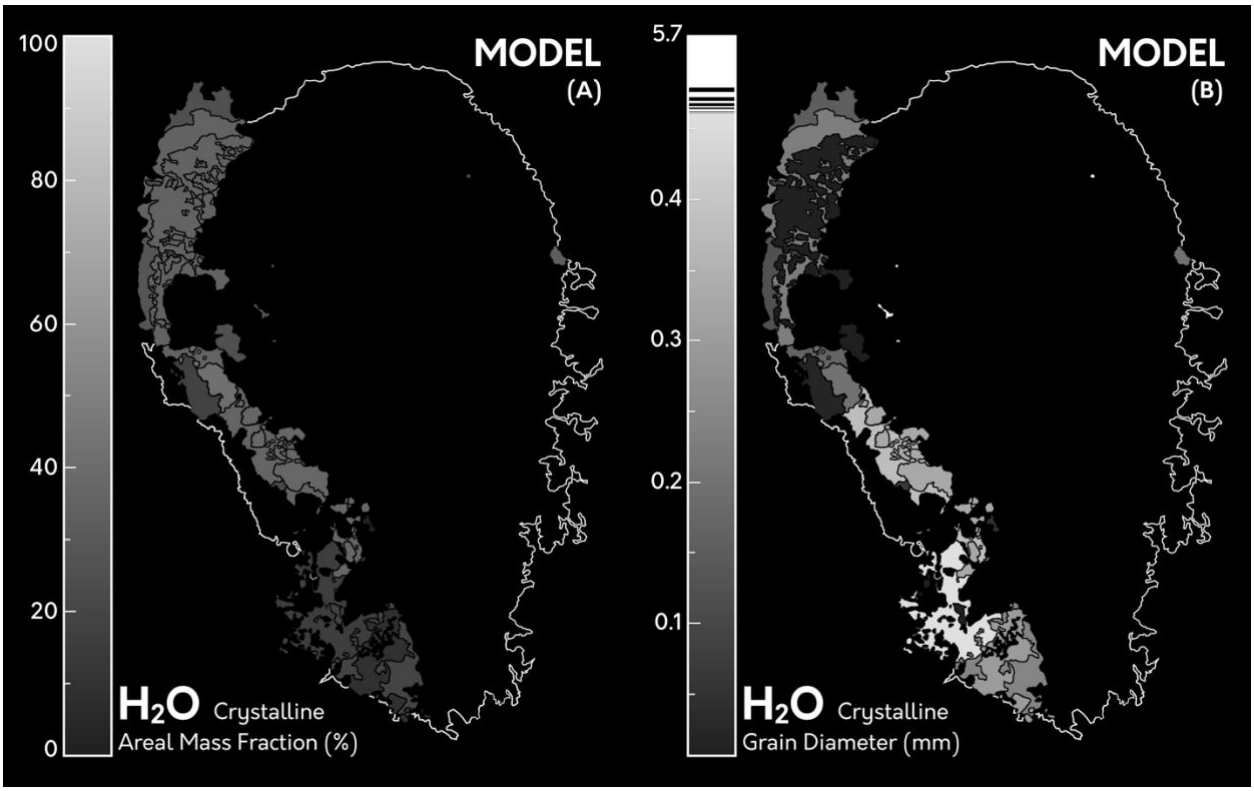

Figure 17A-B: *Maps of variation of Crystalline H_2O areal mass fraction (A) and grain size(B) estimated by the spectral modeling*

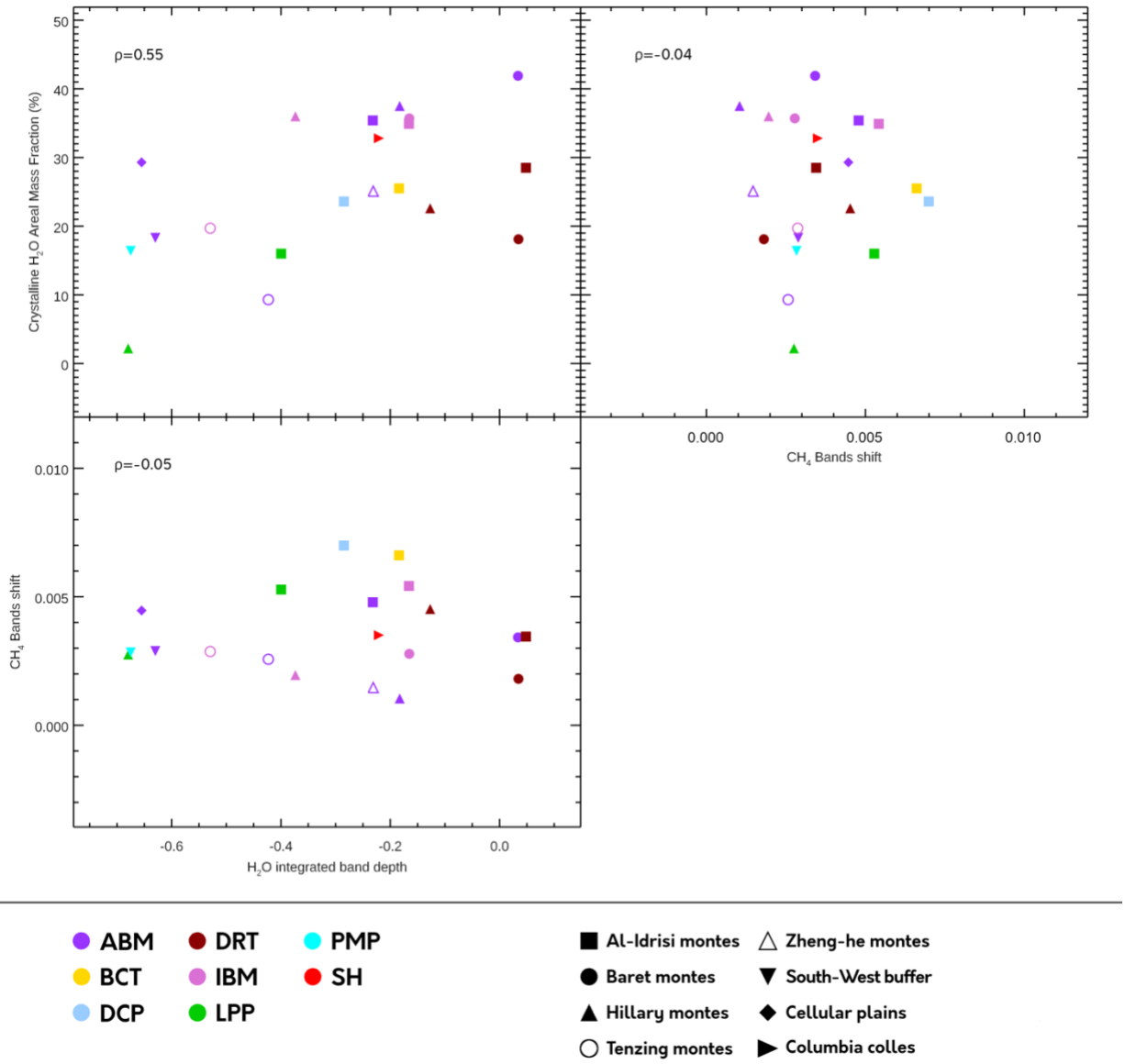

Figure 18: *Mutual variation of the crystalline H_2O areal mass fraction, the H_2O integrated band depth, and the CH_4 shift index. Crystalline H_2O ice well correlates with the H_2O integrated band depth (top, left panel), while no correlation exists between the H_2O areal mass fraction (top, right panel) and the H_2O integrated band depth (bottom, left panel) and the shift parameter, suggesting that H_2O do not influence the CH_4 band shift.*

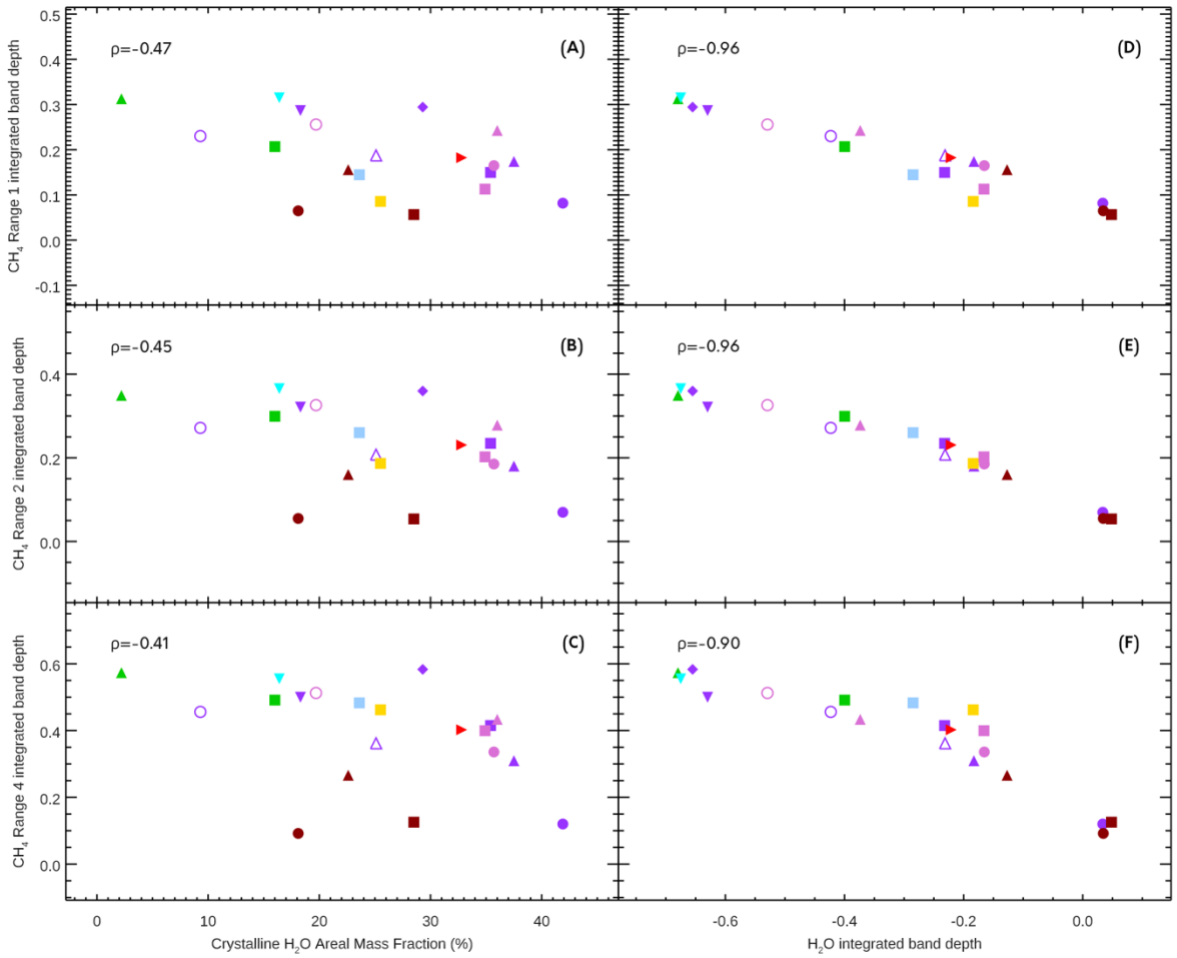

Figure 19: (A-F) *Scatter plot showing the correlation between the CH_4 integrated band depth in Ranges 1 (top), 2 (middle), and 4 (bottom) with the H2O crystalline areal mass fraction (A, B, C), and with the H_2O integrated band depth (D, E, F). All the represented parameters show clear anti-correlations, suggesting that water ice can contribute to the suppression of the strong methane ice absorptions. For some units, though, H_2O is not the only, or the main, contributor. Unit drt in Al-Idrisi and Baret Montes, and unit abm in Zheng He and Hillary Montes have the strongest absorptions in the 2.0 µm region, but moderate fractions of crystalline water ice. The discrepancy between the two water ice parameters suggests that crystalline H_2O is contributing to the absorption around 2.0 µm, but the influence of some other material must be invoked to justify such deep absorptions in this spectral area.*

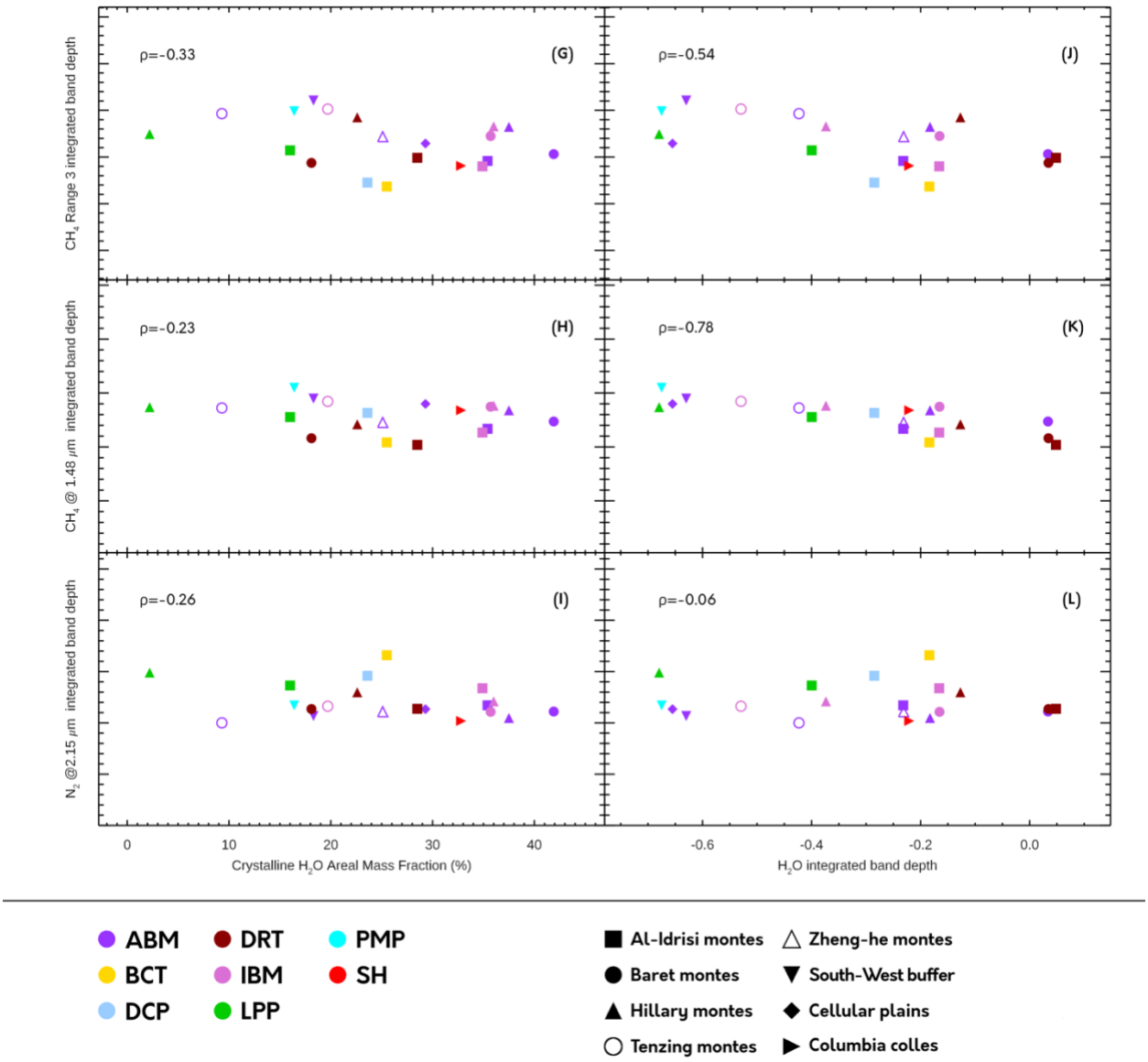

Figure 19: (G-L) *Scatter plot showing the correlation between the CH_4 integrated band depth in Ranges 3 (top), at 1.48 µm (middle), and N_2 integrated band depth at 2.15 µm (bottom) with the H_2O crystalline areal mass fraction (G, H, I), and with the H_2O integrated band depth (J, K, L). The correlation between these parameters is less pronounced than in the previous panels, and indication that crystalline H_2O minimally influence the depth of the CH_4 absorptions in Range 3 and at 1.48 µm, and of N_2.*

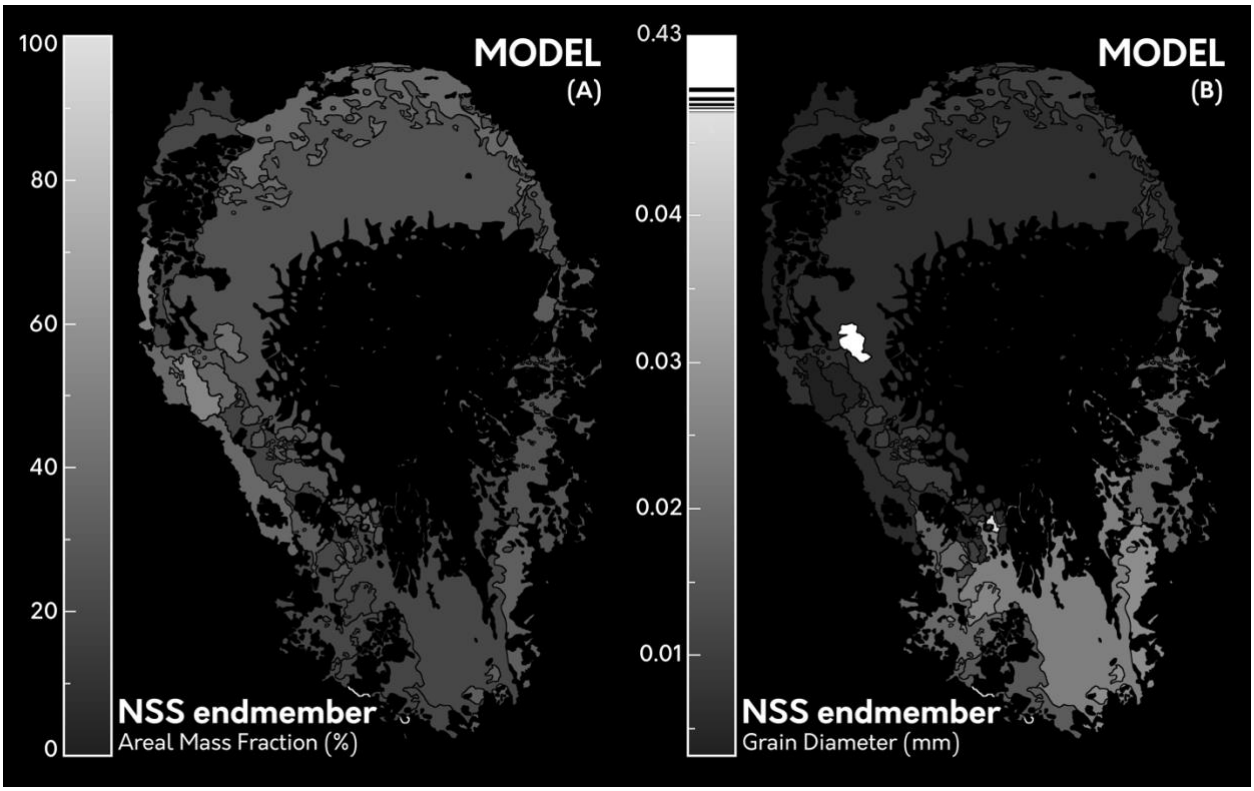

Figure 20: *Maps of variation of NSS endmember areal mass fraction (A) and grain size (B) estimated by the spectral modeling.*

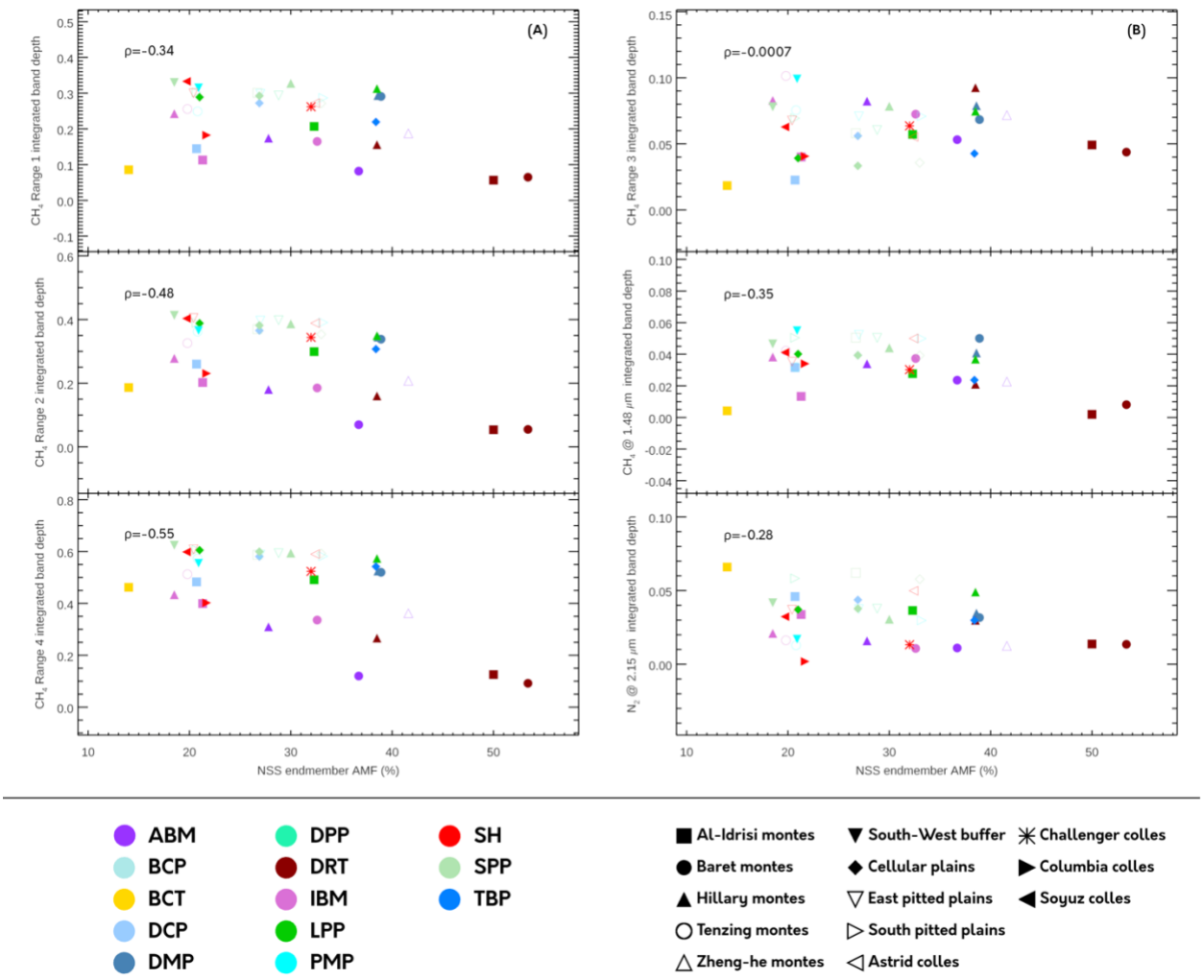

Figure 21: (A) *Scatter plot showing the correlation between the CH_4 integrated band depth in Ranges 1 (top), 2 (middle), and 4 (bottom) with the NSS endmember areal mass fraction. A moderate negative trend between the abundance of the NSS endmember with the integrated band depths of CH_4 in Range 1, Range 2, and Range 4 is observed.* ***(B)*** *Scatter plot showing the correlation between the CH_4 integrated band depth in Range 3 (top), at 1.48 μm (middle), and the N_2 integrated band depth at 2.15 μm (bottom) with the NSS endmember areal mass fraction. The NSS endmember is not correlated with the CH_4 in Range 3, while it has a moderate and slight anti correlation with the CH_4 band at 1.48 μm and the N_2 absorption at 2.15 μm.*

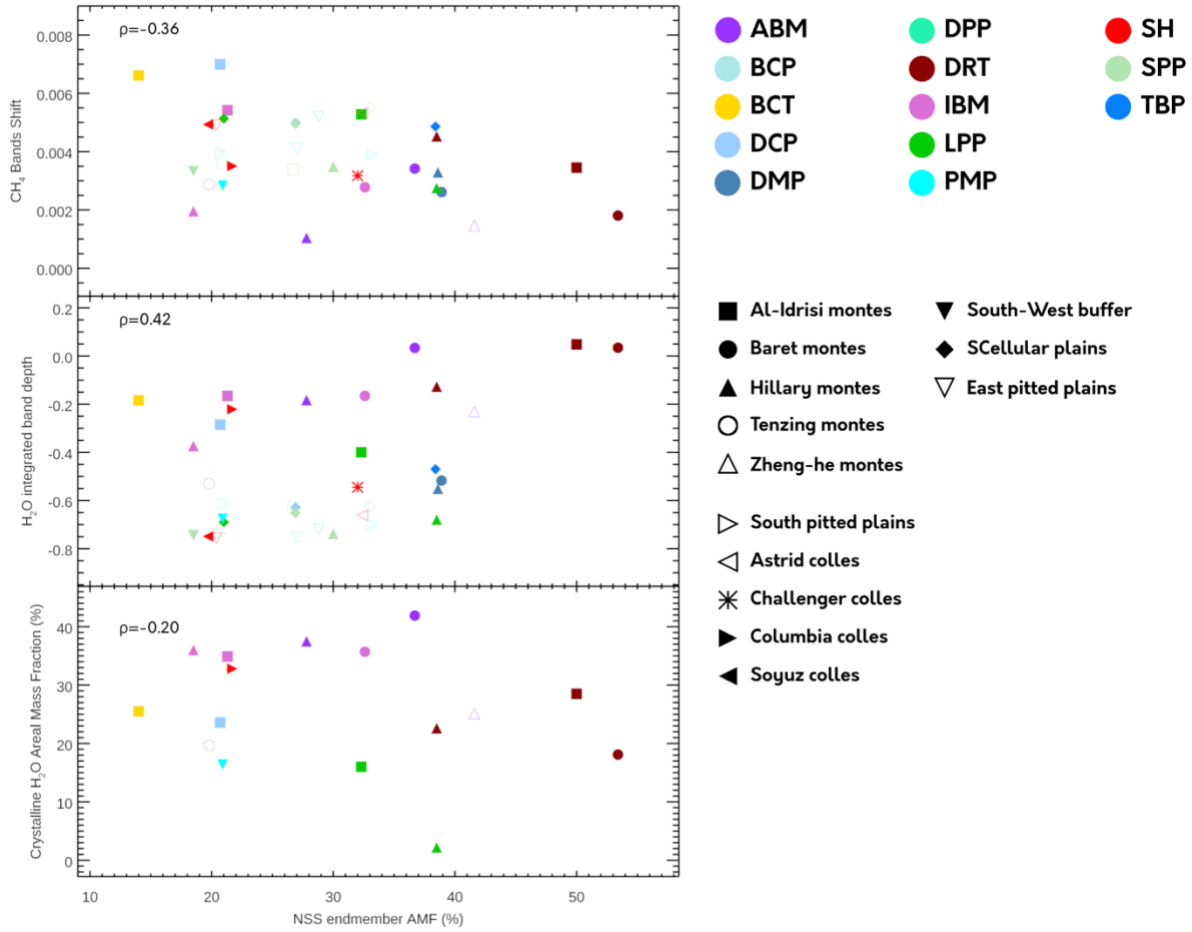

Figure 22: *Scatter plot showing the correlation between the CH_4 band shift index (top), H_2O integrated band depth (middle), and crystalline H_2O areal mass fraction (bottom) versus the NSS endmember areal mass fraction. The top panel shows a slight dependence between the shift value and the NSS slope, while in the other two panels, the represented quantities do not show any clear correlation.*

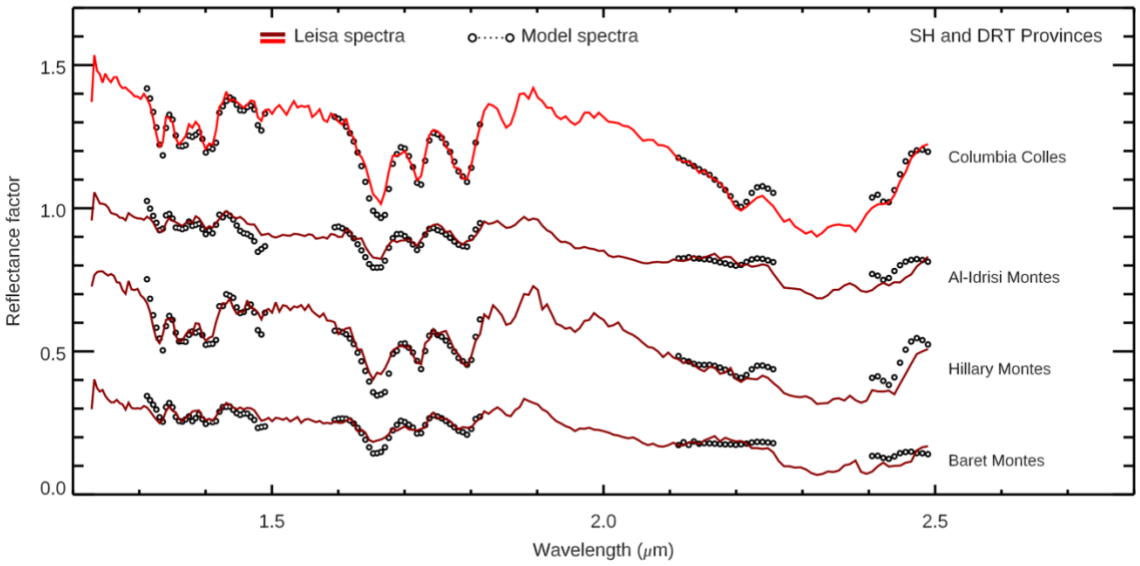

Figure 23: *LEISA spectra, averaged for unit drt in Al-Idrisi, Hillary and Baret montes, and unit sh in Columbia Colles, overlapped by the corresponding Hapke theory-based best fit model. In this case, the modeling made use of the Pluto tholins optical constants, in place of the NSS endmember ones. The spectra are offset for clarity.*

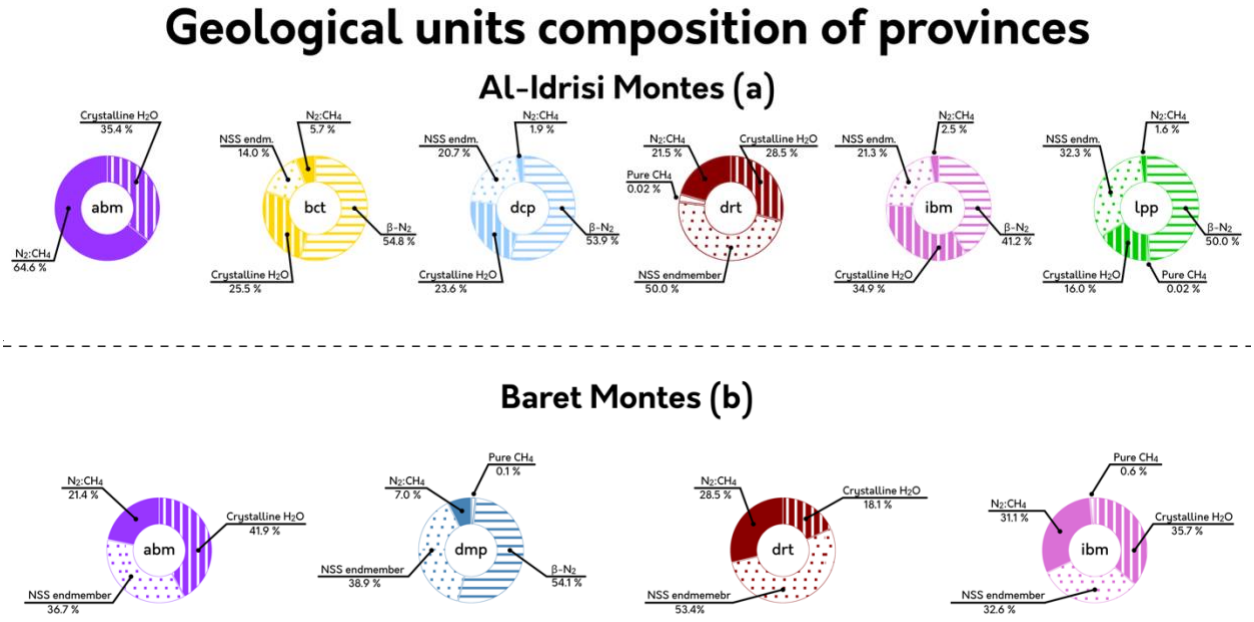

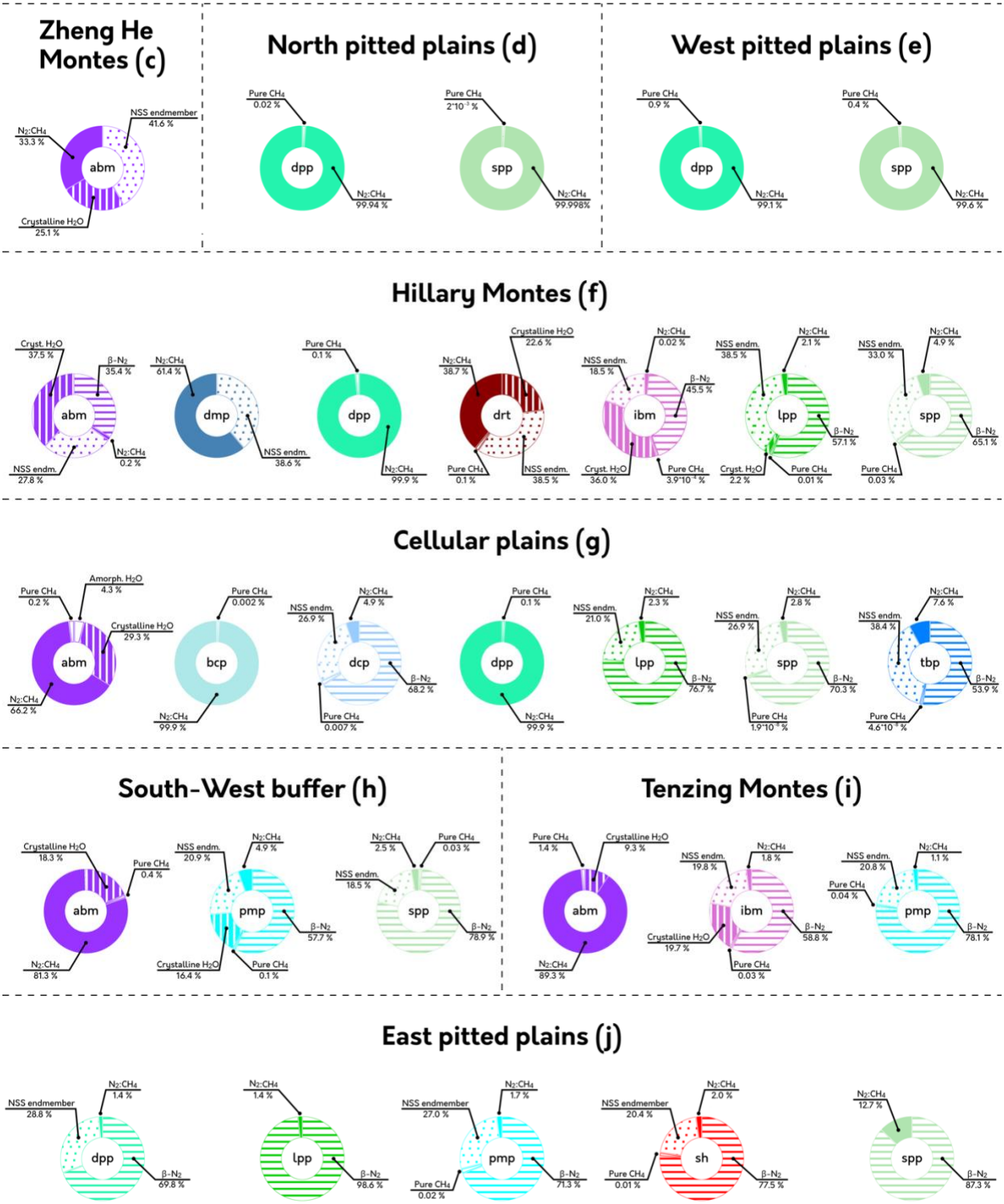
Zheng He Montes (c)
abm
N2:CH4 33.3 %
NSS endmember 41.6 %
Crystalline H2O 25.1 %
North pitted plains (d)
dpp
Pure CH4 0.02 %
N2:CH4 99.94 %
spp
Pure CH4 2·10⁻³ %
N2:CH4 99.998%
West pitted plains (e)
dpp
Pure CH4 0.9 %
N2:CH4 99.1 %
spp
Pure CH4 0.4 %
N2:CH4 99.6 %
Hillary Montes (f)
abm
Cryst. H2O 37.5 %
β-N2 35.4 %
N2:CH4 0.2 %
NSS endm. 27.8 %
dmp
N2:CH4 61.4 %
NSS endm. 38.6 %
dpp
Pure CH4 0.1 %
N2:CH4 99.9 %
drt
Crystalline H2O 22.6 %
N2:CH4 38.7 %
Pure CH4 0.1 %
NSS endm. 38.5 %
ibm
N2:CH4 0.02 %
NSS endm. 18.5 %
β-N2 45.5 %
Cryst. H2O 36.0 %
Pure CH4 3.9*10⁻⁴ %
lpp
N2:CH4 2.1 %
NSS endm. 38.5 %
β-N2 57.1 %
Cryst. H2O 2.2 %
Pure CH4 0.01 %
spp
N2:CH4 4.9 %
NSS endm. 33.0 %
β-N2 65.1 %
Pure CH4 0.03 %
Cellular plains (g)
abm
Amorph. H2O 4.3 %
Pure CH4 0.2 %
Crystalline H2O 29.3 %
N2:CH4 66.2 %
bcp
Pure CH4 0.002 %
N2:CH4 99.9 %
dcp
N2:CH4 4.9 %
NSS endm. 26.9 %
β-N2 68.2 %
Pure CH4 0.007 %
dpp
Pure CH4 0.1 %
N2:CH4 99.9 %
lpp
N2:CH4 2.3 %
NSS endm. 21.0 %
β-N2 76.7 %
spp
N2:CH4 2.8 %
NSS endm. 26.9 %
β-N2 70.3 %
Pure CH4 1.9*10⁻³ %
tbp
N2:CH4 7.6 %
NSS endm. 38.4 %
β-N2 53.9 %
Pure CH4 4.6*10⁻³ %
South-West buffer (h)
abm
Crystalline H2O 18.3 %
Pure CH4 0.4 %
N2:CH4 81.3 %
pmp
N2:CH4 4.9 %
NSS endm. 20.9 %
β-N2 57.7 %
Crystalline H2O 16.4 %
Pure CH4 0.1 %
spp
N2:CH4 2.5 %
Pure CH4 0.03 %
NSS endm. 18.5 %
β-N2 78.9 %
Tenzing Montes (i)
abm
Pure CH4 1.4 %
Crystalline H2O 9.3 %
N2:CH4 89.3 %
ibm
N2:CH4 1.8 %
NSS endm. 19.8 %
β-N2 58.8 %
Crystalline H2O 19.7 %
Pure CH4 0.03 %
pmp
N2:CH4 1.1 %
NSS endm. 20.8 %
Pure CH4 0.04 %
β-N2 78.1 %
East pitted plains (j)
dpp
N2:CH4 1.4 %
NSS endmember 28.8 %
β-N2 69.8 %
lpp
N2:CH4 1.4 %
β-N2 98.6 %
pmp
N2:CH4 1.7 %
NSS endmember 27.0 %
Pure CH4 0.02 %
β-N2 71.3 %
sh
N2:CH4 2.0 %
NSS endmember 20.4 %
Pure CH4 0.01 %
β-N2 77.5 %
spp
N2:CH4 12.7 %
β-N2 87.3 %

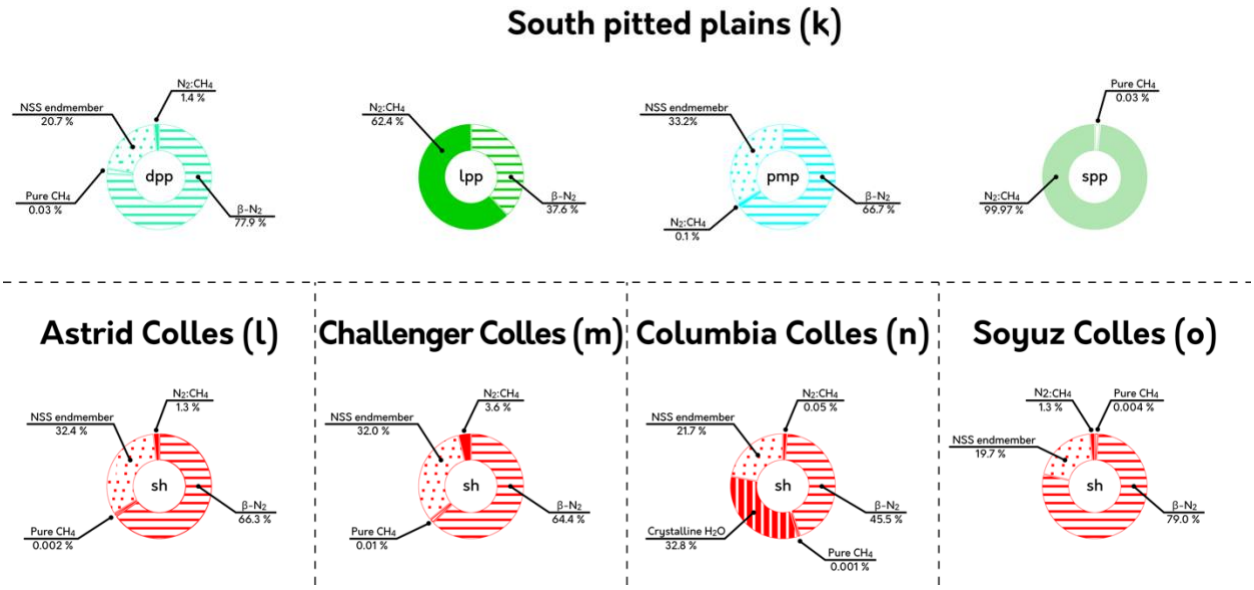

Figure 24 A-O: *Pie plots summarizing the composition of the geologic units in each province, as returned by the application of the Hapke-based spectral modeling.*

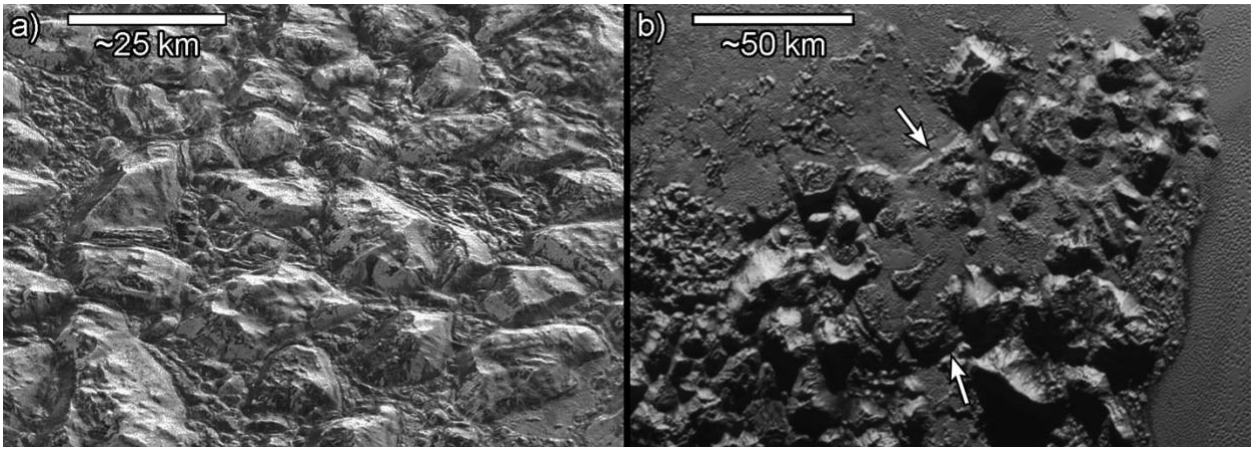

Figure 25: *Contrast between the northernmost mountain range of Al-Idrisi Montes and the southernmost range of Tenzing Montes. (a) Al-Idrisi Montes show minimal interstitial N2 ice plains between mountain blocks. LORRI image is 76 m/pixel and centered at 37.6°N, 156.3°E, with illumination from the top. (b) Several of the mountain blocks of Tenzing Montes are partly engulfed by N2 ice plains that are elevated by up to a kilometer above the surrounding N2 ice plains of Sputnik Planitia, and separated from them by scarps (white arrows). MVIC image is 315 m/pixel and centered at 13.6°S, 176.7°E, with illumination from the top.*

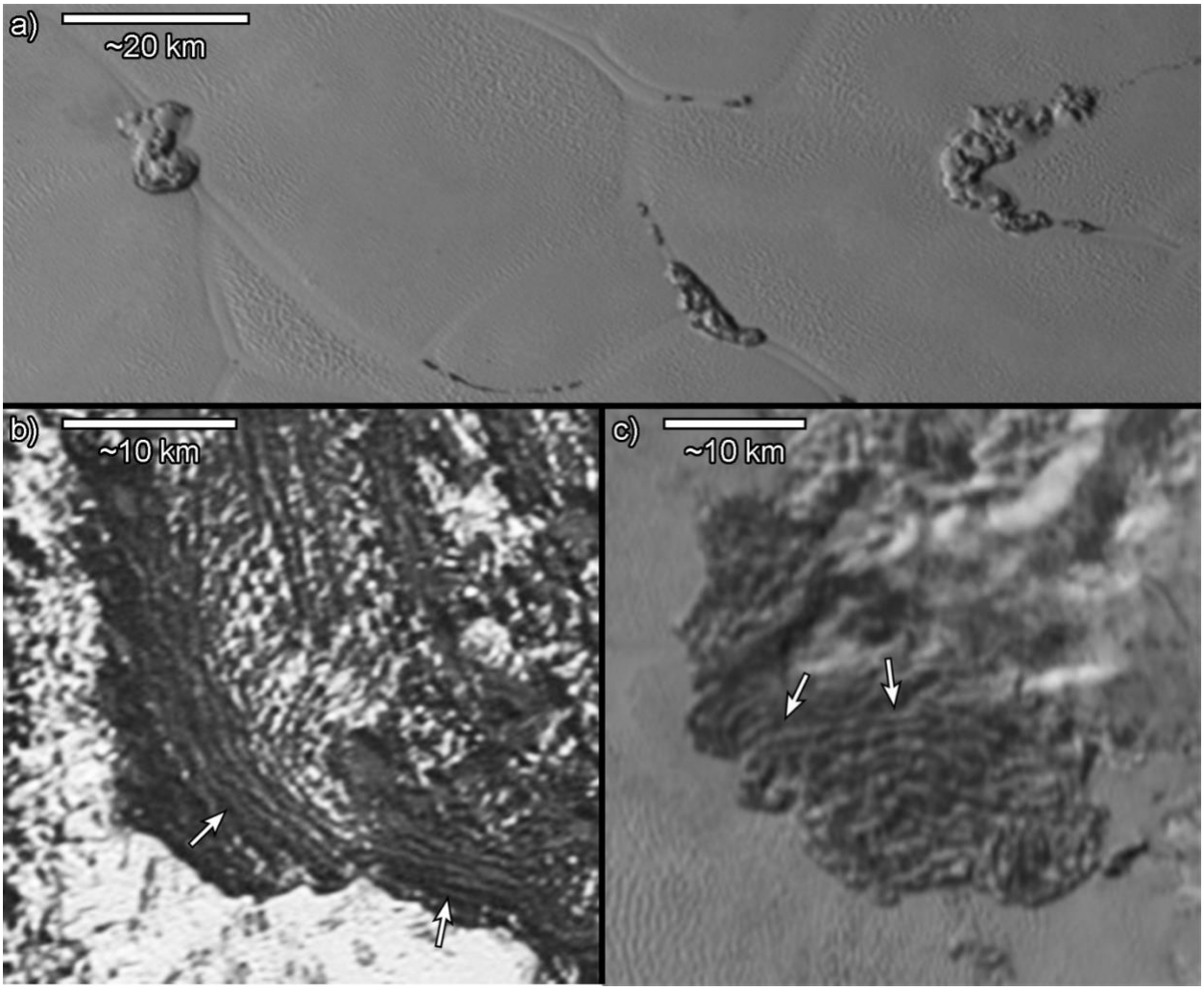

Figure 26: *Scattered hills (unit sh) and dark ridged terrain (unit drt). (a) Scattered hills of Astrid and Soyuz Colles, which display smooth topographic relief and a high albedo, indicating that the hills, like the surrounding plains, have been coated by ongoing N_2 ice deposition. MVIC image is 315 m/pixel and centered at 14.7°N, 184.5°E, with illumination from the left. (b) Dark ridges situated between Baret Montes and dark-pitted, marginal plains of Sputnik Planitia, which were mapped as unit drt by White et al. (2017). White arrows indicate ridges spaced 1-2 km apart that align roughly parallel to the border of the unit with the N_2 ice plains. LORRI image is 117 m/pixel and centered at 11.4°N, 157.5°E, with illumination from the top. (c) Columbia Colles, located at the eastern margin of Sputnik Planitia, which were mapped as unit sh by White et al. (2017). White arrows indicate ridges spaced 1-2 km apart that resemble those highlighted in (a). The comparable geomorphology and albedo of Columbia Colles to occurrences of unit drt in the west suggest that similar processes have affected Columbia Colles, which are otherwise separated stratigraphically and compositionally from unit drt. MVIC image is 315 m/pixel and centered at 28.7°N, 196.5°E, with illumination from the left.*

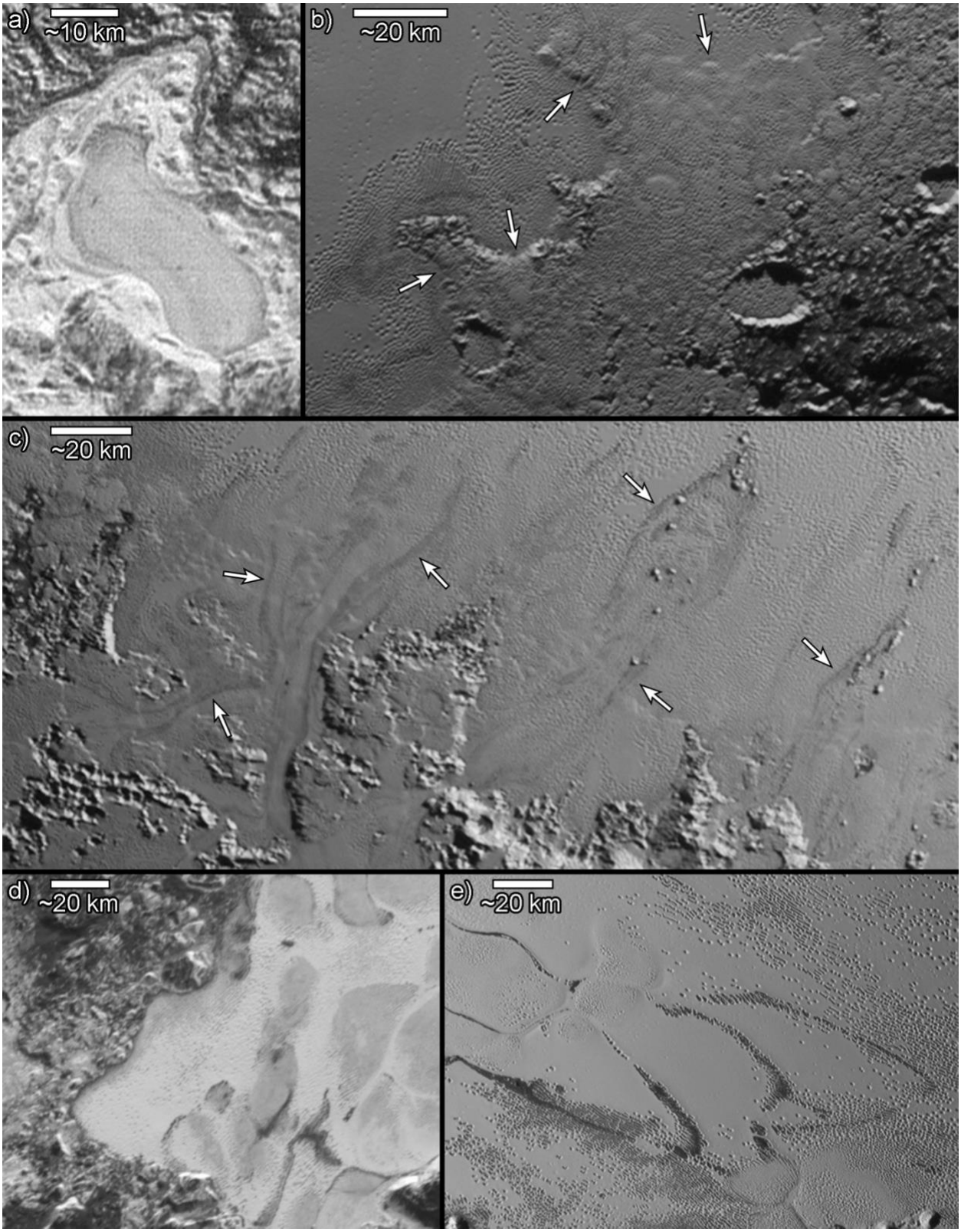

Figure 27: *Plains units of* Sputnik Planitia *described in sections 5.5 and 5.6. (a) Alcyonia Lacus, mapped by White et al. (2017) as an isolated occurrence of dark cellular plains surrounded by mountains and blocky material of Al-Idrisi Montes. LORRI image is 117 m/pixel and centered at 36.4°N, 151.6°E, with illumination from the top-right. (b)*

Hummocky N_2 ice plains of unit pmp covering low-lying uplands of Krun Macula (dark terrain at lower right). Scarps (white arrows) separate unit pmp from the flat plains of Sputnik Planitia, similar to those seen at Tenzing Montes (Fig. 26b). MVIC image is 315 m/pixel and centered at 5.8°S, 191.2°E, with illumination from the left. (c) Glacial flow of nitrogen ice from the bright pitted uplands of East Tombaugh Regio (bottom) into Sputnik Planitia. Dark, converging flow bands (white arrows) are seen in valleys that connect upland flats to Sputnik Planitia, and are interpreted to be moraine trails consisting of CH_4-rich material eroded from the pitted uplands by N_2 ice glaciation. MVIC image is 315 m/pixel and centered at 3.7°N, 193.6°E, with illumination from the top-right. (d) High-albedo, pitted plains of units dpp and spp located at the western edge of Sputnik Planitia, occurring interstitially to convective cells of the dark, cellular plains (unit dcp). MVIC image is 315 m/pixel and centered at 20.3°N, 155.1°E, with illumination from the top. (e) Dense fields of aligned (unit dpp) in southern Sputnik Planitia. Across the center of the image, they are seen to form chains of joined, dark-floored pits that trace elongated, polygonal outlines that enclose sparsely pitted plains (unit spp), and which extend southwards from the bright, cellular plains (unit bcp) at top left. MVIC image is 315 m/pixel and centered at 6.0°S, 179.7°E, with illumination from the left.

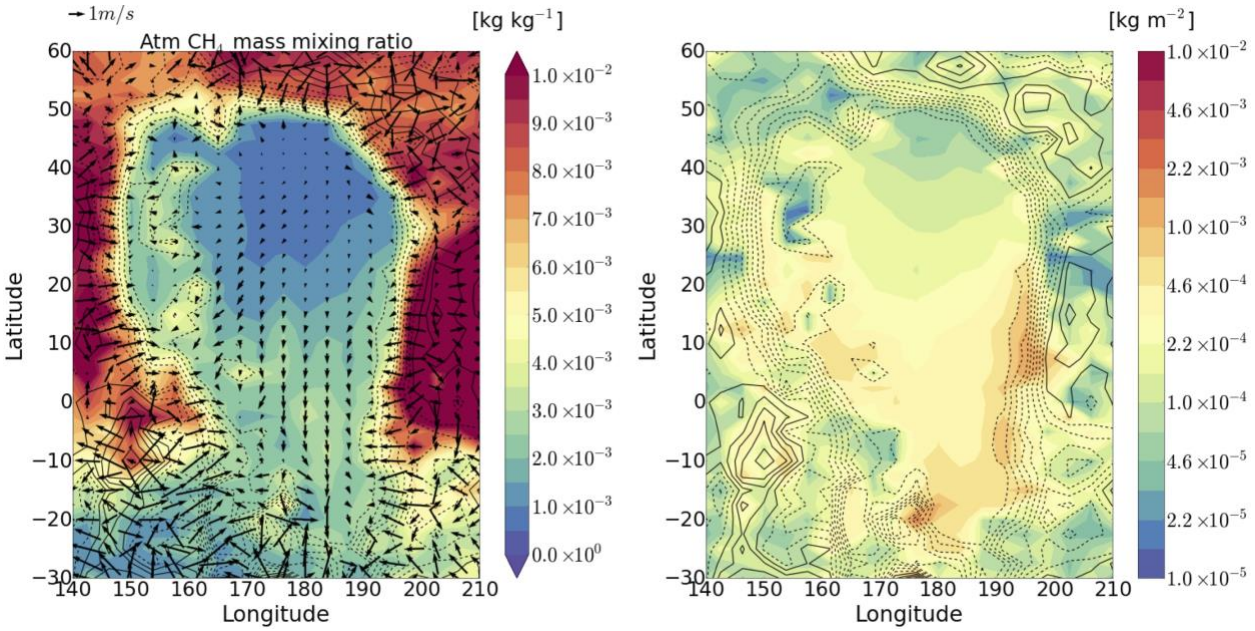

Figure 28: *Results from the global climate model of Pluto obtained for July 2015 from simulations similar to those presented in Bertrand et al., 2020b. Left: Diurnal mean near-surface (~20 m) atmospheric CH_4 mass mixing ratio in the region of Sputnik Planitia, with near-surface winds. Right: Net diurnal CH_4 deposition onto the surface.*